Universidad de Concepción

Facultad de Ciencias Físicas y Matemáticas - Programa de Magíster en Ciencias con mención en Física

Effects of the Initial Mass Function and Mass Segregation in the Evolution of Embedded Star Clusters (Efectos de la Función de Masa Inicial y Segregación de Masa en la Evolución de Cúmulos Inmersos en Gas)

Tesis para optar al grado de Magíster en Ciencias con mención en Física

Por

Raúl Esteban Domínguez Figueroa

Concepción, Chile

Marzo 2017

Profesor Guía: Dr. Michael Fellhauer

Departamento de Astronomía, Facultad de Ciencias Físicas y Matemáticas

Universidad de Concepción

Agradecimientos

Quiero agradecer en primer lugar a mis padres Raúl Domínguez y Yolanda Figueroa por apoyarme sobre todo en difíciles momentos de este largo camino . Les agradezco a mis compañeros que siempre han tenido una palabra de apoyo que me ayudaron a seguir adelante.

Este trabajo no hubiera podido ser posible sin la ayuda y apoyo de mi supervisor Michael Fellhauer, el cual siempre confió en mi y estuvo impulsándome a mejorar.

No puedo dejar de mencionar a los post-doc Rory Smith, Graeme Candlish and Jörg Dabringhausen que siempre estuvieron dispuestos a ayudar. También agradezco a Juan Pablo Farías el cual se mantuvo siempre atento a cualquier duda que tuviera. No puedo olvidar a Dominik Schleicher mas que como co-supervisor, lo consideré mas como un amigo. Gracias también a Amelia Stutz que aunque fue poco el tiempo que compartimos siempre estaba ahí ofreciendo su ayuda.

Gracias además al aporte financiero recibido por parte Fondecyt, Basal y SOCHIAS, que hicieron posible cubrir gastos de arancel y viajes.

No todo fue trabajo, así que agradezco a la party-woman Annette Gerlach que siempre tenía una sonrisa para regalar o una cerveza algunas veces!.

No puedo terminar sin antes decir gracias a mi polola Carla Fuentes por el continuo soporte y alegría luego de esas largas noches de trabajo sin dormir.

Contents

List of Figures

List of Tables

Resumen

En este trabajo investigamos la evolución de la segregación de masa para cúmulos de estrellas jóvenes inicialmente subestructurados con dos diferentes potenciales de fondo, emulando el gas en estados globales viriales y subviriales. Mediante simulaciones de N cuerpos, seguimos la evolución a lo largo de ~ 5 Myr. Medimos la segregación de masa usando el método de minimum spanning tree Λ_{MSR} usando todas las estrellas del cúmulo. También medimos la segregación de masas con una restricción Λ_{MSR}, usando sólo las estrellas más masivas dentro de los radios de media masa. Usando diferentes condiciones iniciales, encontramos que diferentes potenciales de fondo pueden conducir en la mayoría de los casos aproximadamente al mismo nivel de segregación de masa, independientemente de las posiciones iniciales de las estrellas masivas. Incluso cuando las diferencias en el resultado final son pequeñas, la evolución interna es muchos casos es muy diferente, dependiendo fuertemente de las condiciones iniciales, que puede acelerar o frenar la evolución de la segregación.

También estudiamos el proceso de mortalidad. Comenzamos con las mismas condiciones iniciales que en el trabajo anterior, pero ahora eliminando el potencial de fondo, imitando la expulsión de gas. Dejamos evolucionar los cúmulos estelares sin gas por 9 Myr después de la expulsión de gas para estudiar su supervivencia. Comparamos con una predicción anterior para simulaciones de masas iguales, encontrando que la inclusión de una función de masa inicial produce una disminución en la fracción de la masa ligada de los remanentes debido a los fuertes encuentros de dos cuerpos y efectos de evaporación.

Abstract

We investigate the evolution of mass segregation in initially substructured young embedded star clusters with two different background potentials mimicking the gas in virial and subvirial global states. By means of N-body simulation we follow the evolution along ~ 5 Myr. We measure the mass segregation using the minimum spanning tree method Λ_{MSR} using all the stars of the clusters. We also measure mass segregation with a restricted Λ_{MSR}, using only the most massive stars inside of the half-mass radii. Spanning a variety of different initial conditions, we find that different background potentials can lead in most of the cases to approximately the same level of mass segregation, independent of the initial positions of the massive stars. Even when the differences in the final result are small, the process of the internal evolution in many cases is very different, depending strongly on the initial condition, which can speed up or slow down the evolution of mass segregation.

We also study the infant mortality process. We start with the same initial conditions than described above, but now remove the background potential, mimicking gas expulsion. We let the gas-free star clusters evolve for 9 Myr after the gas expulsion to study their survival. We compare with a previous prediction for equal-mass simulations and find that the inclusion of an initial mass function produces a decrease in the fraction of the bound mass of the clusters due to strong two-body encounters and evaporation effects.

Chapter 1

General Introduction

1.1 Types of Star Cluster

Star clusters (SCs) have been long recognized as important laboratories for astrophysical research. Studies about this kind of objects have played an important role in developing and understanding of the universe. SCs contain statistically significant samples of stars spanning a wide range of stellar mass within a relatively small volume of space. Also they could be regarded as the fundamental places of star formation (SF). However only describe a cluster for been the precursor of SF process has bias and some restrictions are mandatory.

Defining what is a cluster can be difficult, and often is merely a matter of personal opinion. The criteria to refer to SC or an association can follow some restrictions, e.g. observed stellar mass volume density, where the values are sufficiently large to keep the group stable against tidal disruption of the galaxy ($\rho \geqslant 0.1\mathrm{M}_{\odot}\ \mathrm{pc}^{-3}$; Bok (1934)) and to pass through interstellar clouds ($\rho \geqslant 1.0\mathrm{M}_{\odot}\ \mathrm{pc}^{-3}$; Spitzer (1958)). Adams & Myers (2001) introduced a criterion where a cluster consists of enough stars to ensure a lifetime of more than 10^8 years (typical lifetime of open clusters), to eject all its members due to internal encounters, this lower limit is normally called evaporation time (τ_{ev}) which for stellar system in virial equilibrium, can be approximated to $\tau_{ev} \sim 10^2\tau_{relax}$, with the relaxation time of the order of $\tau_{relax} \sim \frac{0.1N}{lnN}\tau_{\mathrm{cross}}$, with τ_{cross} the time which takes a member to travel through the system and N the number of stars it contains (Binney & Tremaine, 1987). The typical value for open SCs is $\tau_{\mathrm{cross}} \sim 10^6$ years, $\frac{0.1N}{lnN} \sim 1$, obtaining a final value of $N \sim 35$.

1.1.1 Associations

This classification consists in stars that look like to form a group with low densities, below the limit to call them SCs as defined in Section 1.1. Most of them are still embedded in their primordial molecular gas and, do not appear to be gravitationally bound systems with densities $\rho < 0.1\mathrm{M}_{\odot}\ \mathrm{pc}^{-3}$.
OB-associations: They can contain thousands of O and B stars covering dozens of parsec. An example of this kind of object is LH 72 showed in Fig. 1.1 located in Large Magellanic Cloud (LMC)
T-associations: They contain less objects, around a hundred of low mass stars, mostly of them are pre-main sequence type called T-Tauri.

A summary of important parameters of this kind of objects are showed in Tab. 1.1, column 1 (OB-associations) and column 2 (T-associations).

FIGURE 1.1: OB-association in the LMC called LH 72. Is possible to observe a few high-mass, very young stars embedded in hydrogen gas. Image taken from http://spacetelescope.org/images/potw1147a/

1.1.2 Embedded Star Clusters

Embedded clusters are clusters that are fully or partially embedded in interstellar gas and dust. The studies of the physical processes of these objects have been limited because the environment that surrounds them which is obscuring the inner parts. In the last decade, the development of infrared astronomy has improved this situation, providing a better study of embedded SCs within molecular clouds (MC). The evolution of these objects is a complex mix of gas dynamics, stellar dynamics, stellar evolution, and radiative transfer which is not completely understood (e.g. Elmegreen (2007), Price & Bate (2009)), leaving some critical SC properties uncertain.

Lada & Lada (2003) suggest that $70 - 90\%$ of stars form in embedded SCs, which can be the basic unit of SF. Fig. 1.2 shows how the infrared technology can observe deep into the MC (right panel) in comparison with the visual capabilities (left panel). These kind of clusters are the youngest known stellar systems and can also be considered proto-clusters, with an embedded phase which appears to not last long, between 2 and 3 Myr. Ages older than 5 Myr rarely appear to be associated with a MC (Leisawitz et al., 1989). After the embedded phase due to different processes as supernovae, stellar winds and radiation from OB stars, some of the stars remain bound and evolve into open SCs ($\sim 10\%$), the rest of stars contribute to the Galactic field.

The summary of the parameters of embedded SCs is showed in Tab. 1.1, column 3.

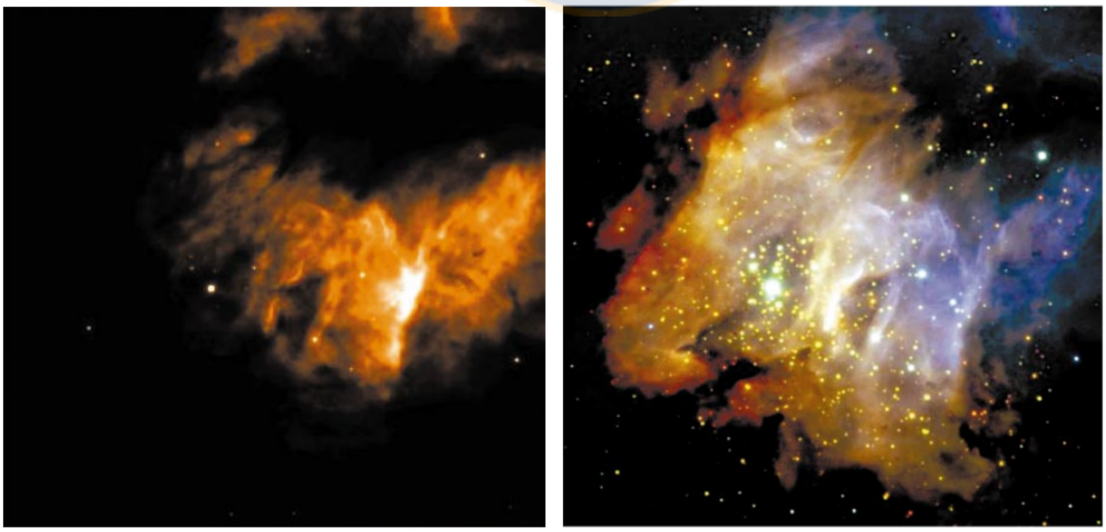

FIGURE 1.2: Optical (left) and Infrared (right) images of the RCW 38 region obtained with the ESO VLT. The infrared observations can reveal the obscured inner parts of the embedded SC which is not possible with the visual approach. Image taken from https://www.eso.org/public/images/eso0929c/

1.1.3 Open Star Clusters

Open SCs are continuously formed in the disk containing population I stars i.e. only young main sequence stars. They can be characterized as exposed clusters with practically negligible gas. Almost all clusters found in standard open cluster catalogs (e.g., Lynga (1987)) fall into this category. The common inheritance of having formed almost simultaneously from the same parent MC make them useful for observations, which help fill color-magnitude diagrams (CMDs) and the classical theory of star evolution can be tested. Additionally, SCs offer the smallest physical scale over which an accurate approach of the mass function (MF) can be made. The mutual gravitational attraction of its individual members, which support the cluster is determined by Newton's laws of motion and gravity, useful for studies of stellar dynamics. Young SCs have been used as tracers of recent episodes of SF in galaxies and in spiral structures, where the gas is still abundant. One of the most famous SC is shown in Fig. 1.3 called The Pleiads or M45.

Some properties of these objects are summarized in Tab. 1.1, column 4.

FIGURE 1.3: An example of a typical open cluster is Pleiades. Image taken from http://www.rc-astro.com/photo/id1106.html

1.1.4 Globular Clusters

Globular clusters (GCs) contain typically between 10^4 and 10^6 population II stars. Many of them are located within 10 kpc distance from the Galactic Center, but it is possible to find them further away. Some of them have distances beyond 50 kpc. Their shapes normally appear nearly spherical, as Fig 1.3 shows. They also are characterised by to be dynamically stable. They contain practically no gas, dust or young stars. The origin of a globular cluster is yet not understood. They were formed billions of years ago ($\sim 10^{10}$ yr) and are known as relics of the formation of the galaxy itself. A low number of main sequence stars can be observed compared with open SCs. As they are not actually forming in the Milky Way (with a few exceptions), so a direct empirical study of their formation process is not possible with perhaps some exceptions in extragalactic systems which can be observed. Young massive SCs are sometimes referred as young GCs, with life-times similar to many of the old GCs. The distribution of GCs was used to find the location of the Galactic Center, the existence of a Galactic halo and setting the overall scale of the Galaxy.

The principal parameters of GCs are shown in Tab. 1.1, column 5.

FIGURE 1.4: M80 (NGC 6093) is one of the densest known globular clusters in the Milky Way Galaxy; it lies in the constellation Scorpius and was discovered by Messier & Niles (1981). Image taken from http://hubblesite.org/image/837/ news_release/1999-26

TABLE 1.1: Parameters of the different types of associations and clusters. From Galactic Dynamics (Princeton Series in Astrophysics) and Portegies Zwart et al. (2010)

	OB associations	T associations	Embedded Cluster	Open Cluster	Globular Cluster
Core density ρ_r	< 1 M$_\odot$ pc^{-3}	< 1 M$_\odot$ pc^{-3}	$> 10^3$ M$_\odot$ pc^{-3}	$> 10^3$ M$_\odot$ pc^{-3}	$< 10^3$ M$_\odot$ pc^{-3}
Size	> 100 pc	< 100 pc	< 5 pc	< 10 pc	10-100 pc
Number of stars	$10^3 - 10^5$	10 - 100	$10^2 - 10^5$	10^3	$10^5 - 10^6$
Mass M	$10^3 - 10^4$ M$_\odot$	$\sim 10^2$ M$_\odot$	$< 10^4$ M$_\odot$	$> 10^2$ M$_\odot$	$< 10^6$ M$_\odot$
Lifetime	$< 10^6$ yr	$< 10^6$ yr	$< 10^5$ yr	10^8 yr	2×10^{10} yr
Mostly Observed	Close GMC	Close Dark MC	Embedded MC	Disk	Halo

1.2 Hertzsprung-Russell diagram

The Hertzsprung-Russell (H-R) diagram, shows the relationship between the luminosities and effective temperatures as the panels in the Fig. 1.5 illustrates. The prominent diagonal is called the main sequence. Depending on the object the main sequence can be different.In open SCs, the H-R diagram looks like the left panel. For older objects, the top part of the main sequence become shorter (middle panel) and is possible to observe the turnoff point where the red giants are located. The main sequence can be even much shorter (right panel) for oldest objects as globular clusters showing the turnoff point more populated.

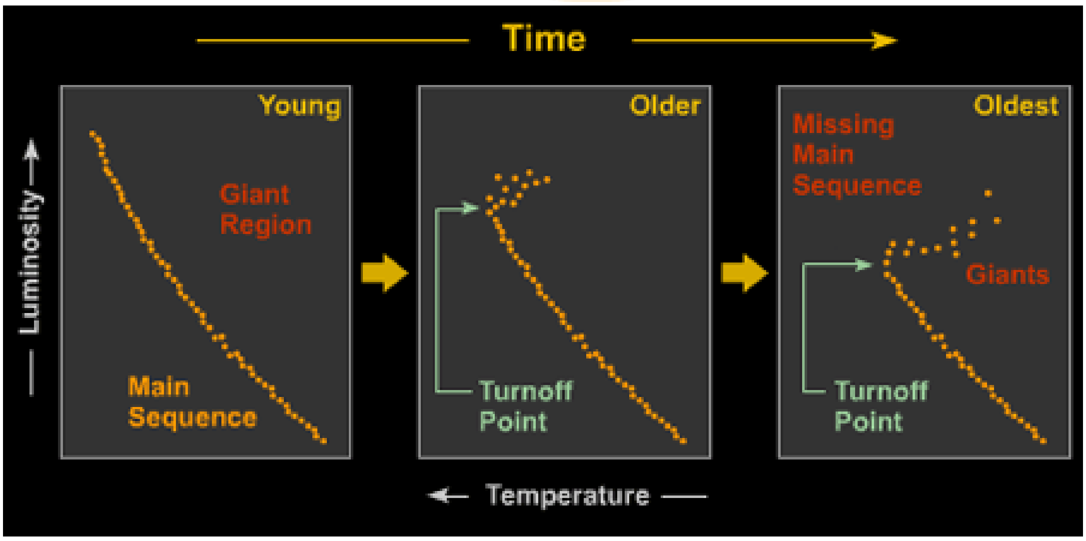

FIGURE 1.5: Turn off point at different ages of SCs. Left panel is the tipical H-R diagram for an open SCs. Right panel shows the H-R diagram observed for GCs. From Brooks/Cole Thomson Learning.

1.3 Overview of Star Formation Process

The process starts with the gravitational collapse of a giant MC (GMC) (or part of) where then the stars are formed. This process only starts if the the equilibrium of the cloud is disturbed e.g. a shock coming of a supernovae or a collision with another cloud, which causes a collapse under its self gravity. AS a consequence of the collapse, the cloud is breaking into many fragments. If the fragments of the GMC have more mass than the Jeans mass (M_j) it is not possible to maintain the hydrostatic equilibrium, producing essentially a free-fall collapse (Jeans, 1902). The fragmentation continues along the cloud, producing a wide range of masses and even very low mass objects ($< 0.1\mathrm{M}_\odot$).

As a product of the collapse the gas releases gravitational potential energy as heat. As its temperature and pressure increases, the fragment condenses into a rotating sphere of hot gas producing decrease of the collapse. In this stage of the process it is possible to speak of a proto-star.

The gas still surrounding the proto-star keeps falling onto the core, this is a process dominated by accretion. The accretion of gas generates gravitational energy, part of which further heats the core and part of which is radiated away, providing the luminosity of the proto-star.

When the gas on the core reaches a temperature of ~ 2000 K the molecular hydrogen (H_2) starts to dissociate and the hydrostatic equilibrium is no longer possible and a renewed phase of dynamical collapse follows, during which the gravitational energy release is absorbed by the dissociating molecules without a significant rise in temperature. When H_2 is completely dissociated into atomic hydrogen (H), helium (He) is restored and the temperature rises again. Somewhat later, further dynamical collapse phases follow when first H and then He are ionized at $\sim$ 104 K. When ionization of the protostar is complete it settles back into hydrostatic equilibrium at a much reduced radius

Finally, the accretion slows down and its luminosity is now provided by gravitational contraction. The contraction continues, until the central temperature becomes high enough for nuclear fusion reactions. Once the energy generated by H fusion compensates for the energy loss at the surface, the star stops contracting and reaches the main sequence phase.

1.4 Virial Ratio

The virial ratio (Q) is the fraction of kinetic energy k and the total potential energy Ω of a cluster:

$$\mathrm{Q} = \frac{k}{|\Omega|} \tag{1.1}$$

Depending of the value of Q important information of the global processes occurring in a SC can be derived.

- Q= 0.5 reflects that the SC is in virial equilibrium, a very stable configuration
- Q< 0.5 means that Ω is dominating and a collapse of the SC is produced. This state is known as cool or subvirial state.
- Q> 0.5 is obtained when k is dominating producing an expansion of the SC.
- Q> 1 is giving information about of a unbound object with stars escaping and spreading.

Observations show that for SCs in the embedded phase the stars appear to be in a dynamically cool state (Peretto et al., 2006, 2007; Proszkow & Adams, 2009) and this property is supported by hydrodynamical simulations of star formation (Klessen & Burkert, 2000; Offner et al., 2009; Maschberger et al., 2010).

1.5 The Initial Mass Function

The initial mass function (IMF) is normally assumed as universal taking studies derived from the Solar Neighborhood (Salpeter, 1955; Miller & Scalo, 1979; Kroupa, 2001) which can not be true. Studies of young massive SCs are deficient in low-mass stars and/or top-heavy (Smith & Gallagher, 2001), and different behaviors can be observed. Many cases impose minimum and maximum stellar masses. Some of the studies exclude masses lower than $\sim 1\mathrm{M}_{\odot}$, which are not important for young SCs but extremely affecting the oldest SCs (> 100) Myr, where the lower-mass stellar population is very important, e.g., to reproduce accurate relaxation times. The high masses restriction is less important, there are good relations between the total mass of the cluster and the mass of the most massive star (Vanbeveren, 1982; Weidner & Kroupa, 2004) and they evolve fast enough to disappear after a few Myr.

The MFs are usually described by the following equation:

$$\phi(m) = \frac{dN}{dm} \propto m^{\alpha} \tag{1.2}$$

where m is the mass of a star, N the number of stars in a range of mass and α is the slope of the relation obtained.

Salpeter (1955) was the first to introduce the IMF, providing a very good relation between $log(dN/dm)$ connected with $logm$ of the stars in SCs, with a value of $\alpha = -2.35$. There is not only one description for the slope of the relation. Phelps & Janes (1993) based their study on several open SCs covering a mass range 1-8 $M_\odot$ finding agreement with the Salpeter value with $\alpha = -2.4 \pm 0.13$. There might be exceptions for the Salpeter slope (e.g. Sanner et al., 1999; Sanner & Geffert, 2001; Prisinzano et al., 2003; Kalirai et al., 2003; Pandey et al., 2005). An improvement of the determination of the subsolar IMF was developed by Moraux et al. (2003) in the Pleiades finding an $\alpha = -2.7$. Other measurements in the Magellanic Clouds also support the Salpeter slope (e.g. Cayrel et al., 1988; Sagar & Richtler, 1991; Fischer et al., 1991; Bencivenni et al., 1991; Will et al., 1995) where the SCs differ in many physical properties. Excluding the large uncertainties in some individual measurement, it is possible to talk of an universal IMF (Sagar, 2002), at least in the range 1-20 $M_\odot$. Fig. 1.6 shows different objects with their respective MF.

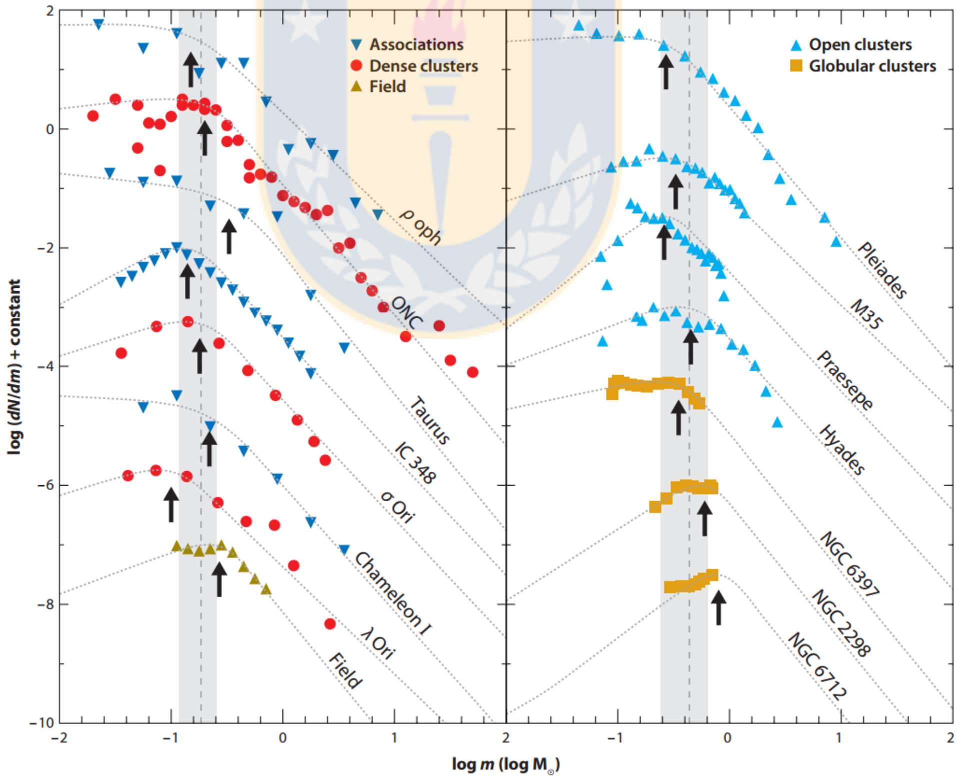

FIGURE 1.6: IMF shapes for different types of objects. Image taken from Bastian et al. (2010)

1.6 Internal Processes of Young Star Clusters

The dynamics of SCs can be split in three big steps, the first is the embedded phase, which it is followed as a gas free evolution, with mass loss taking the important role. Finally the pure dynamical processes are defining the long-term evolution of the SCs.

1.6.1 Timescales

There are two fundamental timescales of a self-graviting system called dynamical time ($\tau_{\rm dyn}$) and the relaxation time ($\tau_{\rm rel}$).

The time required for a system to find the equilibrium can be described with $\tau_{\rm dyn}$ by:

$$\tau_{\rm dyn} = \frac{GM^{5/2}}{(-4E)^{3/2}} \tag{1.3}$$

where $E \equiv k + \Omega$, the total energy of the system. In virial equilibrium (Q $= 0.5$) $2k + \Omega = 0$, assuming the form of Spitzer (1987):

$$\tau_{\rm dyn} = \frac{GM^{-1/2}}{r_{\rm vir}^{3}} \tag{1.4}$$

where $r_{\rm vir} = \frac{GM^2}{2|U|}$ the virial radius. The necessary time on which two-body encounters transfer energy between them establishing thermal equilibrium is represented by $\tau_{\rm rel}$ (Spitzer, 1987) with the equation:

$$\tau_{\rm rel} = \frac{\langle v^2 \rangle^{(3/2)}}{15.4 G^2 \bar{m} \rho \ \ln \ \Lambda} \approx \frac{N}{8 \ \ln \ N} \tau_{\rm cross} \tag{1.5}$$

where $\langle v^2 \rangle$ the root-mean-square speed, $\bar{m}$ the mean mass, ρ the local density and $\tau_{\rm cross} = R/\langle v \rangle$, with R the radius of the cluster and $\langle v \rangle$ the average velocity i.e., the necessary time for one star travel to the center. The value of Λ is $0.4N$ when all stars have the same mass and are homogeneously distributed with an isotropic velocity distribution (Spitzer, 1987). For systems with different masses the effective value of Λ may be much smaller.

Replacing in the last equation the average values for a cluster in virial equilibrium and assuming $R_h = r_{\rm vir}$ (where R_h is the half-mass radius) it is possible to obtain the half-mass two body relaxation time ($\tau_{\rm rh}$) represented by the equation:

$$\tau_{\rm rh} = \frac{N}{7 \ \ln \ \Lambda} \tau_{\rm dyn} \tag{1.6}$$

All these τ are describing the time to reach different types of equilibrium.

After an SC find some kind of equilibrium at $\tau_{\rm rel}$, the stars can show a Maxwellian velocity distribution. Two-body relaxation allows to the stars to exchange energy between them increasing or decreasing their velocities. Some fraction of the stars (ϵ_s) can have velocities larger than $v_{\rm esc}$ escaping from the SC, producing a new Maxwellian distribution, with a new tail of stars which will escape again. In this context if is assumed a constant ϵ_s inside of the R_h a dissolution time can be estimated as $\tau_{\rm dis} = \tau_{\rm rh}/\epsilon_s$. For a typical SC density profile $\epsilon_s \approx 0.033$, resulting in a $t_{\rm dis} \approx 30\ t_{\rm rh}$ for isolated SCs (Spitzer (1987)). The fraction ϵ_e can no be constant for a SCs orbiting a host galaxy. Gieles & Baumgardt (2008) show that $\epsilon_s \approx (R_h/r_j)^{(3/2)}$, where the Jacobi radius $r_j = \left(\frac{GM}{2(V_G/R_G)^2}\right)^{(1/3)}$ (King (1962)), with R_G and V_G the Galactocentric distance and the circular orbital speed respectively.

1.6.2 Mass Segregation

Mass segregation (MS) has been detected even in embedded star clusters (Lada et al., 1996; Hillenbrand, 1997; Hillenbrand & Hartmann, 1998; Bonatto & Bica, 2006; Chen et al., 2007; Er et al., 2013), this means that the most massive stars are preferentially concentrated (not necessary in the centre). The process to become a segregated cluster can be dynamical (McMillan et al., 2007; Allison et al., 2009; Yu et al., 2011) and fast for cool and substructured clusters (Allison et al., 2010; Parker et al., 2016) reaching MS in ~ 1 Myr. Primordial MS is also possible as result of the star formation process (Zinnecker, 1982; Murray & Lin, 1996; Elmegreen & Krakowski, 2001; Klessen, 2001; Bonnell et al., 2001; Bonnell & Bate, 2006) where the massive stars tend to form in the centers of the star-forming regions because the higher accretion rates in the central parts or as a result of competitive accretion (Larson, 1982; Murray & Lin, 1996; Bonnell et al., 1997). The last primordial state has been used to explain very high levels of MS in short times when only dynamical processes are not fast enough to explain the observed MS (Bonnell & Davies, 1998; Raboud & Mermilliod, 1998).

The pure theoretical dynamics approach is described in Spitzer (1969) with a segregation time (τ_{seg}) for a star with mass M. The necessary time for a star to travel to the center is described by the equation:

$$\tau_{\rm seg} \approx \frac{\bar{m}}{M}\frac{N}{8\ln\ N}\frac{R}{\langle v\rangle} \tag{1.7}$$

which e.g. for a cluster of $R = 1.5$ pc, $N = 1000$, $\bar{m} = 0.5\ {\rm M}_\odot$ and $\langle v\rangle \sim 2$ km s^{-1} results in a $t_{\rm seg} \sim 1.7$ Myr, enough time to segregate even in the embedded phase. This approximation is only measuring the time which takes for one single star travel from the outer part to the centre, as a free fall, which could not be possible for a populated cluster where many other interactions are happening.

To quantify the level of MS many methods have been published which in some cases produce contradictory results as they do not measure the same thing. The methods tested by Parker & Goodwin (2015) are summarized in the following section.

1.6.2.1 Radial Mass Functions $\mathcal{M}_{\mathbf{MF}}$

This method compares the radial distribution of different masses (e.g. Sagar et al., 1988; Gouliermis et al., 2004; Stolte et al., 2006; Sabbi et al., 2008; Chavarría et al., 2010). According to this model if a cluster is showing mass segregation, the most massive stars are preferentially towards the center, and low mass stars located in the outer locations. This method shows some disadvantages. A center definition is required which is acceptable in relaxed, virialized and uniform distributions, but not working in substructured star formation regions.The radial bins are very dependent of the radius-range where it is counting stars and is often arbitrarily. Also there is not a clear interpretation about a quantitative description of MS.

1.6.2.2 Minimum Spanning Tree $\Lambda_{\mathbf{MST}}$

This method was introduced by Allison et al. (2009) and, relates the spatial distribution of the N most massive stars with respect to many samples of randomly chosen N low massive stars. To measure the spatial distribution the method uses a technique called minimum spanning tree (MST), which it is not necessary and centre definition. The MST in this context is basically the minimum path which connects N stars. To use this definition, it is necessary to find the length of the N most massive stars and several samples using the same N for low massive stars to compare as follow:

$$\Lambda_{\mathrm{MST}} = \frac{\langle l_{\mathrm{average}} \rangle}{l_{\mathrm{subset}}} \pm \frac{\sigma_{\mathrm{average}}}{l_{\mathrm{subset}}} \tag{1.8}$$

where $\langle l_{\mathrm{average}} \rangle$ is the average of the several measurements of l from the N low massive stars with the associate error $\sigma_{\mathrm{average}}$. The length of the MST of the N most massive stars is denoted by l_{subset}.

The different values of Λ_{MST} can give different information. If the low mass stars are distributed in the same way as the most massive stars, one obtains a value of $\Lambda_{\mathrm{MST}} \sim 1$. When $\langle l_{\mathrm{average}} \rangle$ is bigger than l_{subset} $\Lambda_{\mathrm{MST}} > 1$ is obtained, which indicates that the most massive stars are preferentially concentrated, compared to the low mass stars. A high level of MS is denoted by $\Lambda_{\mathrm{MST}} >> 1$. It is possible that the low mass stars can be more concentrated, resulting in a value of $\Lambda_{\mathrm{MST}} < 1$. An associated error is calculated $(\pm \frac{\sigma_{\mathrm{average}}}{l_{\mathrm{subset}}})$, which makes possible to note if the obtained result is enough reliable.

The $\Lambda_{\rm MST}$ method is measuring MS more according to the classical sense, where the most massive stars are preferentially concentrated and not necessarily centered.

1.6.2.3 The Local Density Ratio $\sum_{\rm LDR}$

This method was presented by Maschberger & Clarke (2011). A measurement of the local surface density ($\sum = \frac{n-1}{\pi r_n^2}$) of every star is developed to compare with the average local surface density of the N most massive stars producing a local surface density ratio. This ratio is giving information of detected MS if the most massive stars are located in regions of higher local surface density. This method is also not assuming the existence of a center. The ratio is expressed as follow:

$$\sum_{\rm LDR} = \frac{\bar{\sum}_{\rm subset}}{\bar{\sum}_{\rm all}} \tag{1.9}$$

1.6.2.4 Comparison of the Methods

In order to test the methods Parker & Goodwin (2015) try the methods for three differents configurations of masses in a substrutured distribution. Starting with a random distributions as shown in Fig. 1.7, with red filled points denoting the ten most massive stars. The methods detect MS as follows:

i) $\mathcal{M}_{\rm MF}$: The Fig. 1.8, top panel, shows the cumulative distribution from the centre for all particles as a solid line and, with a dashed line for the ten most massive stars. Until 3 pc both distribution follow almost the same path but splitting after that, due there are not massive stars at radii larger 3.2 pc.

ii) $\Lambda_{\rm MST}$: The Fig. 1.8, middle panel, shows the level of MS dependent on the number of the most massive stars. This method detects MS for the ten most massive stars (1.7 ± 0.4) and, a no depreciable level of MS for the 20 most massive stars .

iii) $\sum_{\rm LDR}$: The Fig. 1.8, bottom panel, shows the stellar surface density for each individual mass. The blue dashed line is the average $\sum$ for low mass stars (13.1 stars pc^{-2}) and the red solid line the average for the ten most massive stars (13.2 stars pc^{-2}), finding no MS.

For this configuration for an observer is possible to say that even where the are randomly distributed, some level of concentration is more appreciable for the ten most massive stars. The only method which detect a level of MS is the $\Lambda_{\rm MST}$.

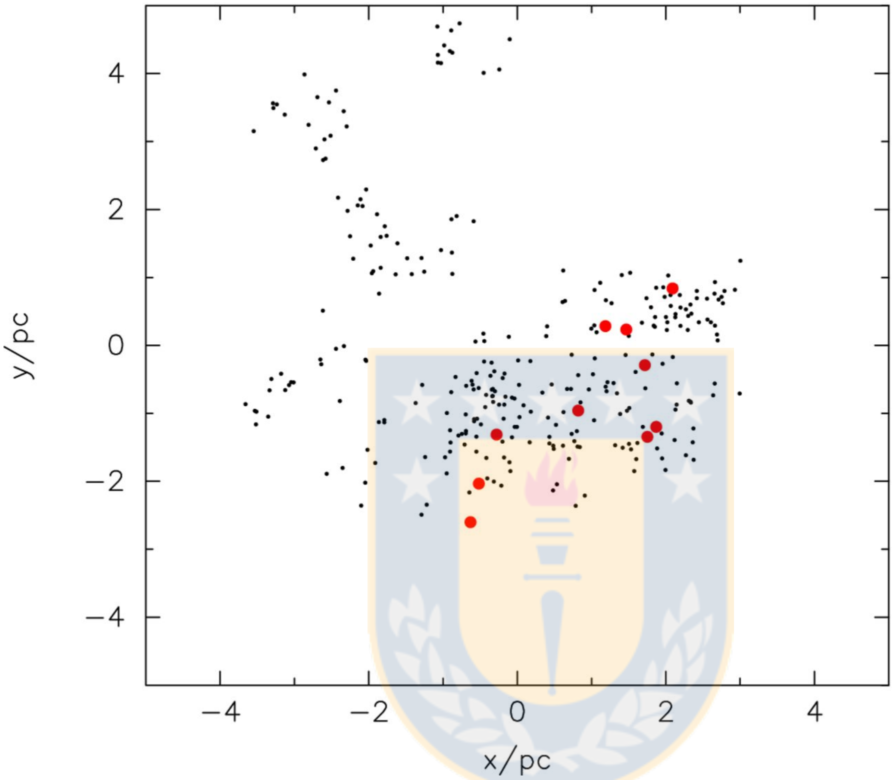

FIGURE 1.7: Substructured distribution with stars randomly drawn from an initial mass function and placed randomly in the spatial distribution. The ten most massive stars are shown by the larger (red) points. Image taken from Parker & Goodwin (2015).

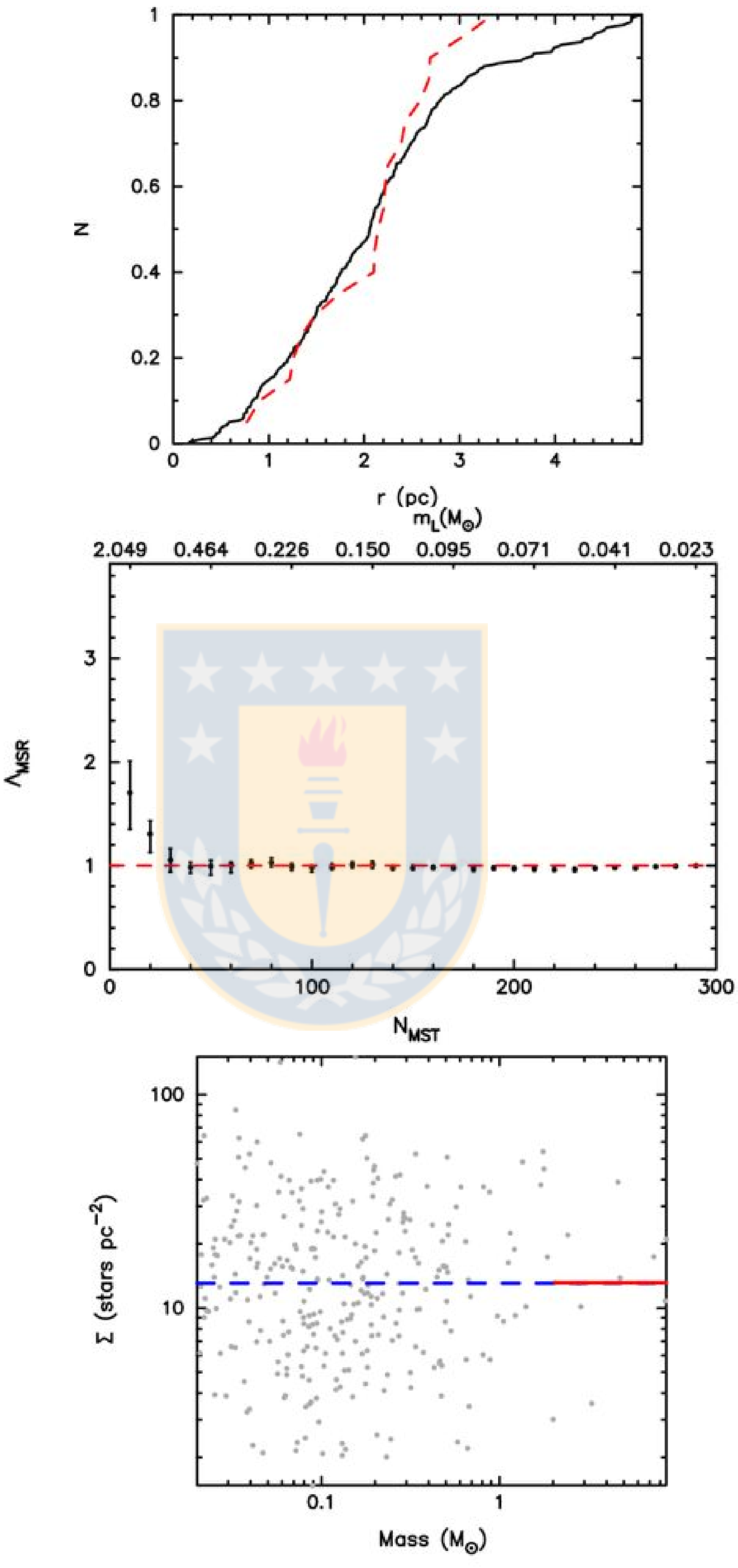

FIGURE 1.8: Three separate measures of mass segregation for the stellar distribution shown in Fig. 1.7. In top panel is showed the cumulative distribution ($\mathcal{M}_{\rm MF}$) of the distance from the centre for the ten most massive stars (the red dashed line) and the cumulative distribution for all stars (the solid black line). In the middle panel is showed the $\Lambda_{\rm MST}$ value as a function of the $\rm N_{MST}$ i.e. stars used in the subset. In bottom panel is showed local stellar surface density versus stellar mass ($\sum_{\rm LDR}$). The median stellar surface density for the ten most massive stars is shown by the solid (red) horizontal line and the median surface density for all of the stars is shown by the blue horizontal dashed line. Images taken from Parker & Goodwin (2015).

The methods were tested for a centrally concentrated distribution, locating the ten most massive stars in the inner positions of the fractal, as the Fig 1.9 shows. The distribution looks like the classical picture of MS, where the most massive stars are preferentially concentrated in the centre.

i) $\mathcal{M}_{\rm MF}$: The Fig. 1.10, top panel, shows the cumulative distribution from the centre for the particles as a solid line and, with a dashed line the ten most massive stars. This method detects MS even when was though for uniform distributions.

ii) $\Lambda_{\rm MST}$: The Fig. 1.10, middle panel, shows the level of MS dependent of number of most massive stars. The method reflects a high level of MS for the ten most massive stars (5.3 ± 1.0), but decreasing to very low levels when most of the stars are used.

iii) $\sum_{\rm LDR}$: The Fig. 1.10, bottom panel, shows the stellar surface density according to each individual mass. The blue dashed line is the average $\sum$ for low mass stars and the red solid line the average for the ten most massive stars, resulting in a $\sum_{\rm LDR} = 0.58$, i.e. no MS. This is because that the most centrally located stars are located in areas with relativity low surface density.

From the distribution shown in Fig. 1.9 is possible to appreciate that the massive stars are preferentially concentrated. $\mathcal{M}_{\rm MF}$ and $\Lambda_{\rm MST}$ detect MS and $\sum_{\rm LDR}$ does not.

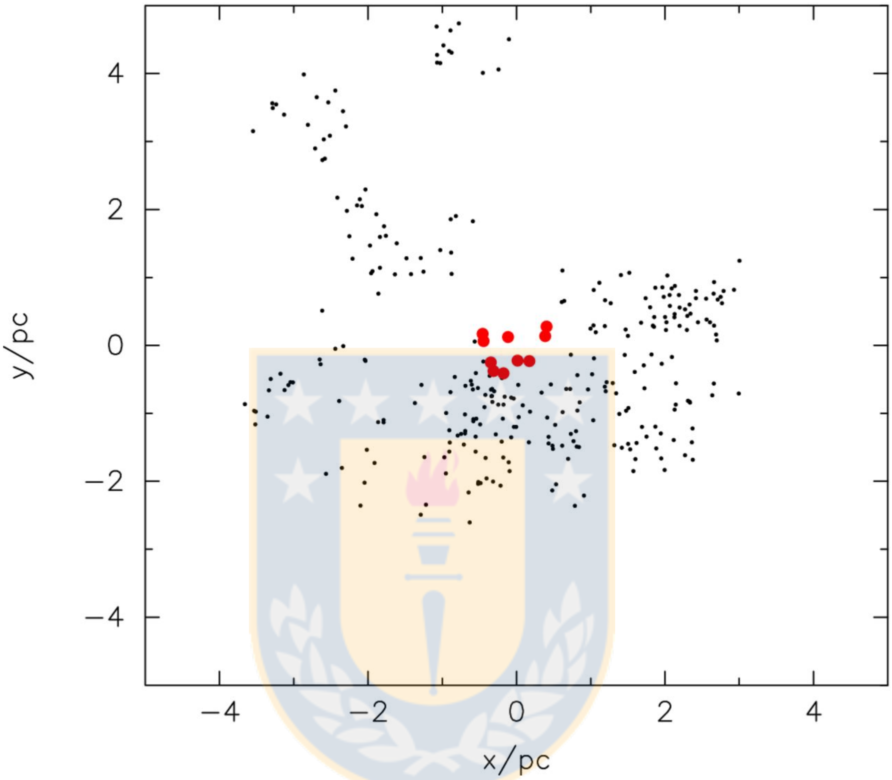

FIGURE 1.9: Substructured distribution with stars drawn from an initial mass function and placed preferentially centred in the spatial distribution. The ten most massive stars are shown by the larger (red) points. Image taken from Parker & Goodwin (2015).

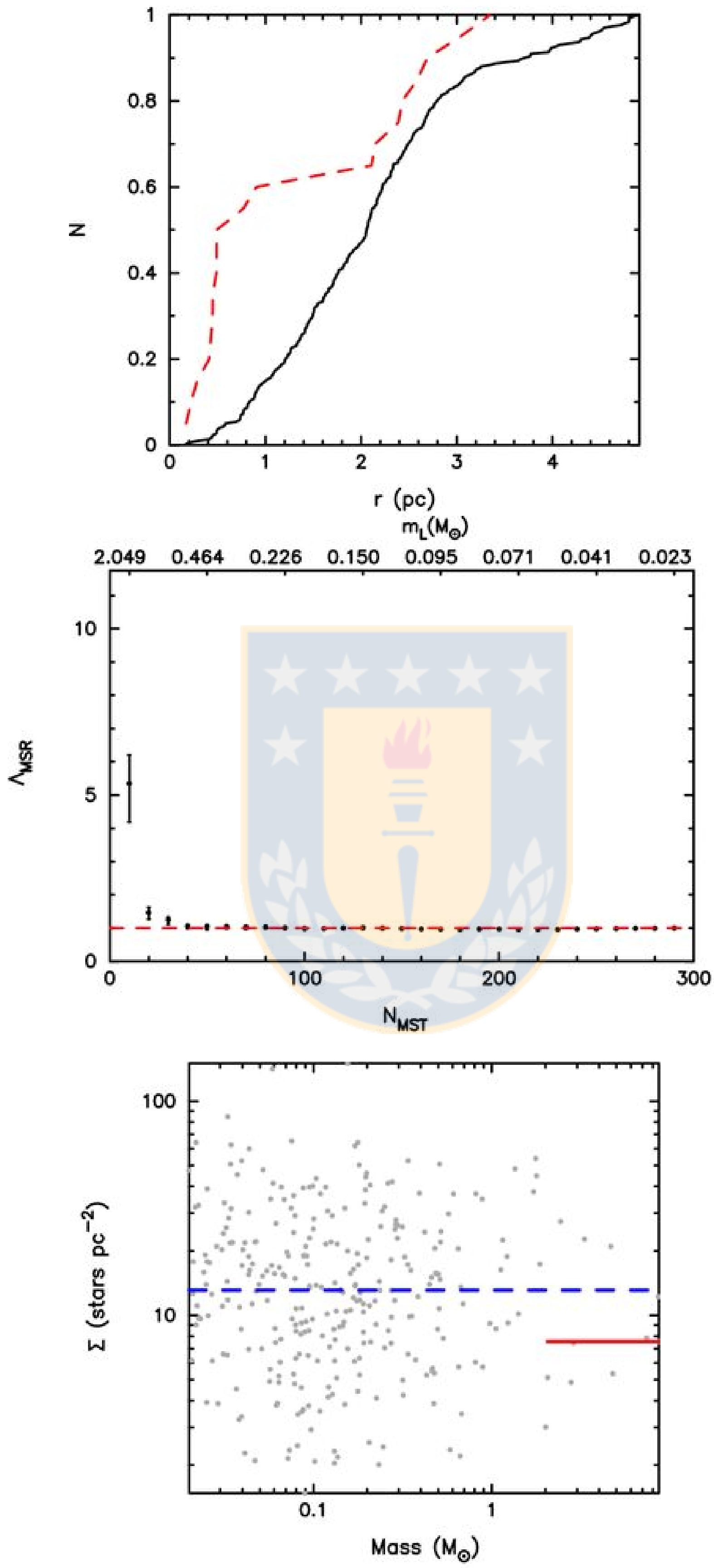

FIGURE 1.10: Three separate measures of mass segregation for the stellar distribution shown in Fig. 1.9. In top panel is showed the cumulative distribution ($\mathcal{M}_{\rm MF}$) of the distance from the centre for the ten most massive stars (the red dashed line) and the cumulative distribution for all stars (the solid black line). In the middle panel is showed the $\Lambda_{\rm MST}$ value as a function of the $\rm N_{MST}$ i.e. stars used in the subset. In bottom panel is showed local stellar surface density versus stellar mass ($\sum_{\rm LDR}$). The median stellar surface density for the ten most massive stars is shown by the solid (red) horizontal line and the median surface density for all of the stars is shown by the blue horizontal dashed line. Images taken from Parker & Goodwin (2015).

As a third test Parker & Goodwin (2015) located the most massive stars in locations with high local surface densities as Fig 1.11 shows. The classical picture of MS now is observed in locations with high surface densities.

i) $\mathcal{M}_{\mathrm{MF}}$: The Fig. 1.12, top panel, shows the cumulative distribution from the centre for all the particles with a solid line and, with a dashed line for the ten most massive stars. This method detects MS, but as this method lacks statistics the level of MS is not well represented.

ii) Λ_{MST}: The Fig. 1.12, middle panel, shows the level of MS dependent of number of most massive stars. The method reflects a level of MS for the ten most massive stars (2.7 ± 0.5), but decreasing to low levels but still detecting values > 1 for the 30 most massive stars.

iii) $\sum_{\mathrm{LDR}}$: The Fig. 1.12, bottom panel, shows the stellar surface density according each individual mass. The blue dashed line is the average $\sum$ for low massive stars and the red solid line the average for the ten most massive stars, resulting now due the high local densities where the most massive stars are located, in a $\sum_{\mathrm{LDR}} = 4.9$, i.e. detecting MS. This is not a surprise because this was the scenario to which was created matching exactly with the definition for this method.

Is possible to say that for this scenario the three method agree in find MS, as is expected for observer watching this kind of configuration.

Parker & Goodwin (2015) concluded that the even when Λ_{MST} and $\sum_{\mathrm{LDR}}$ can detect MS as the classical picture, the last agree only if the local surface density is high around the most massive stars. In consequence only Λ_{MST} is excluding all the issues previously tested and a more reliable level of MS is detected.

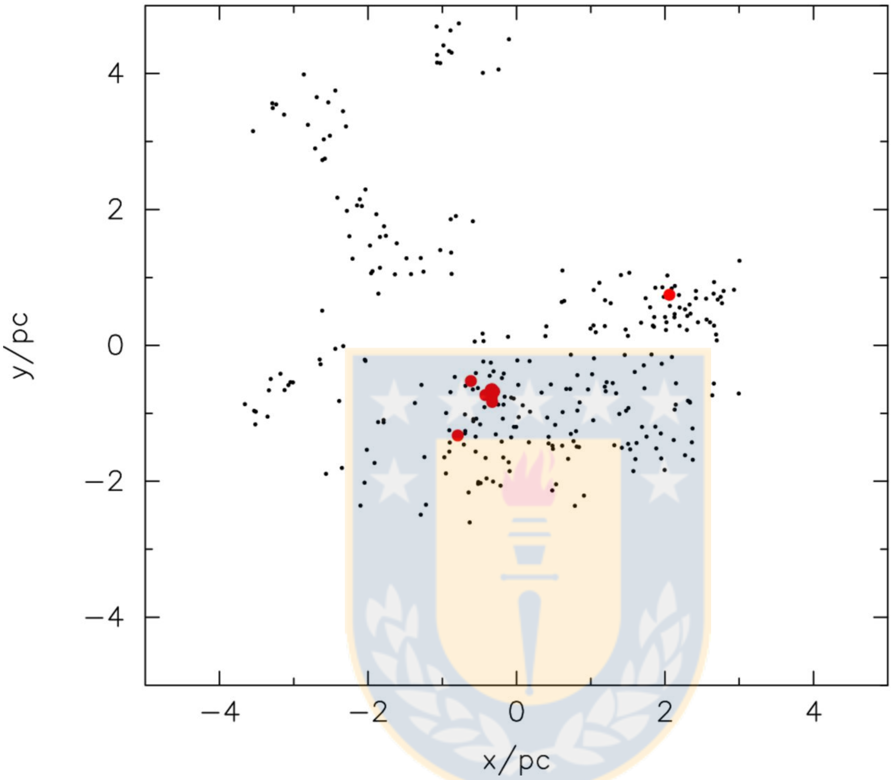

FIGURE 1.11: Substructured distribution with stars randomly drawn from an initial mass function and placed in locations with high local surface densities. The ten most massive stars are shown by the larger (red) points. Image taken from Parker & Goodwin (2015).

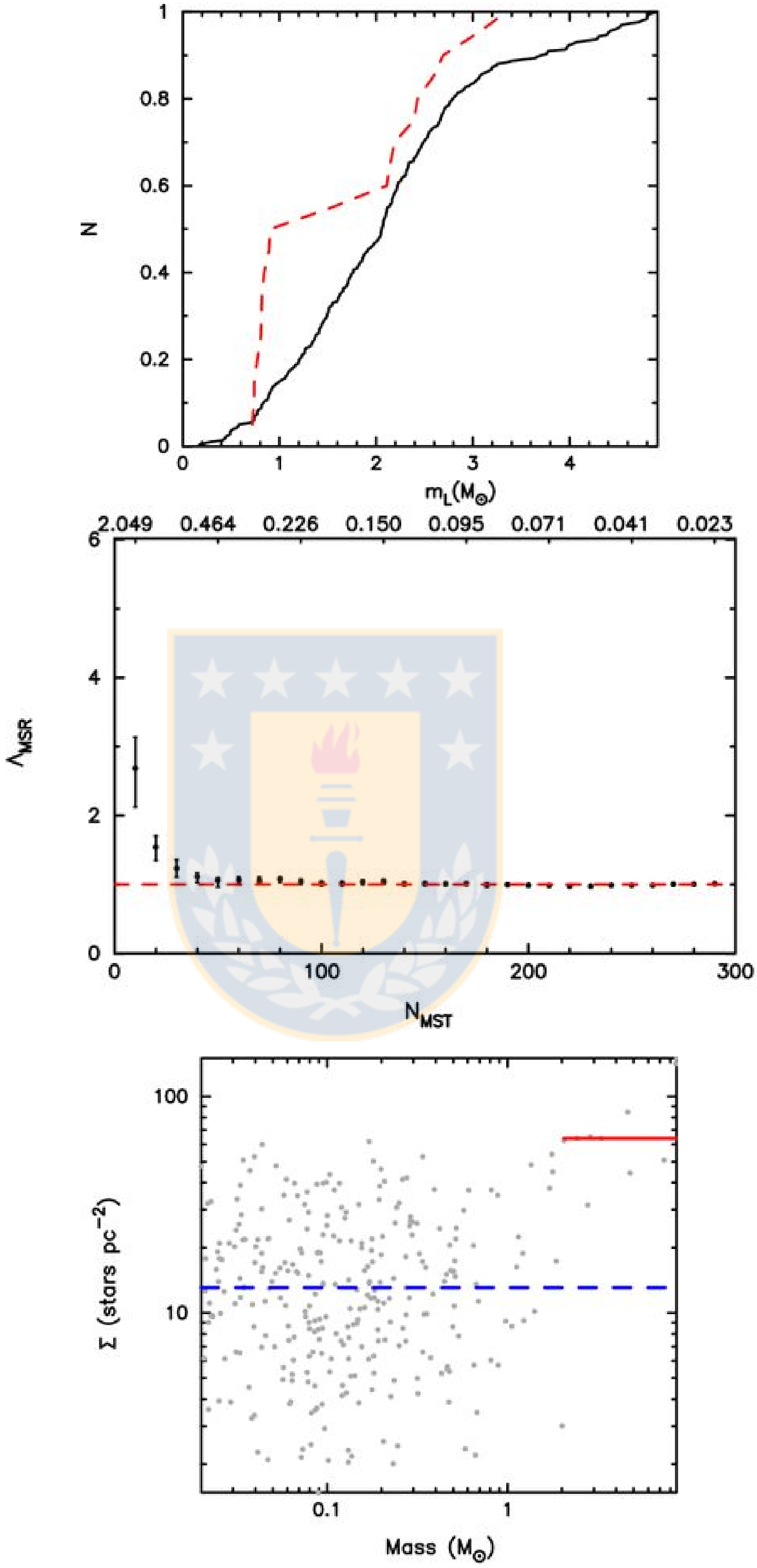

FIGURE 1.12: Three separate measures of mass segregation for the stellar distribution shown in Fig. 1.11. In top panel is showed the cumulative distribution ($\mathcal{M}_{\rm MF}$) of the distance from the centre for the ten most massive stars (the red dashed line) and the cumulative distribution for all stars (the solid black line). In the middle panel is showed the $\Lambda_{\rm MST}$ value as a function of the $\rm N_{MST}$ i.e. stars used in the subset. In bottom panel is showed local stellar surface density versus stellar mass ($\sum_{\rm LDR}$). The median stellar surface density for the ten most massive stars is shown by the solid (red) horizontal line and the median surface density for all of the stars is shown by the blue horizontal dashed line. Images taken from Parker & Goodwin (2015).

1.6.3 Overview of Star evolution

Stellar evolution is called to the process which a star changes over the course of time. Depending on the mass of the star, normally in the range of $0.1 - 60$ M$\odot$, its lifetime can reach from a few million years for the most massive to trillions of years for the least massive. The time of life is directly related with the nuclear-reaction time which produce a finite time of survival, of the order of $t_{\rm nuc} \approx 10^{10}(M/{\rm M}_{\odot})^{-2.5}$ (Padmanabhan, 2001). The mass of the formed star strictly describes the post-main-sequence evolution, with high mass stars characterised by convective cores and low mass stars by radiative cores.

1.6.3.1 Evolution of High Mass Stars

Starting converting in the core H to He by nuclear reactions, following the path 1-2 in Fig. 1.13, until practically turn to a He-core surrounded by a shell of H. This lead to a heavy core which decreases the pressure. To increase the density and temperature the star contracts producing an increasing of the overall star luminosity to reach the point 3. The H still present in the shells stars to burn because of the increasing temperature of the core after the contraction, expanding very fast the shell passing trough 4 and 5. This process going on decreasing the envelope temperature significantly moving until 6. A convective zone is produced in the outer layer increasing the luminosity reaching 7. The core which was contracting since 2 finally can reach an enough temperature ($\sim 10^8$ K) to start the He burning and stopping the contraction and again starting to expand. Contrary to the expansion the outer shells start to contract, this last move the star from 7 to 8. The He burning takes the star from 8 to 10 increasing the temperature and luminosity. As in the previous behaviour but now with He, the decreasing of the available quantity of fuel on the core produce decreasing of a temperature reaching 11. The stars respond contracting to increase the temperature and luminosity until 12 where the high temperature of the core produce a He burning in the outer layers until 12. At this point, the shell starts to contract until 14.

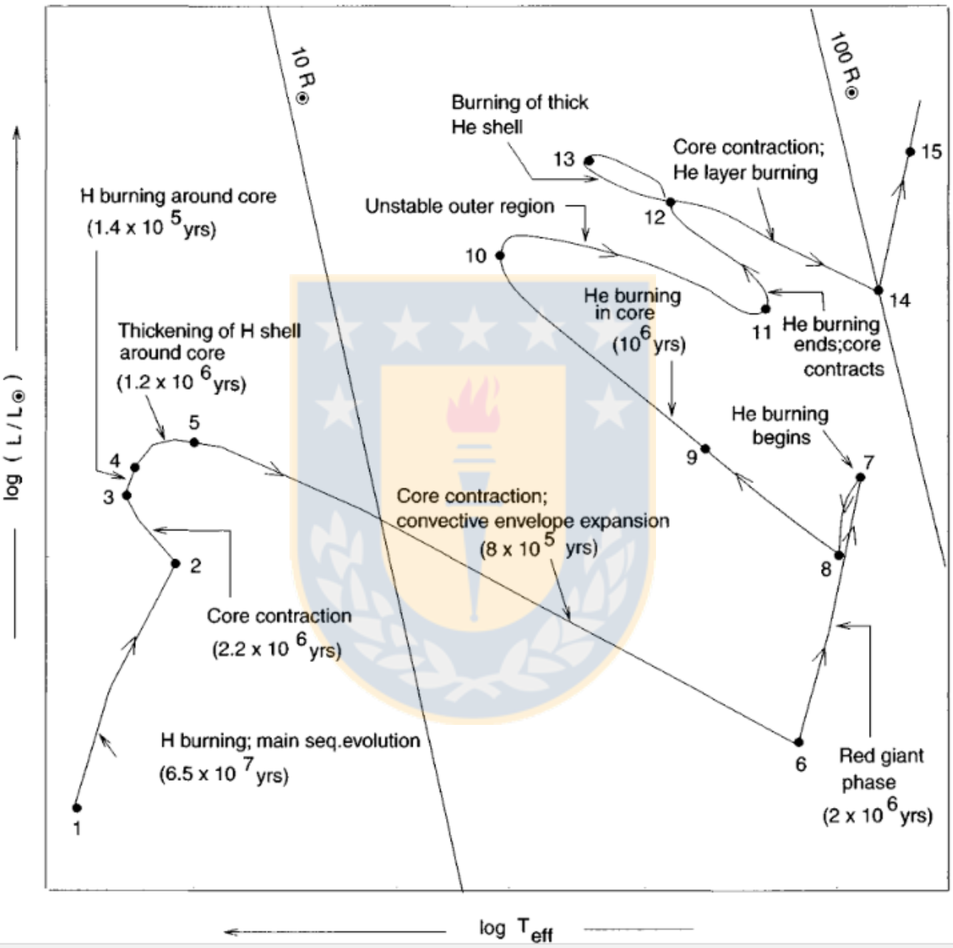

FIGURE 1.13: Path of low mass star evolution. Image taken from (Padmanabhan, 2001).

1.6.3.2 Evolution of Low-Mass Stars

For stars with masses, lower than $\sim 2.3\ M_{\odot}$ the global evolution is produced in a very slow way. The path of the evolution is showed in Fig. 1.14, starting burning H and a small expansion (1-2) due to lower temperatures in comparison with massive stars. As in the massive case, the core reacts contracting to reach 3 with an almost exhausted core of H. The core remains contracting to produce in 4 the H-burning in the outer layers until 5. With a very degenerate core, a slow cored contraction and a significant shell expansion are produced reaching high luminosities between 5-8. Enough temperature in the core produced at 8 where the He flash starts followed by the core He burning. The process between 1-2 is repeated now reaching 10. In this range the star in present in the asymptotic giant branch.

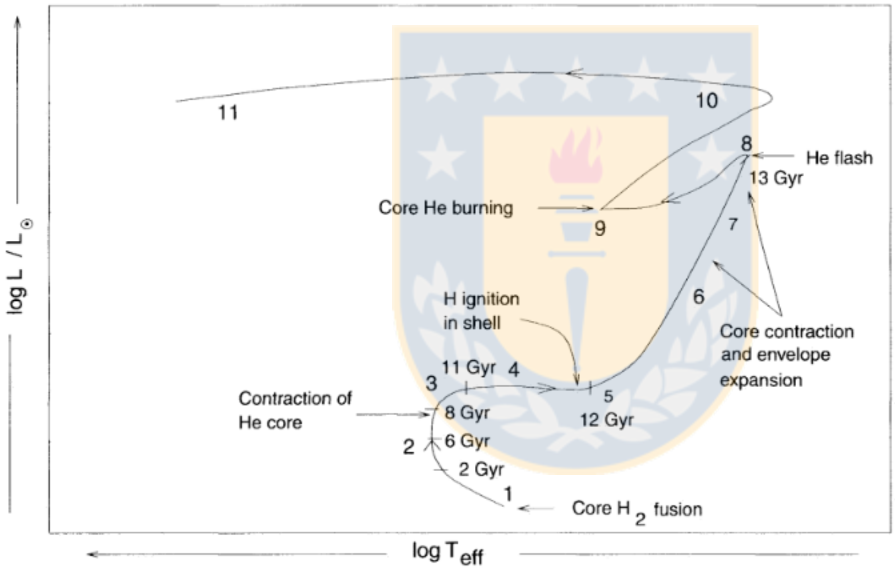

FIGURE 1.14: Path of low mass star evolution. Image taken from (Padmanabhan, 2001).

TABLE 1.2: Parameters of stars depending of their masses. From T. Padmanabhan - 2001

Mass range	Core Fuel	Lifetime	final stage	Comment
$M \leq 0.08\ M_{\odot}$	-	-	brown dwarf	No H burning.
$0.08 \leq M \leq 0.5\ M_{\odot}$	H	-	He white dwarf	He burning never starts.
$0.5 \leq M \leq 2.2\ M_{\odot}$	He	1-15 Gyr	CO white dwarf	He flash is produced in a degenerate core, liberating He and N to the ISM.
$2.2 \leq M \leq 8\ M_{\odot}$	He	10^7-10^9 years	CO white dwarf	He flash is produced in a non degenerate core, liberating He, C,N,O to the ISM. The lifetime range is 10^7-10^9 years.
$8 \leq M \leq$ 10-12 $M_{\odot}$	C,O	$< 10^8$ years	Supernova type II	Contributing principally to the ISM with He. Heavy elements remain captured by the collapsed core..
$12 \leq M \leq 40\ M_{\odot}$	Heavy elements	$\sim 10^6$ years	Neutron star	Contributing to the ISM with O, Ne, Mg, Si, S, Ca. A neutron star of $\sim 1.4\ M_{\odot}$ or black hole is produced.
$M > 40\ M_{\odot}$	Heavy elements	$< 10^6$ years	-	Evolution poorly understood.

1.6.3.3 Final-Stage of Stars

The final stages of the stars are in direct relation with their mass. For very low mass stars, is possible that the He burning could never be produced because of the low level of conversion of H to He. This produces a decrease in the temperature when the H run out. For stars until $\sim 8\ M_{\odot}$ can reach further steps from H to He, then to carbon and oxygen producing a more massive core, contracting and increasing the density. If the core loses their hydrostatic equilibrium will lead to a strong collapse. The time in which the complete process is produced for low mass stars is in the order of Gyr contrary to the case of high massive stars when a star die in the order of Myr. The Tab. 1.2 resume some properties for different ranges of masses.

1.7 Infant mortality

In the previous section it have been described that two different phases of young SCs, embedded SCs turn to naked open SCs in a non generic way. The process in which the molecular gas is expelled either by energy injected by proto-stellar jets, energy radiations from massive stars or supernovas explosion can remove the remaining gas (see Lada & Lada (2003)). The process is not possible to follow complete observationally, due the long human-scales, only snapshots are available which are used by simulations to fill the gaps.

Lada & Lada (2003) compared the frequency of SCs for each phase, comparing with the age as the Fig. 1.15 shows. Solid line shows the number of embedded SCs and embedded SCs. In the first bin all the embedded SCs are found. The dashed line is a prediction of the expected number of open SCs with a constant star formation. The discrepancy between the prediction and the frequency observed confirm that $\sim 4\%$ of the embedded SCs can emerge from their natal gas.

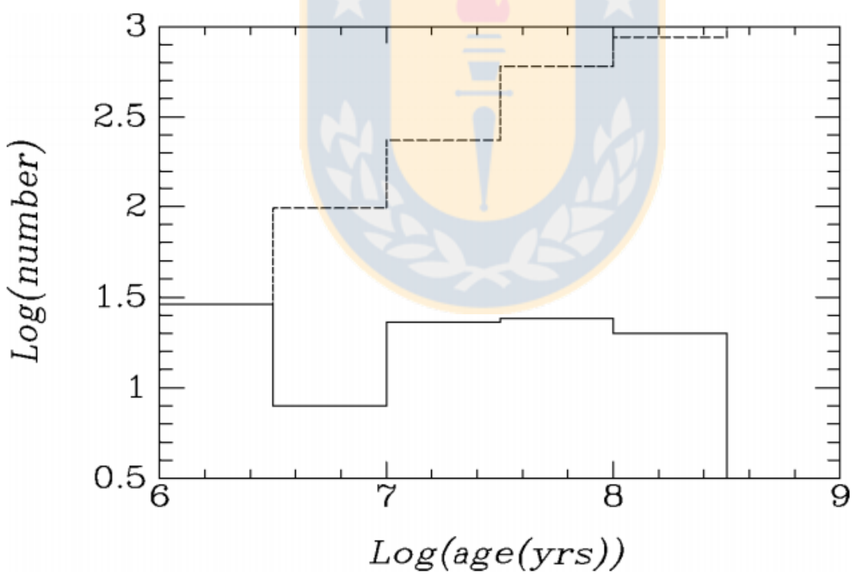

FIGURE 1.15: Observed frequency of naked SCs and Embedded SCs against age showed by solid line. Expected frequency assuming a constant SF denoted by dashed line. From Lada & Lada (2003)

Chapter 2

Codes to use

2.1 IMF Generator

To generate different samples of IMF for the simulations, the code use an inverse cumulative distribution function. The equations of Kroupa (2002) are analytically integrated and then a Monte Carlo method is used to generate random mass samples, from which the IMF distribution is selected. The equations of Kroupa (2002) are divided by mass region as follow:

$$N(M) \propto \begin{cases} M^{-0.3} & m_0 \leq M/\mathrm{M}_{\odot} < m_1 \\ M^{-1.3} & m_1 \leq M/\mathrm{M}_{\odot} < m_2 \\ M^{-2.3} & m_2 \leq M/\mathrm{M}_{\odot} < m_3 \end{cases} \tag{2.1}$$

with $m_0 = 0.01$, $m_1 = 0.08$, $m_2 = 0.5$, $m_3 = 50\ \mathrm{M}_{\odot}$.

The Fig. 2.1 shows different samples for different total masses. The three intervals follow the values of the slopes of Kroupa (2002). For these samples we use more than three thousands masses to ensure enough statistic.

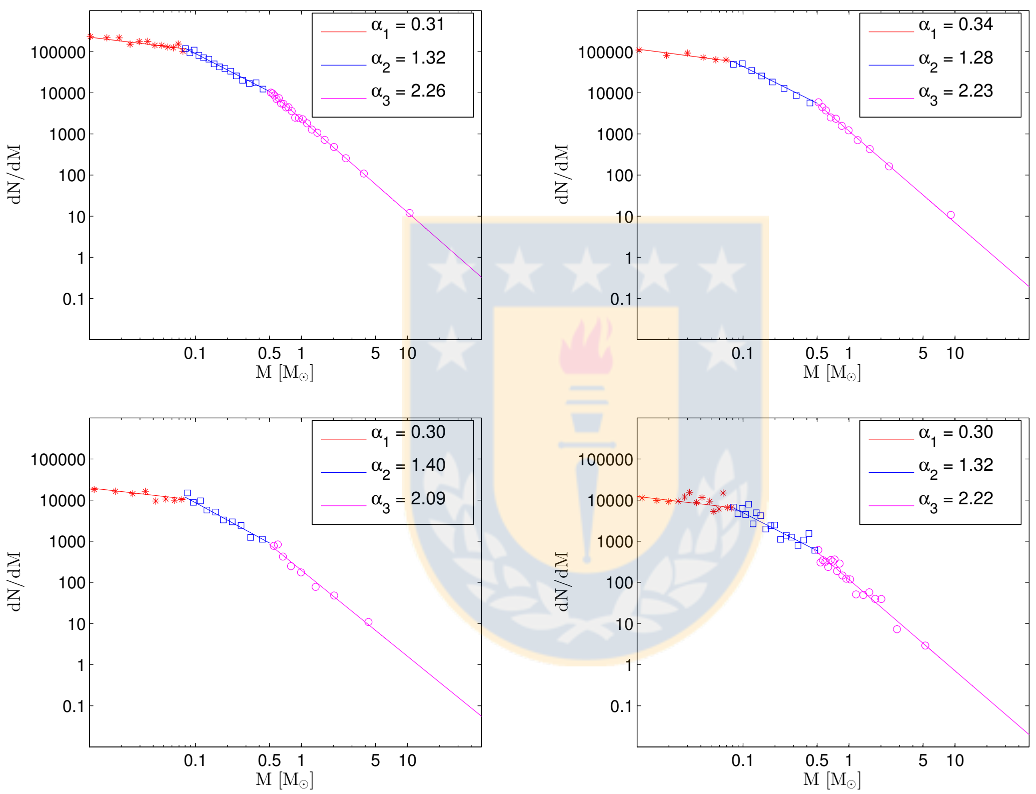

FIGURE 2.1: Different samples reproducing Kroupa IMF (2002). Top-left: total mass 10.000 $M_{\odot}$. Top-right: total mass 5.000 $M_{\odot}$. Bottom-left: total mass 1.000 $M_{\odot}$. Bottom-right: total mass 500 $M_{\odot}$. From this work.

2.2 Fractal Generator

Advances in observations have shown that star clusters form in a substructured way (Larson, 1995; Elmegreen, 2000; Testi et al., 2000; Williams, 2000; Cartwright & Whitworth, 2004; Gutermuth et al., 2005; Schmeja & Klessen, 2006; Carpenter & Hodapp, 2008; Schmeja et al., 2008), and this has also been supported by simulations (Klessen & Burkert, 2000, 2001; Bate et al., 2003; Bonnell et al., 2003; Bate, 2009; Offner et al., 2009)

Goodwin & Whitworth (2004) introduced a method to generate initial sub-structured distributions. This method defines a cube of size $N_{\rm div} = 2$ of which the fractal is created. Starting in the center of the cube with a first-generation parent which is divided in $N_{\rm div}^3$ sub-cubes. Each sub-cube, called child, can turn into a parent for the next generation with a probability of $N_{\rm div}^{(D-3)}$ where D is the fractal dimension. The probability to become a parent is clearly ruled by the value of the fractal dimension, for lower D less children turn to parents so a more sub-structured distribution is produced. A value of $D = 3$ correspond to a uniform distribution. The not surviving children are removed from the box, then a small noise is added to the remaining survivors moving them very close around the actual position, to prevent an artificial grid-like structure and finally they become parents for the next step. The mature children or new parents are divided into $N_{\rm div}^{(3)}$ new children each of which $N_{\rm div}^{(D-3)}$, the same probability than before, become a parent. The process is repeated until the number of children reaches a larger number than the number of particles. The velocities of the children are inherited of the parents including a random component that decreases with each new generation. The velocities of the parents follow a Gaussian with a mean of zero and the children inherit the velocity from the parent including a random component that decreases with each new generation

Examples of different fractals, changing only the fractal dimension are shown in Fig. 2.2, in 2D, for a better appreciation. Top panel shows a fractal with a value of $D = 1.0$ i.e. a very clumpy distribution. The value of D is increasing to the bottom until produce a uniform distribution, which correspond to a value of $D = 3.0$.

FIGURE 2.2: Examples of fractal distribution for different fractal dimensions. Top-left fractal with D=1.0. Top-right fractal with D=1.6. Bottom-left fractal with D=2.0. Bottom-right fractal with D=3.0. From this work.

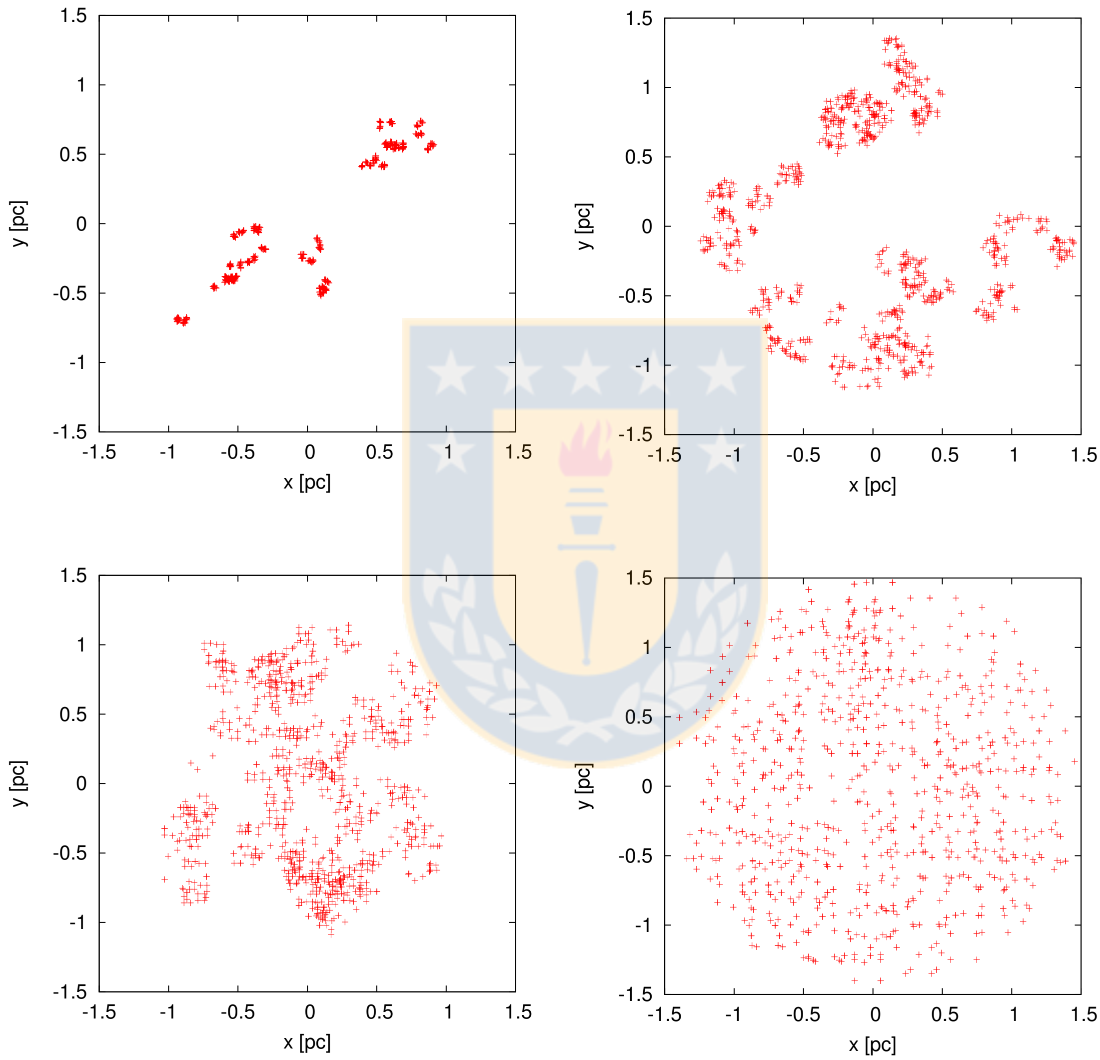

2.3 Nbody6

This code was developed by Aarseth (2003) and is continuously updated. The code is a direct N-body code i.e. solves all the forces involved in equation:

$$\mathbf{F} = G \sum_{i \neq j}^{N} \frac{m_i m_j}{{r_{ij}}^2} \tag{2.2}$$

with G the gravitational constant, m_i and m_j to different masses and r_{ij} the distance between them.

The code incorporates several developments to improve the speed and accuracy. It has been thought to study a variety of problems involving point-mass interactions with emphasis on realistic SCs models.

The programing language is Fortran 77 with more than 216 routines with some of the main features:

- Ahmad-Cohen neighbour scheme (Ahmad & Cohen, 1973). This scheme uses different time-steps depending of a predefined radii.
- External tidal field, which is added to the equations using the Hermite integration with hierarchical time-block steps (Makino, 1991).
- Stumpff KS formulation with Hermite integrator (Mikkola & Aarseth, 1998). This solves interactions of compact subsystems as binaries.
- Stability of hierarchical systems (Mardling & Aarseth, 1999). With a semianalytical criterion can hold the stability for this kind of systems for a wide range of mass ratios and arbitrary outer eccentricities
- Chain regularization of compacts sub-systems (Mikkola & Aarseth, 1993). This regularization treats the interaction between hard binaries and a single star or other binaries.
- IMF (e.g. Kroupa, 2002) and Synthetic stellar evolution (Hurley et al., 2000).
- Instantaneous tidal circularizations for detached binaries and collisions.

The code is free to download from the web and can be used to run simple simulations on workstations or laptops. Nbody-6 allows to use an external field i.e. smooth tidal field or a gas cloud. In our simulations, we use the analytical potential to mimic a gas-cloud in which the stars are embedded.

2.3.1 Gas Cloud

The gas potential in a star forming cloud ca be complicated to describe in an analytical way and, also can be expensive if it is introduced in a simulation. To avoid this, approximations about the interaction are carried out using smooth background potentials, as we are using in our simulations.

2.3.1.1 Uniform Potential

A simplistic approach to the gas can be modeled as uniform sphere of mass M_{u} and a constant density $\rho_{\mathrm{u}} = \frac{3M_{\mathrm{u}}}{4\pi R_{\mathrm{u}}^3}$ which will produce a potential of the form:

$$\phi(r) = -\frac{GM_{\mathrm{u}}}{2}\left[3 - \frac{r}{R_{\mathrm{u}}}\right] \tag{2.3}$$

with G the gravitational constant, M_{u} the total mass of the sphere, R_{u} the radius of the sphere and r the different radius along the BG potential.

Fig 2.3 shows the shape of the uniform BG potential (green solid line) for a $R_{\mathrm{u}} = 1.8$ pc and $M_{\mathrm{u}} = 3455$ $\mathrm{M}_{\odot}$ (values will be justified in the next sections).

2.3.1.2 Plummer Potential

We also express the BG potential as a Plummer sphere, proposed by Plummer (1911), with a dense center and reducing the value with the radius. The density follow the equation:

$$\rho(r) = \frac{3M_{\mathrm{Pl}}}{\pi R_{\mathrm{Pl}}}\left(1 + \frac{r^2}{R_{\mathrm{Pl}}}\right)^{-\frac{5}{2}} \tag{2.4}$$

with R_{Pl} being the scale radius. The profile produces a potential of the form:

$$\phi(r) = -\frac{GM_{\mathrm{Pl}}}{\sqrt{r^2 + a^2}} \tag{2.5}$$

Fig 2.3 shows the shape of the Plummer BG potential (red dashed line) for $R_{\mathrm{Pl}} = 1.0$ pc and $M_{\mathrm{Pl}} = 3472$ $\mathrm{M}_{\odot}$ (values will be justified in the next sections).

The problem with this approximations could be the case where the gas might leave the cluster in certain parts, which produces a non-spherical distribution of the gas. The gas density will vary inside the cluster but the changes in the potential are always much smoother, so the assumption of a spherical gas distribution should have a small influence.

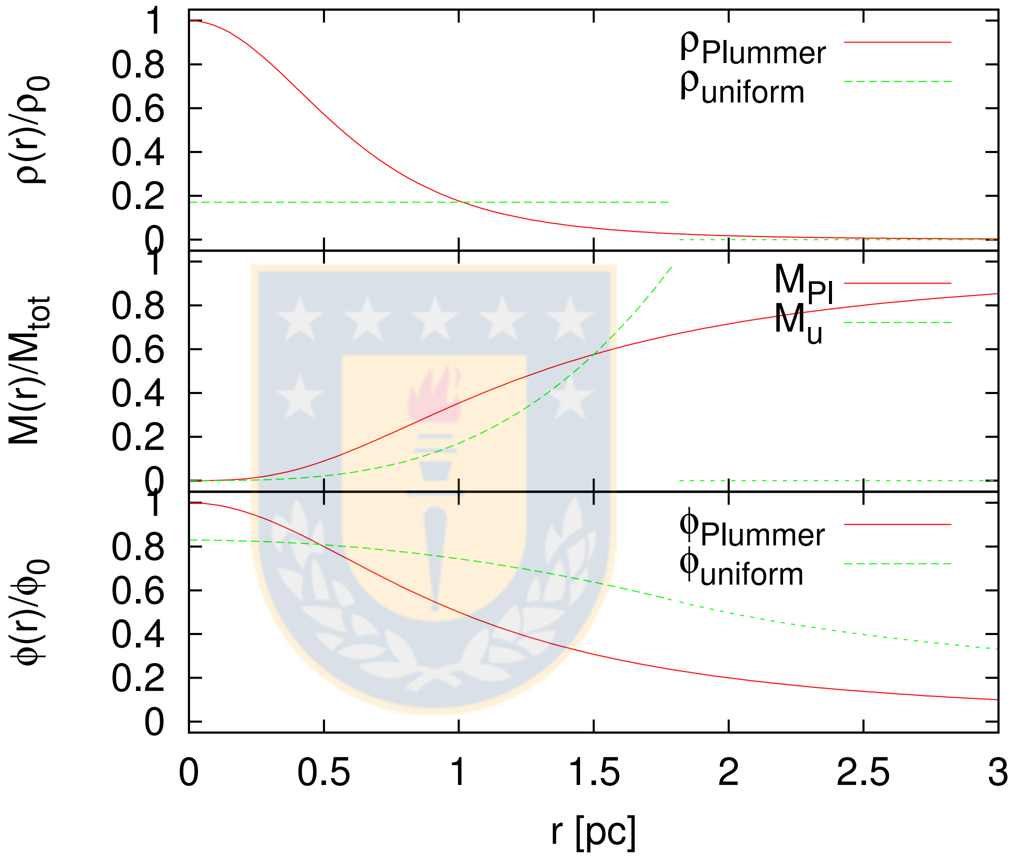

FIGURE 2.3: The top panel shows the normalised curve for the density inside of the spheres. The middle panel shows the normalised quantity of the different spheres. The bottom panel shows the normalised potential produced. Red solid line is for uniform sphere and green dashed line for Plummer sphere. From this work.

2.4 Bound Mass Measurement

We use the snow ball code (Farias et al., 2015) to discard stars which are not bound to the cluster i.e. they have velocities larger than $v_{\rm esc}$.

The code works as follow:

1. The code starts finding over-densities or clumps using a density and number of particles criterion.
2. The gravitational potential is calculated for each clump separately.
3. Depending on the velocities, particles inside can be rejected of kept and, extra stars which initially not belong to the clump can be added if they have velocities less than $v_{\rm esc}$
4. The loop continues until the code can not add or reject more stars i.e. the method converges.

The process is computed for each clump separately which makes it possible to find more than one bound clump. In the top panel of Fig. 2.4 we show an example of a distribution of stars, where it is possible to detect by simple visual inspection at least 4 clumps. The code detects 6 clumps based on their density as the middle panel shows. Visually the most massive clump appears to be the clump close to the left corner with a very massive star in the center. The visual mass is 98.02 $M_\odot$ and the second more massive clump in the bottom of the panel has 73.64 $M_\odot$. The code after it converges finds the bound particles shown in the bottom panel and, the most massive clump now is located at the bottom with 68.84 $M_\odot$, which is a bit bigger than the 64.71 $M_\odot$ of clump in the left corner. The rest of the clumps have masses much smaller. The data for each clump is summarized in Tab. 2.1.

TABLE 2.1: Data of measurements for Fig 2.4. First column: Clump number identification. Second and third column: Position x-axis and y-axis respectively. Fourth column: Number of bound particles. Fifth and sixth column: Visual and bound mass respectively. From this work.

# clump	x[pc]	y[pc]	$N_{\rm bp}$	Visual Mass	Bound Mass
1	-6.30	20.10	80	98.02	64.71
2	-0.24	-22.22	104	73.64	68.84
3	2.83	14.69	89	39.87	45.12
4	-10.72	-0.46	43	23.16	16.83
5	14.12	-15.04	25	18.72	10.13
6	6.21	3.78	9	8.83	4.26

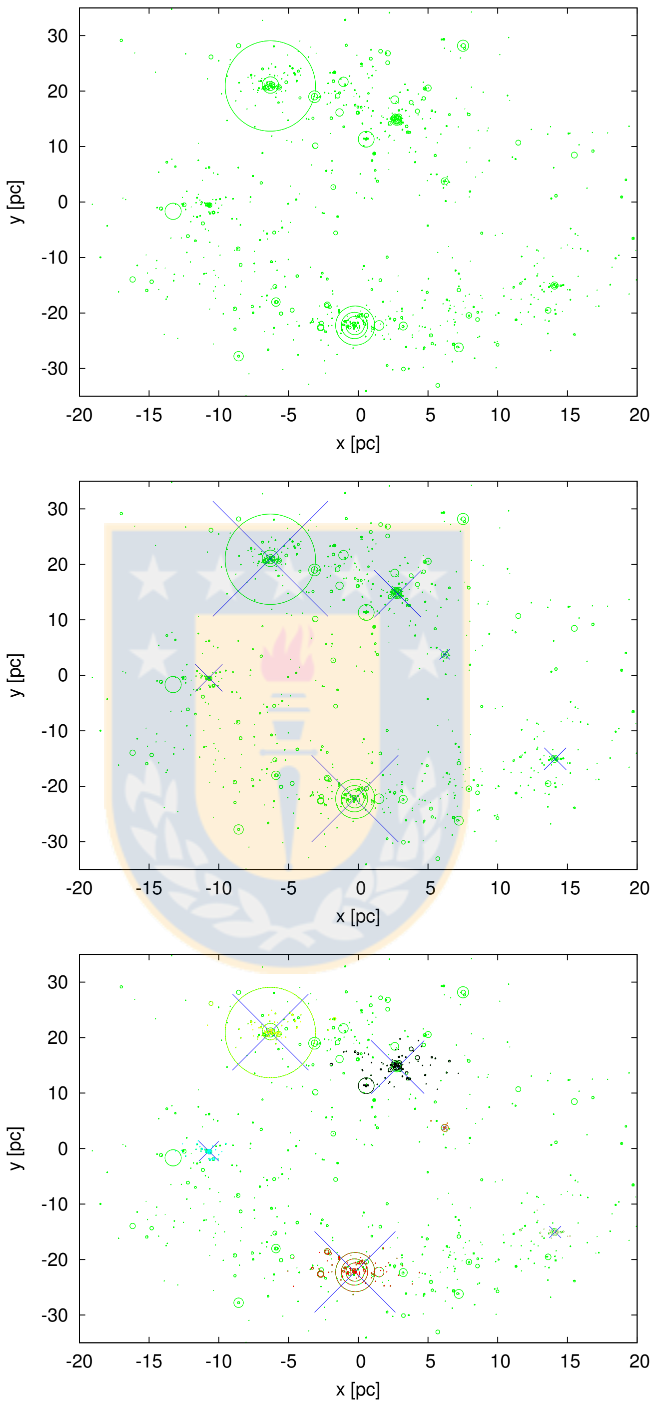

FIGURE 2.4: Snapshots of the process to find bound particles. Top panel: Example of particles distribution. Middle panel: Detected clumps. Bottom panel: Bound particles of each clump. The size of each symbol is a direct representation of its mass. From this work.

Chapter 3

Mass Segregation Evolution

3.1 Aim

By means of N-body simulations, we follow the evolution of MS, using the method of (Allison et al., 2009), in embedded SCs. We observe under which conditions it is more probable to find a significant level of MS testing different mass distributions, virial ratios and BG potentials. A more specific explanation will be given in each section.

3.2 Previous Works

MS is a topic which has been very well studied (see. Sec 1.6.2) and all authors conclude that MS is a process which is produced no matter the initial conditions, only affecting the final level of MS. In the theoretical studies, using N-body simulations, the effect of the embedded phase has been neglected. Simulations start from a naked SC which initially can shows a significant level of MS as a result of the star formation process or purely dynamical (see Sec. 1.6.2). All the studies conclude that the level of MS becomes bigger than the initial value. Massive stars inject energy to the low mass stars producing the expansion and the massive stars fall to the inner parts, showing MS.

3.3 Method

- We emulate the initial state of a SC with substructured distributions. To generate these kind of distribution we used the method of Goodwin & Whitworth (2004) (see Sec. 2.2) with a value of D=1.6 and a total radius of $R = 1.5$ pc.

- We assig different masses according to a modified Kroupa IMF (2002):

$$N(M) \propto \begin{cases} M^{-1.30} & m_0 \leq M/\mathrm{M}_\odot < m_1 \\ M^{-2.30} & m_1 \leq M/\mathrm{M}_\odot < m_2 \\ M^{-2.35} & m_2 \leq M/\mathrm{M}_\odot < m_3 \end{cases} \tag{3.1}$$

  to our stars, with $m_0 = 0.08$, $m_1 = 0.5$, $m_2 = 1.0$, $m_3 = 50$ $\mathrm{M}_\odot$. We are interested only in the stellar component, so we do not use the substellar mass range (below 0.08$\mathrm{M}_\odot$ for brown dwarfs). The total mass of the generated stars is ~ 500 $\mathrm{M}_\odot$ for ~ 1000 stars which are common values for small and young SCs (Piskunov et al., 2008). We call massive stars to all the stars with $M > 4\mathrm{M}_\odot$. Stars less massive are regarded as low mass stars in this work. To generate the masses we use the IMF generator, explained in Sec. 2.1. We use 12 random IMF samples with ~ 500 $\mathrm{M}_\odot$ and ~ 1000 particles. The samples that we use are shown in Fig. 3.1. It is possible to observe that we follow the analytic slopes very closely. This is caused by the low number statistics produced in a random sample of only ~ 1000 stars (Kroupa, 2001). In Tab. 3.1 we show the total mass, total number of particles, number of particles in the ranges given in Eq. 3.1, the number of stars with masses $M > 4$ $\mathrm{M}_\odot$, the number of stars with masses $M > 10$ $\mathrm{M}_\odot$ and the most massive star.

- To locate the massive stars in the distribution we use three criteria and examples of these configurations are showed in Fig. 3.2, projected in 2D for a better appreciation.

  1. NOSEG: We located massive stars randomly though out the distribution. An example of this is shown in panel (1) of Fig. 3.2.
  2. SEGIN: We force all massive stars to be located in a radius $R < 0.5$ pc i.e. inner locations, producing a high level of MS. The panel (2) shows how one of these configurations looks like.
  3. SEGOUT: We force massive stars to be located at radii $R > 1.0$ pc i.e. outer locations. An example of this is shown in panel (3).

  The SEG-OUT case is very unlikely but we analyze it to test the accepted trend of MS occurring no matter the initial conditions.

- The SCs are embedded in two different BG potential. A cuspy potential is emulated by a Plummer Sphere and a flat potential by a uniform sphere. To fix an SFE = 0.2, which is commonly observed for this kind of objects (Lada, 1999; Lada & Lada, 2003; Clark & Bonnell, 2004) the mass enclosed in a radius of 1.5 pc is 2000 $M_\odot$ (see Sec. 2.3.1).

- To investigate the influence of the initial Q we scale our velocities i.e. we change the kinetic energy to ensure values of $Q_{\text{init}} = 0.5$ and $Q_{\text{init}} = 0.2$ (see Sec. 1.4). A value of Q = 0.5 usually signifies that the system is in virial equilibrium, i.e. it is stable and should not be subject to changes. This is only true for well populated spherical systems. Our stellar distributions try to re-arrange themselves into a smaller in size but close to spherical distribution. This produces an initial compression, reaching higher values of Q and then oscillating around the virial state until a stable spherical shape is produced. Starting with a value of $Q_{\text{init}} = 0.2$ will produce a strong compression, as the low velocities lead to a global collapse of the stellar distribution, reaching even higher values of Q than in the previous case and then oscillating around the virial state as well, erasing the fractal distribution even faster. An example of this process is shown in Fig. 3.3. The green dashed line shows the evolution of a fractal with $Q_{\text{init}} = 0.5$ and the blue solid line for the same fractal now starting with $Q_{\text{init}} = 0.2$.

- The simulations evolve for 5 Myr using the Nbody6 code (see Sec. 2.3).

- To measure the evolution of MS, we quantify MS using the Λ_{MST} method (see Sec. 1.6.2.2). The measurements of Λ_{MSR} (see Eq. 1.8) can be very sensible to low mass stars kicked out due to strong two-body interactions, that increases the values of l_{norm}. This can be fixed to some degree, repeating the measurements many times, which we are doing by comparing 1600 samples of low mass stars. Another factor, can be that one massive star escapes from the cluster or is on the way to do so, increasing the length of l_{massive}. Also, a case that increases the value of l_{massive}, is when one or more of the massive stars that belong to the cluster, are still in a very early stage in the process of segregation, i.e. are located far away or a group which is already segregated. These three issues can give us strange information about the real state of the cluster. Trying to avoid these problems, we restrict the measurements of Λ_{MSR} with three conditions:

  1. Only use the most massive stars inside of the half-mass radii (R_h)
  2. If is not possible to find at least eight of the most massive stars ($M \geqslant 4\text{M}_\odot$) inside of R_h, increase the radii until finding the eighth most massive star and start the measurement of the level of MS at that radii that we call r_8.

3. Only use low mass stars inside of $2r_8$, which can be equal to $2R_h$, when at least eight of the most massive are inside of R_h.

We also keep the Λ_{MSR} method with no restrictions, as a way of control and to extract more information about the evolution of MS with time. In Fig. 3.4, we show as an example, the evolution for one fractal with an initial mass distribution SEG-OUT. Note in the top panel, that until ~ 2 Myr some contradictory levels of MS are detected and a the biggest discrepancy before than 1 Myr. The restricted method (blue solid line) recognizes a level of MS ~ 2, but on the other hand, the normal Λ_{MSR} (red dashed line) detects inverse MS. In the bottom panel we see, that some (or all) of the most massive stars are traveling out of the cluster (blue solid line) and then returning almost reaching the R_h (green dashed line), where the contradictory result is measured. The restricted method is detecting that only (or at least) eight of the most massive stars are segregated at that time, but the normal method is taking into account the rest of the most massive stars, which are still on the way to become segregated and this last assumption is supported by the fact that in the later evolution both methods are measuring the same degrees of MS, no matter the restriction. Λ_{MSR} can lead to spurious results with ejections. Λ_{rest} gives spurious result at the beginning for SEG-OUT.

The effects on the final degree of MS depending on the initial conditions will be discussed in the following section where many simulations are taken into account to avoid stochastic results due to the high dependence on the initial conditions of the fractal distributions which can lead to very specific final results far away from the average.

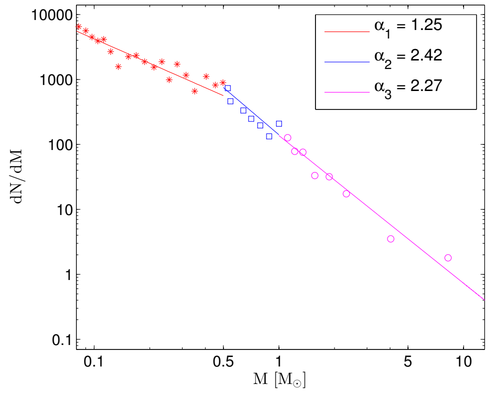

α_1 = 1.25
α_2 = 2.42
α_3 = 2.27
dN/dM
M [$M_\odot$]

(1)

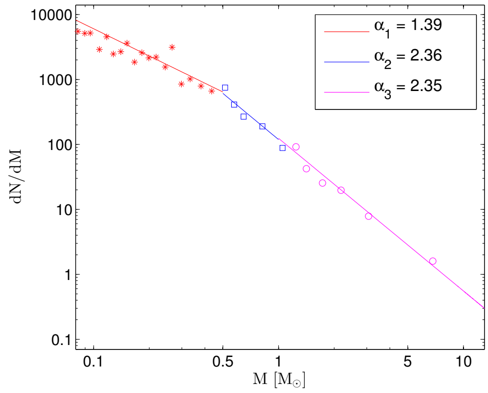

α_1 = 1.39
α_2 = 2.36
α_3 = 2.35
dN/dM
M [$M_\odot$]

(2)

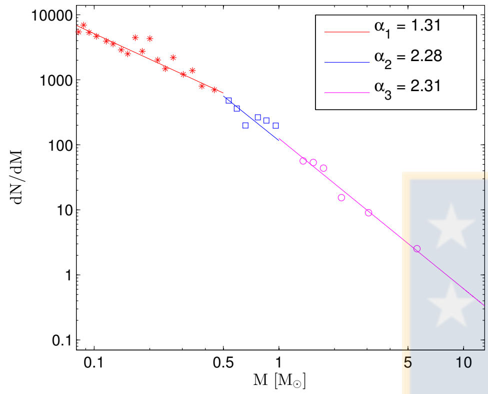

α_1 = 1.31
α_2 = 2.28
α_3 = 2.31
dN/dM
M [$M_\odot$]

(3)

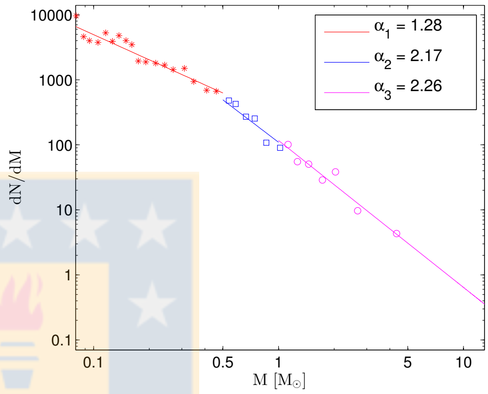

α_1 = 1.28
α_2 = 2.17
α_3 = 2.26
dN/dM
M [$M_\odot$]

(4)

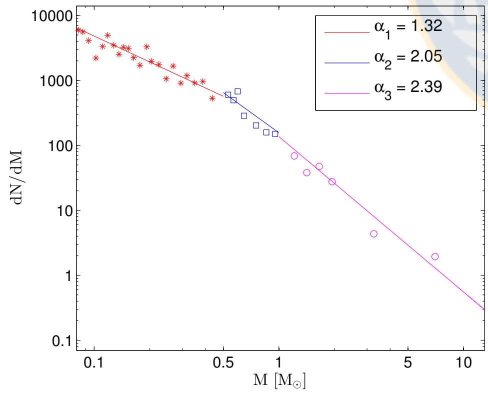

α_1 = 1.32
α_2 = 2.05
α_3 = 2.39
dN/dM
M [$M_\odot$]

(5)

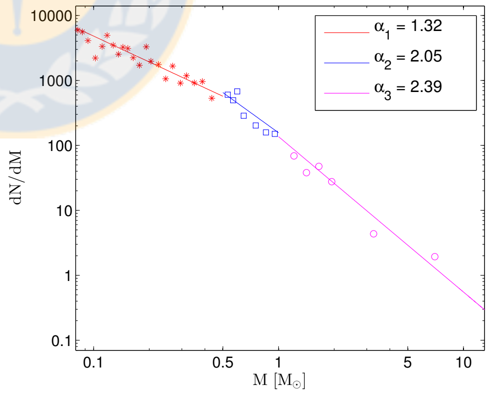

α_1 = 1.32
α_2 = 2.05
α_3 = 2.39
dN/dM
M [$M_\odot$]

(6)

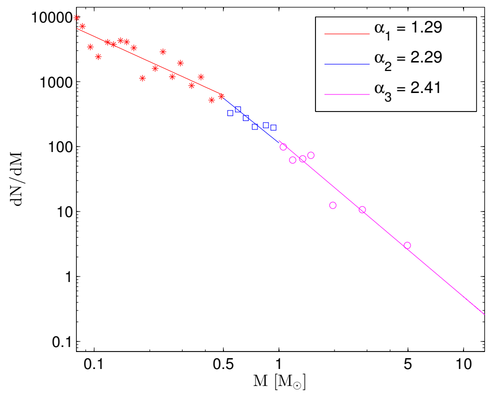

α_1 = 1.29
α_2 = 2.29
α_3 = 2.41
dN/dM
M [$M_\odot$]

(7)

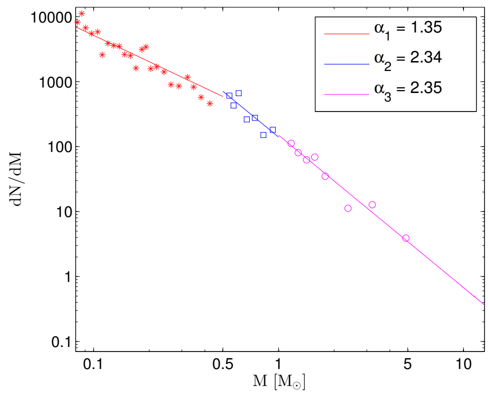

α_1 = 1.35
α_2 = 2.34
α_3 = 2.35
dN/dM
M [$M_\odot$]

(8)

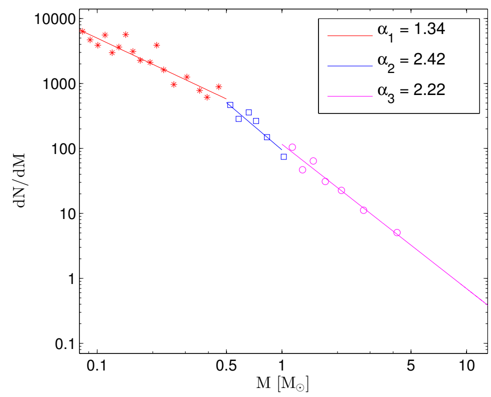

(9)

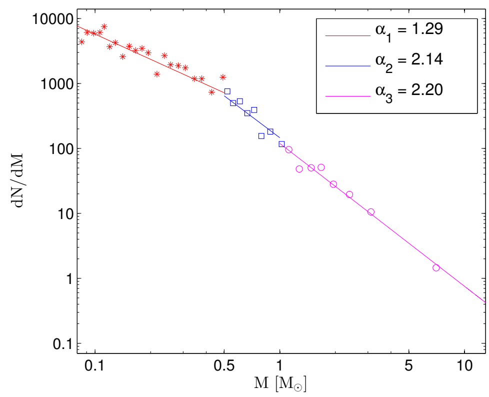

(10)

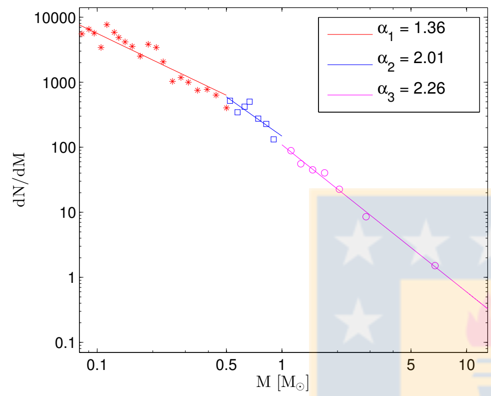

(11)

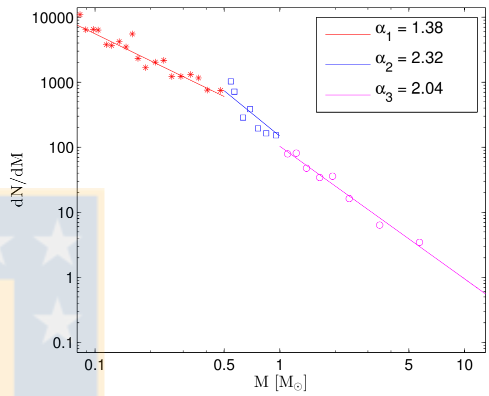

(12)

FIGURE 3.1: Samples of IMF used for the simulations in this work. The different colors is to represent the regions of the masses. From this work.

TABLE 3.1: Summary of properties of IMF samples showed in Fig. 3.1. From this work.

IMF sample row	Total Mass [$M_\odot$]	Number of particles (N_p)	N_p range 1	N_p range 2	N_p range 3	N_p $M \geq 4$ $M_\odot$	N_p $M \geq 10$ [$M_\odot$]	Maximum Mass [$M_\odot$]	Average Mass [$M_\odot$]
(1)	500.39	981	736	150	95	14	2	11.21	0.51
(2)	500.09	955	743	127	85	15	5	20.93	0.52
(3)	500.28	947	734	128	85	16	4	17.83	0.53
(4)	501.25	917	715	115	87	11	4	41.13	0.55
(5)	501.09	915	689	142	84	16	4	22.98	0.55
(6)	500.40	1030	803	137	90	12	1	25.33	0.49
(7)	502.47	905	693	135	77	10	3	40.86	0.56
(8)	502.49	967	716	148	103	15	1	10.51	0.52
(9)	500.11	891	690	114	87	13	3	30.53	0.56
(10)	500.17	1071	834	148	89	9	2	29.06	0.47
(11)	500.09	1002	785	137	80	12	3	37.67	0.50
(12)	500.04	1004	761	150	93	15	2	15.82	0.50

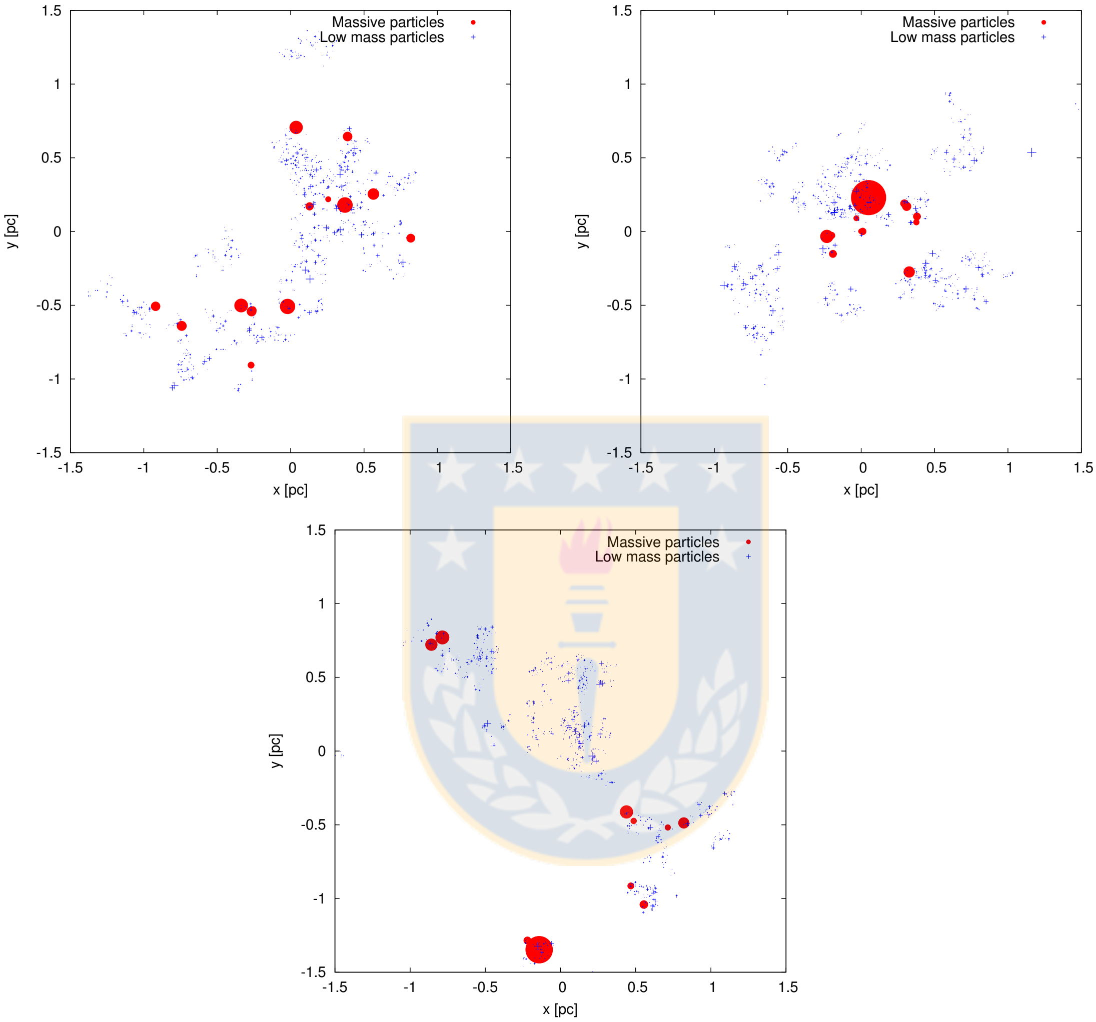

FIGURE 3.2: Examples of the three different initial distribution of massive stars assumed in this work(shown in 2D). Red filled circles are high mass stars and blue points are low mass stars. The sizes of circles and points are proportional to the mass of the stars. Top-left panel: initial fractal with random placements of the masses (NO-SEG). Top-right panel: initial fractal with inside-out segregation (SEG-IN), i.e. the highest mass stars are in the centre of the distribution. Bottom panel: initial fractal with outside-in segregation (SEG-OUT), i.e. the highest mass are further away from the centre. From this work.

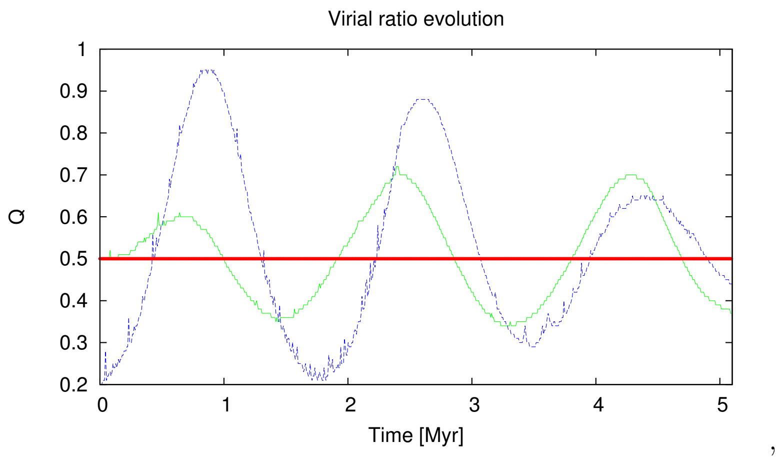

FIGURE 3.3: Example of the evolution of the virial ratio for fractal distributions. The green solid line shows the oscilations for one fractal starting in virial equilibrium (Q = 0.5) and the blue dashed line shows the changes for the same fractal now starting in a cool state (Q = 0.2). Horizontal line denotes the virial equilibrium value of Q = 0.5. From this work.

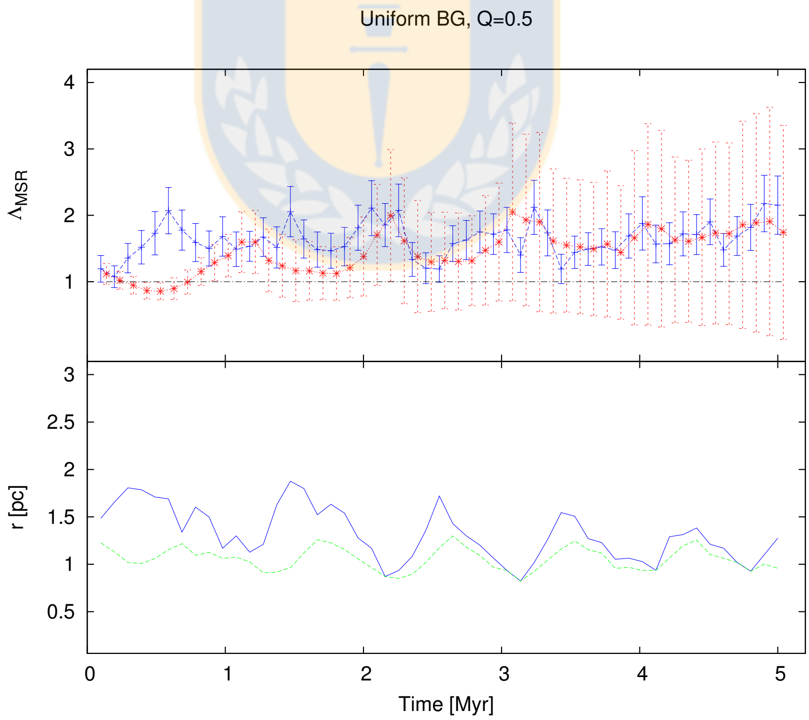

FIGURE 3.4: Example of one fractal with initial mass distribution SEG-OUT, $Q_{\rm init} = 0.5$ and uniform BG. Top panel shows the evolution of $\Lambda_{\rm MSR}$ with the red dashed. The evolution of $\Lambda_{\rm MSR} - R$ method is denoted with the blue solid line. The bottom panel compares the evolution of the r_8 (blue solid line) and the value of R_h (green dashed line). From this work.

3.4 Set of Simulations

We perform, in total, 480 N-body simulations using the direct N-body code NBODY6 with 1000 different mass particles with clumpy initials conditions. We scale the velocities to get sub-virial and virial states. The different configurations are embedded in two different BG potentials.

We use a 12 different fractal distributions (see Fig. 3.2 for the initial mass distributions). For each fractal we draw a different IMF sample for the distribution of the masses, shown in Fig. 3.1. We use four pairs for each set of initial mass placement cases (NO-SEG, SEG-IN and SEG-OUT). For each pair of positions and masses, we generate 10 different random assignments of the masses to the positions according to the NO-SEG rule (using 4 fractal-IMF pairs), 10 random realisations following the SEG-IN rule for its 4 pairs of fractal-IMF realisations and the same for the SEG-OUT case. We have now 160 different initial conditions for each mass distribution.

The complete sample of simulations is showed in Tab. 3.2. We compare the simulations with the same initial conditions producing 40 simulations from where we extracted the information.

TABLE 3.2: Summary of initial conditions of simulations used in this work. From this work.

Initial Distribution	IMF sample	Q_{init}	BG Potential	Number of random realisations
NO-SEG	(1)	0.5	Plummer	10
NO-SEG	(1)	0.5	Uniform	10
NO-SEG	(1)	0.2	Plummer	10
NO-SEG	(1)	0.2	Uniform	10
NO-SEG	(2)	0.5	Plummer	10
NO-SEG	(2)	0.5	Uniform	10
NO-SEG	(2)	0.2	Plummer	10
NO-SEG	(2)	0.2	Uniform	10
NO-SEG	(3)	0.5	Plummer	10
NO-SEG	(3)	0.5	Uniform	10
NO-SEG	(3)	0.2	Plummer	10
NO-SEG	(3)	0.2	Uniform	10
NO-SEG	(4)	0.5	Plummer	10
NO-SEG	(4)	0.5	Uniform	10
NO-SEG	(4)	0.2	Plummer	10
NO-SEG	(4)	0.2	Uniform	10
SEG-IN	(5)	0.5	Plummer	10
SEG-IN	(5)	0.5	Uniform	10
SEG-IN	(5)	0.2	Plummer	10
SEG-IN	(5)	0.2	Uniform	10
SEG-IN	(6)	0.5	Plummer	10
SEG-IN	(6)	0.5	Uniform	10
SEG-IN	(6)	0.2	Plummer	10
SEG-IN	(6)	0.2	Uniform	10
SEG-IN	(7)	0.5	Plummer	10
SEG-IN	(7)	0.5	Uniform	10
SEG-IN	(7)	0.2	Plummer	10
SEG-IN	(7)	0.2	Uniform	10
SEG-IN	(8)	0.5	Plummer	10
SEG-IN	(8)	0.5	Uniform	10
SEG-IN	(8)	0.2	Plummer	10
SEG-IN	(8)	0.2	Uniform	10
SEG-OUT	(9)	0.5	Plummer	10
SEG-OUT	(9)	0.5	Uniform	10
SEG-OUT	(9)	0.2	Plummer	10
SEG-OUT	(9)	0.2	Uniform	10
SEG-OUT	(10)	0.5	Plummer	10
SEG-OUT	(10)	0.5	Uniform	10
SEG-OUT	(10)	0.2	Plummer	10
SEG-OUT	(10)	0.2	Uniform	10
SEG-OUT	(11)	0.5	Plummer	10
SEG-OUT	(11)	0.5	Uniform	10
SEG-OUT	(11)	0.2	Plummer	10
SEG-OUT	(11)	0.2	Uniform	10
SEG-OUT	(12)	0.5	Plummer	10
SEG-OUT	(12)	0.5	Uniform	10
SEG-OUT	(12)	0.2	Plummer	10
SEG-OUT	(12)	0.2	Uniform	10

Chapter 4

Results and Discussion Mass Segregation Evolution

4.1 Mass Segregation Results

In the following sub-sections we present the results for the different initial MS states, namely NO-SEG, SEG-IN and SEG-OUT.

The figure shown for each sub-section shows in the left panels the pseudo-virial initial conditions and in the right panels the results for the sub-virial initial state. The top panels are the uniform background simulations, while the lower panels show the results for the background potential which follows a Plummer distribution. The upper half of each panel shows the evolution of the MS ($\Lambda_{\rm MSR}$ and $\Lambda_{\rm rest}$ respectively) and the lower half the evolution of R_h and r_8. In all figures we show the mean values taken from all 40 realisations of this set of parameters, instead of the results of one single simulation. Again, the unrestricted method is shown as red stars and dashed lines, while the restricted values are given as blue plus-signs and solid lines in the upper part of each panel, while the lower parts show r_8 in solid blue and R_h in dashed green.

4.1.1 NO-SEG

In Fig. 4.1, we see in the top parts of each panel, that both methods pick up a Λ value (here the term Λ refers to both methods) higher than one initially. The restricted method shows a number higher than two, which means a significant level of mass-segregation, even though the high mass stars are randomly placed. The simulations end up with mean values slightly below 3.0.

In the top left panel (uniform BG, $Q_{\rm init} = 0.5$) we see an increase until at about 2 Myr the highest degree of MS is found ($\Lambda_{\rm rest} = 3.17$). After that we see small oscillations around 3. As a final value we assign a mean value of $\Lambda_{\rm rest}$ measured from all data-points between 4 and 5 Myr called $\Lambda_{\rm final}$, which in this case is $\Lambda_{\rm final} = 2.79 \pm 0.77$. We call the time where the level of $\Lambda_{\rm rest}$ remains larger than 2, (i.e., a significant level of MS) $t_{\rm seg}$. In this set of simulations this is always the case and so $t_{\rm seg}$ = always.

In the bottom half of this panel we see small oscillations in R_h, which are damping out with time and settling at a slightly lower value than the initial one, i.e. we see that even in the supposedly virialised case we get a net contraction of the final cluster.

The top-right box is showing the results for the same background potential but now starting in a cool state ($Q_{\rm init} = 0.2$), i.e. undergoing a strong collapse at the beginning. Starting with the same initial degree of MS (as both sets rely on the same initial fractal and mass assignments, just with differently scaled velocities) a faster increase of $\Lambda_{\rm rest}$ is observed reaching the highest value of $\Lambda_{\rm rest} = 3.38$) at already 1 Myr. Then a very slow decrease is visible until it reaches a value of $\Lambda_{\rm final} = 2.66 \pm 0.73$ at the end of the simulations. At the end of the simulations both methods agree well within their errors.

In the bottom half of this panel we can see the strong decrease of R_h, due to the cold initial conditions. Afterwards, we obtain large oscillations until the simulations settle into a final value much lower than in the pseudo-virialised case.

The bottom-left panel shows the results for the Plummer BG potential starting in pseudo-equilibrium. We see a slow rise in MS leveling off at a final value of 2.68 ± 0.66. As the simulations start out with a $\Lambda_{\rm rest} > 2$ to begin with but showing a small dip below 2 at about 0.7 Myr, we assign $t_{\rm seg} = 0.7$ Myr. Both methods give indistinguishable values towards the end of the simulation.

In the bottom half of this panel we see larger error-bars for R_h. This is explainable by the fact that in a uniform sphere we have a well defined free-fall time which is the same for all radii and so all particles more or less reach the densest configuration at the same time, which is also more or less the same for all simulations of the previous set of parameters. Now, in the Plummer BG case, the free-fall times vary with radius and the point of densest configuration can vary in time for the different sets of initial particle distributions. Therefore, we see no clear oscillations in our results, which are mean values calculated from all simulations, but rather inflated error-bars.

The bottom-right panel shows the results for the Plummer BG potential starting in a cool state i.e. we get a strong compression. The trend of fast rising Λ values as seen in the corresponding uniform BG case is produced even faster now, reaching a high value earlier than 1 Myr and stabilizing at a value of MS of $\Lambda_{\rm final} = 2.83 \pm 0.68$ ($t_{\rm seg}$ = always).

In the lower half of this panel, we see that the cold initial conditions produce a similar collapse or contraction in all simulations resulting in small error-bars for R_h. The steeper potential of the Plummer BG helps to damp the oscillations rather quickly. It settles at about the same value as in the uniform, cold case, as predicted in previous studies (Smith et al. 2011, 2013).

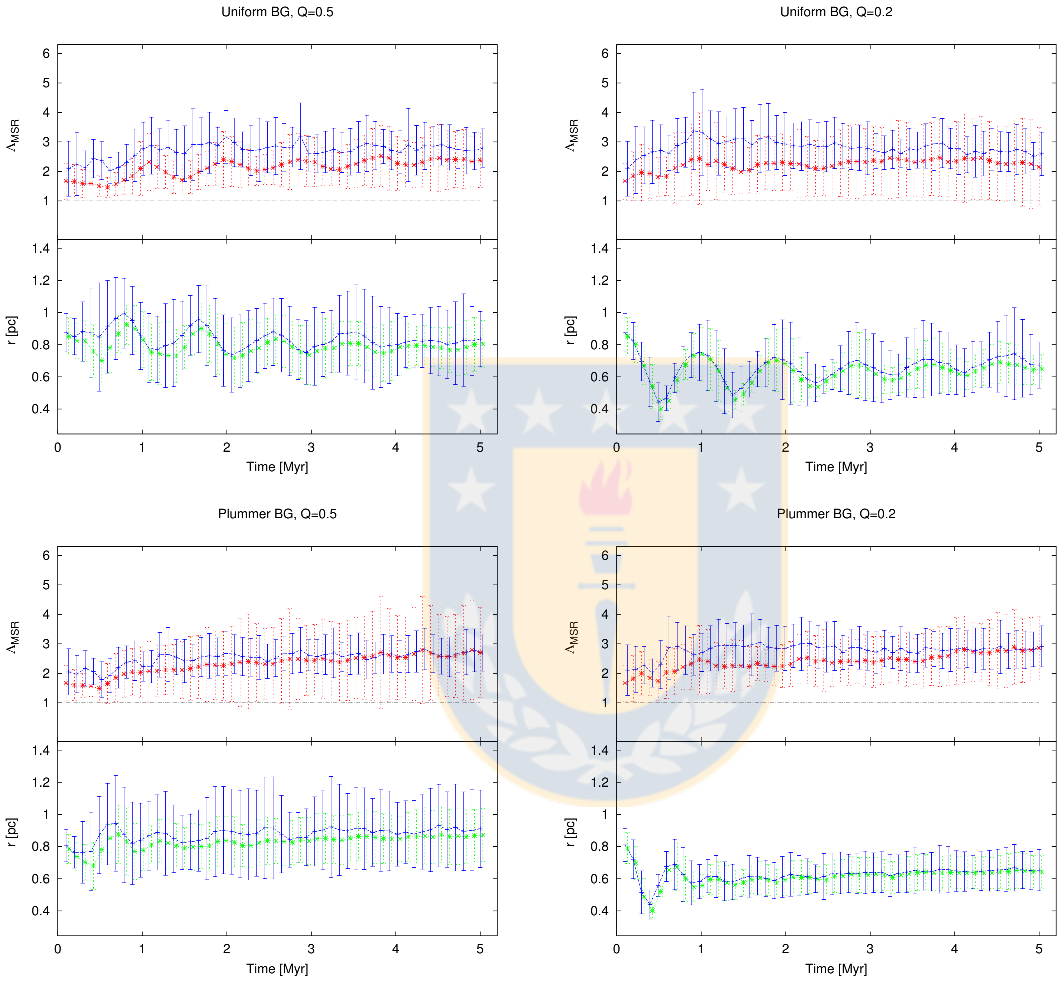

FIGURE 4.1: Results for NO-SEG, i.e. the masses are distributed randomly throughout the whole fractal. In contrary to Fig. 3.4 each datapoint is a mean value calculated from ten different random realisations. Top row panels show the results for a uniform background and the lower row panels for the Plummer background. Left panels are the simulations with Q_{init} = 0.5, i.e. starting in 'pseudo-virial equilibrium' and right panels show the simulations where velocities are reduced to obtain $Q_{init} = 0.2$. In each panel the top half shows the evolution of Λ_{MST} (red stars and dashed lines) and Λ_{rest} (blue plus signs and solid lines). In the lower halves of the panels we show the evolution of Rh (green dashed line) and r_8 (blue solid line). From this work.

4.1.2 SEG-IN

The sets of simulations (shown in Fig. 4.2) are designed to have a high value of MS initially, as we have forced the high mass stars to be in the central area. In all panels we see initial Λ values in the range between 5 and 6. Also both methods agree at the beginning perfectly as not a single high mass star is ejected yet. In all simulations we see a rapid decline of the MS values until they settle at roughly the same values as in the NO-SEG cases.

This is in contrary to any prediction of the dynamics of MS in which we should always see an increase. We explain this behaviour that due to the initial contraction of our stellar distributions, the central area gets stirred up and massive stars may end up further out then they initially were. Furthermore, the initial contraction or even collapse (cold simulations) compacts the low mass stars towards the potential centre. We see larger error-bars for the non-restricted values as high mass stars leave the central area.

The behaviour of R_h is similar to the NO-SEG cases explained above.

The top-left panel again shows the uniform BG-$\mathrm{Q_{init}} = 0.5$ case. The simulations reach a final value of $\Lambda_{\mathrm{final}} = 2.69 \pm 0.69$ with t_{seg} = always (in fact all panels show t_{seg} = always). The top-right panel shows the results for the uniform BG potential starting in a cool state. Here the final value is 2.56 ± 0.66. For the Plummer BG with $\mathrm{Q_{init}} = 0.5$ (bottom left panel) we get $\Lambda_{\mathrm{final}} = 2.89 \pm 0.82$, which is slightly higher than with the uniform BG. It seems that a steeper potential, even though not influencing the final value of R_h is able to retain the massive stars in the centre better than the uniform BG. Finally, in the bottom right (Plummer BG-$\mathrm{Q_{init}} = 0.2$) we get $\Lambda_{\mathrm{final}} = 2.79 \pm 0.68$.

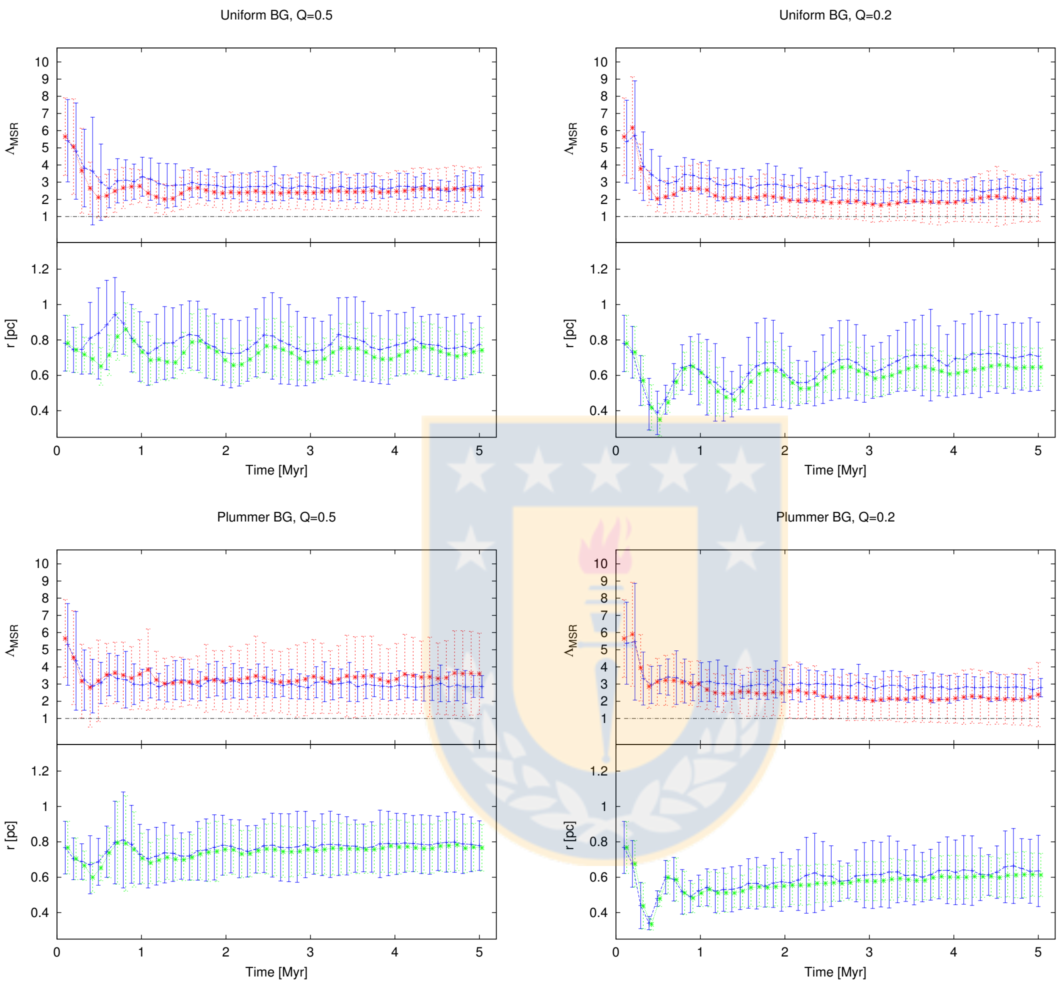

FIGURE 4.2: Results for SEG-IN, i.e. where all the massive stars are initially within the central 0.5 pc. In contrary to Fig. 3.4 each datapoint is a mean value calculated from ten different random realisations. Top row panels show the results for a uniform background and the lower row panels for the Plummer background. Left panels are the simulations with Q_{init} = 0.5, i.e. starting in 'pseudo-virial equilibrium' and right panels show the simulations where velocities are reduced to obtain Q_{init} = 0.2. In each panel the top half shows the evolution of Λ_{MST} (red stars and dashed lines) and Λ_{rest} (blue plus signs and solid lines). In the lower halves of the panels we show the evolution of Rh (green dashed line) and r_8 (blue solid line). From this work.

4.1.3 SEG-OUT

In this section we describe our results (shown in Fig. 4.3) obtained with rather unphysical initial conditions, i.e., we start with all high mass stars being formed in the outskirts of the stellar distribution. This is inverse MS and should be reflected by initial Λ values below unity. Still, as a mean value taken from many simulations we see a value close to unity, i.e. no segregation. It seems that the minimum spanning tree method delivers higher degrees of MS as there actually are. If this is the truth for all measurements or just a curiosity due to our fractal initial distributions needs to studied in a separate investigation.

In the pseudo-equilibrium cases (left panels), we see no fast evolution in MS but a slow increase with the uniform BG ($\Lambda_{\mathrm{final}} = 2.12 \pm 0.57$ and tseg = 3.5 Myr) or almost no evolution at all with the Plummer BG ($\Lambda_{\mathrm{final}} = 1.61 \pm 0.39$ and t_{seg} = never). This shows that the small contraction of our stellar distribution is not enough to ensure sufficient interactions between the high mass stars and the lower mass stars to drive them efficiently towards the centre. How realistic such initial conditions are, is debatable.

If we look at the cold cases (right panels), we see again a very fast evolution of MS. Here, it seems the initial collapse of the stellar distribution is enough to drag the high mass stars to the central area and then they stay there. We get for the uniform BG case a value of 2.70 ± 0.72 with a $t_{\mathrm{seg}} = 1.3$ Myr and for the Plummer BG case 2.14 ± 0.60 and $t_{\mathrm{seg}} = 3.8$ Myr.

The bottom halves of the panels show again the same evolution of Rh as seen in the other sets, but this time we note that the values for r8 are always larger than R_h for all initial conditions and throughout the simulation times. This means that in all simulations we never got 8 or more massive stars within the half-mass radius.

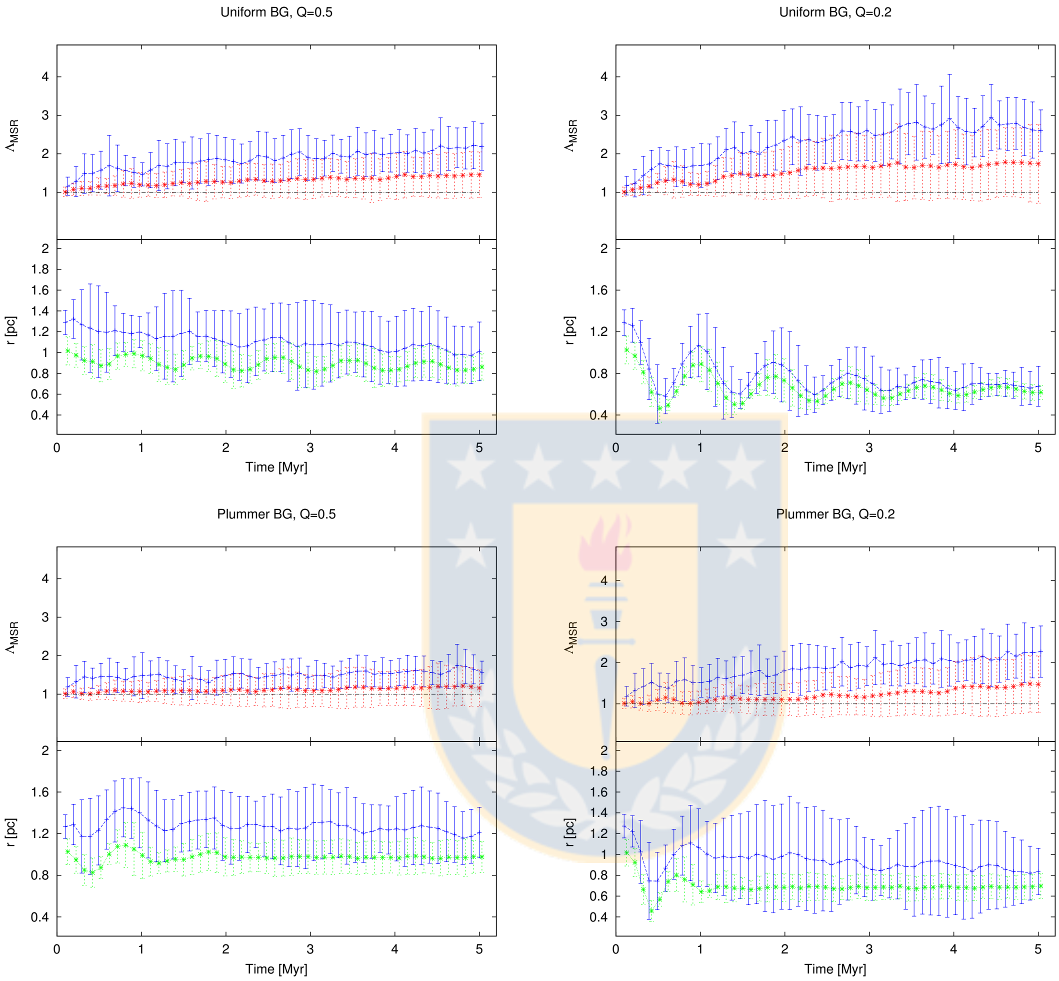

FIGURE 4.3: Results for SEG-OUT, i.e. where all the massive stars are initially outside the central 1.0 pc. In contrary to Fig. 3.4 each datapoint is a mean value calculated from ten different random realisations. Top row panels show the results for a uniform background and the lower row panels for the Plummer background. Left panels are the simulations with $Q_{\rm init}$ = 0.5, i.e. starting in 'pseudo-virial equilibrium' and right panels show the simulations where velocities are reduced to obtain $Q_{\rm init}$ = 0.2. In each panel the top half shows the evolution of $\Lambda_{\rm MST}$ (red stars and dashed lines) and $\Lambda_{\rm rest}$ (blue plus signs and solid lines). In the lower halves of the panels we show the evolution of Rh (green dashed line) and r_8 (blue solid line). From this work.

4.2 Summary & Discussion

A summary of the most important initial parameters and the associated results is given in Tab. 4.1.

In Fig. 4.4 we show the final configurations for the three example simulations shown in Fig. 3.2. In the left and central panel one clearly sees the effect of MS. In the right panel (SEG-OUT case) the results are debatable, but still an overdensity of massive stars can be detected in the centre. In fact this particular example has indeed a final value higher than two.

All sets of simulations (except the SEG-OUT cases) reach values of $\Lambda_{\text{rest}} \geq 2$ very fast (less than 1 Myr) or even show these values from the start.

This shows that it is possible to observe MS after very short times in the embedded phase for clusters which are not initially segregated, so the premise where MS has to be primordial (e.g. Bonnell & Davies 1998; Hillenbrand & Hartmann 1998; Raboud & Mermilliod 1998) is not strictly necessary. Parker et al. (2015) found that primordial MS is less common when in the process of star formation the influence of feed-back is taken into account. However, we cannot exclude primordial MS, which is supported by hydrodynamical simulations (e.g. Klessen 2001b; Bonnell et al. 2001; Bonnell & Bate 2006).

After gas-expulsion, the naked SC can inherit the level of MS from the embedded phase, which can be used as an initial condition for studies of later evolution (e.g. McMillan et al. 2007; Moeckel & Bonnell 2009b; Allison et al. 2009).

The global evolution, in the unlikely scenario SEGOUT, is slower due the location of the massive stars. The low gravitational potential of a Plummer BG in the outer parts joined with a weak compression ($Q_{\text{init}} = 0.5$) is not producing a significant level of MS. In comparison the flat uniform BG, which is stronger in the outer parts, is helping to drag most of the massive stars to the centre. For the cool initial state, the Plummer BG is helping the massive stars to reach locations with a deeper potential but not within a short time interval.

Allison et al. (2010) and Yu et al. (2011) performed similar N-body simulations but without any background potential for the gas distribution. When starting with initially virial (in reality pseudo-virial) conditions they obtain MS values around ~ 2. In their cold simulations they obtain MS values of about 6 (Allison et al. 2010) or even larger than 20 (Yu et al. 2011). While our MS values in the pseudo-virial case are somewhat higher they mainly agree within the errors. We believe the reason for the difference can be found in the use of the background potential which is helping to retain stars (in this case high mass stars) in the central cluster area, which otherwise would have been ejected or at least transported to larger radii. In the initially cold simulations, we see a strong collapse of all stars alike, transporting many low-mass stars to the central areas as well. This lowers our values of MS significantly and by using a background potential, we also keep more low-mass stars from being ejected.

We have to discuss the different values of the $\Lambda_{\rm MST}$ and $\Lambda_{\rm rest}$ parameters in our simulations. The use of $\Lambda_{\rm rest}$ produces more reliable results. The length of the error bars are smaller than using the unrestricted method, because stars which are escaping or always stay in the outskirts of the cluster are not taken into account. As a consequence the value of $\Lambda_{\rm MST}$ is almost always smaller.

As our results show, both methods produce initial values higher than one, when placing the high mass stars completely random inside our fractals. Per definition, this should give a value of one or at least close to one. The restricted method even shows values around 2, which translates into a significant level of MS. In later stages, when a significant amount of massive stars are located in the very centre of our simulations (see Fig. 4.4), we barely obtain a high value of MS with both methods. We suspect our fractal initial conditions together with the use of a background potential and the subsequent behaviour of our stellar distributions due to this initial conditions to be the culprit. Having a closer look at Fig. 3.2 helps to shed light onto this puzzle. We have a fractal distribution at the start of our simulation, i.e. there is no central density enhancement. The low mass stars have quite a lot of choices for the MST, some of them could be even larger than the result for the massive stars. In consequence this leads to a value larger than one (left panel of Fig. 3.2).

Running our simulations leads to a contraction of the distribution in the pseudo-virialised case or to a collapse in the cold simulations, resulting in a more spherical symmetric and far more denser distribution of the stars. This process is very fast (less than 1 Myr) and very effective in depositing almost all (NO-SEG and SEG-IN cases; see left and middle panel in Fig. 4.4) high mass stars in the central area. Even in the SEG-OUT case we do see many high mass stars in the centre. Per definition this should be a highly mass-segregated configuration. But not only the high mass stars are now centrally concentrated, the low mass stars are also more centrally concentrated than at the beginning, leading to a high probability for short MSTs, which enter the calculation of $\Lambda_{\rm MST}$ and even more so for $\Lambda_{\rm rest}$. This will lead to lower values of MS, and explains why in the SEG-IN case we see a sharp initial drop of the Λ values, due to all the low-mass stars settling into a more concentrated distribution

In our models, no stellar evolution was included which is not realistic, but as we reach significant levels of MS in less than one Myr, i.e. a time in which even the most massive stars of our simulations do not evolve, we are confident that this short-fall of our simulations would not alter the final results. The influence of stellar evolution on our results will be subject of a different investigation in the near future.

TABLE 4.1: Summary of results. The first, second and third column are giving information of the initial conditions: type of BG potential, mass distribution and virial ratio respectively. The fourth and fifth column show the final values for$\Lambda_{\rm MSR}$ and $\Lambda_{\rm rest}$ respectively. The values are calculated by taking an average value of all measurements between 4 and 5 Myr. The sixth column gives $t_{\rm seg}$ i.e. the information when ($t_{\rm seg}$) $\Lambda_{\rm rest}$ stays larger than 2, i.e., a significant level of MS is detected. The last two columns are the final values for r_8 and R_h respectively. Again we calculate them as averages from all measurements between 4 and 5 Myr. From this work.

BG Potential	Inital Mass distribution	Initial Q	Final $\Lambda_{\rm MSR}$	Final $\Lambda_{\rm rest}$	$\Lambda_{\rm rest} \geq 2$ $t_{\rm seg}$ [Myr]	Final r_8 [pc]	Final R_h [pc]
Uniform	NO-SEG	0.5	2.350.94	2.79 ± 0.77	always	0.82 ± 0.20	0.79 ± 0.14
Uniform	NO-SEG	0.2	2.32 ± 1.38	2.66 ± 0.73	always	0.69 ± 0.19	0.65 ± 0.11
Plummer	NO-SEG	0.5	2.65 ± 1.53	2.68 ± 0.66	0.7	0.90 ± 0.24	0.86 ± 0.17
Plummer	NO-SEG	0.2	2.78 ± 1.13	2.83 ± 0.68	always	0.65 ± 0.12	0.64 ± 0.10
Uniform	SEG-IN	0.5	2.58 ± 1.24	2.69 ± 0.69	always	0.77 ± 0.17	0.73 ± 0.13
Uniform	SEG-IN	0.2	2.03 ± 1.39	2.56 ± 0.66	always	0.71 ± 0.21	0.64 ± 0.11
Plummer	SEG-IN	0.5	3.49 ± 2.28	2.89 ± 0.82	always	0.79 ± 0.16	0.77 ± 0.14
Plummer	SEG-IN	0.2	2.20 ± 1.55	2.79 ± 0.68	always	0.64 ± 0.18	0.61 ± 0.12
Uniform	SEG-OUT	0.5	1.43 ± 0.58	2.12 ± 0.57	3.5	1.02 ± 0.32	0.87 ± 0.14
Uniform	SEG-OUT	0.2	1.72 ± 0.91	2.70 ± 0.72	1.3	0.68 ± 0.16	0.63 ± 0.07
Plummer	SEG-OUT	0.5	1.18 ± 0.50	1.61 ± 0.39	never	1.22 ± 0.31	0.97 ± 0.16
Plummer	SEG-OUT	0.2	1.43 ± 0.69	2.14 ± 0.60	3.8	0.86 ± 0.38	0.69 ± 0.12

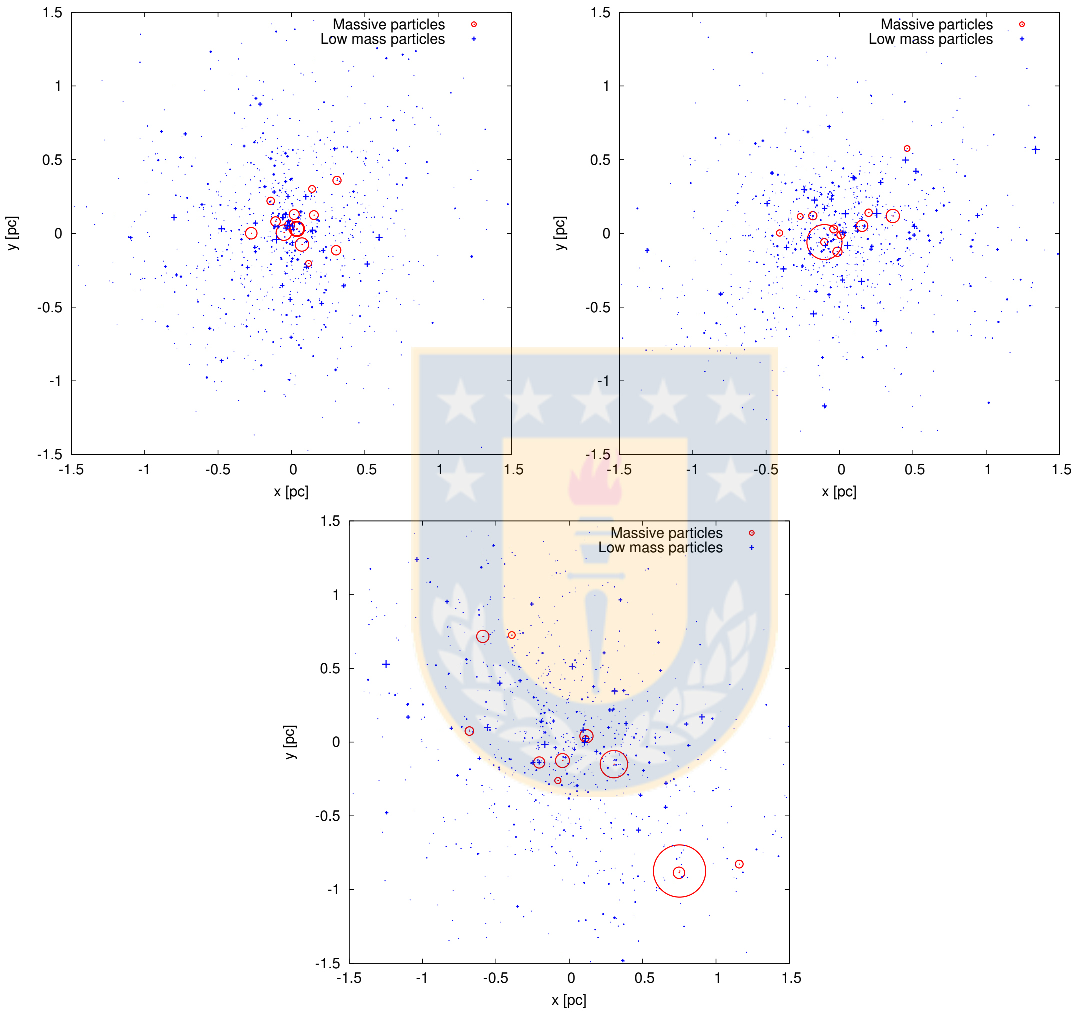

FIGURE 4.4: Examples of the final state for the three different initial distribution of massive stars showed in Fig. 3.2. Left panel: Final state of fractal which start with NO-SEG. Central panel: final state of fractal which start with SEG-IN. Right panel: final state of fractal which start with SEG-OUT. From this work.

Chapter 5

Conclusions: Mass segregation

5.1 MS Conclusions

We have presented simulations of the early evolution of initially cool or pseudo-virial, fractal embedded star clusters. The clusters start with three different initial levels of MS namely NO-SEG, SEG-IN and SEG-OUT. We follow the level of MS using the MST method using all the stars ($\Lambda_{\rm MSR}$) and the same method restricted to R_h or r_8 ($\Lambda_{\rm MSR} - R$).

We conclude that in all cases, due to the contraction or collapse (pseudo-virial or cold conditions, respectively) we get significant MS within a short time-span of less than 1 Myr. Or, if one refuses to call our initial conditions a star cluster, then our results imply that as soon as the star cluster is formed it is automatically mass-segregated from the start.

On the other hand our results show, that the distribution of stars inside the cluster have lost any information of their initial birth place and so the question if stars are born mass-segregated cannot be answered by looking at a mass-segregated cluster. The only set of simulations which retained at least part of this initial information is the highly unlikely SEG-OUT case, i.e. the most massive stars are born in the outer parts of the star forming region. Here, some massive stars on rather circular orbits do not fully take part in the initial contraction phase and therefore do not get deposited into the central area.

To answer the question if the MS is independent of the properties of the gas in embedded young star clusters, we find a similar degree of MS ($\Lambda_{\rm MSR}$) independent of the conditions of the gas we use.

We conclude that any combination of initial virial ratio, BG potential, and initial mass distribution can lead to almost the same levels of MS with $\Lambda_{\mathrm{MSR}} \approx 2.6 \pm 0.7$. The only exception is the unlikely scenario SEG-OUT together with the pseudo-virial velocities, where this parameter shows somewhat lower values.

The dependence on the stochastic initial conditions of the fractal distributions produces in a few cases results far away from the average values reported in this study and we cannot exclude the possibility that these cases can be observed.

Chapter 6

Survival of Embedded Star Clusters

6.1 Aim

By means of N-body simulations, we study the evolution of young SCs after the expulsion of their gas. Continuing with previous work we study how the inclusion of an IMF affects the final fraction of stars which remain bound after gas expulsion, i.e., the infant mortality process.

6.2 Previous work

One parameter to characterise embedded SCs is the star formation efficiency (SFE). The SFE is the comparison of the mass of stars ($M_{\rm stars}$) with the total mass of the cluster i.e. including the mass of gas ($M_{\rm gas}$) as follows:

$$\mathrm{SFE} = \frac{M_{\rm stars}}{M_{\rm stars} + M_{\rm gas}} \tag{6.1}$$

from the equation is clear that when a larger quantity of $M_{\rm gas}$ is included compared to $M_{\rm stars}$, a lower value of the SFE results.

Using this parameter many works have addressed the issue of infant mortality purely theoretically (Tutukov, 1978; Hills, 1980; Lada et al., 1984; Goodwin, 1997; Kroupa et al., 1999; Adams, 2000; Geyer & Burkert, 2001; Kroupa, 2001; Boily & Kroupa, 2003; Fellhauer & Kroupa, 2005; Bastian & Goodwin, 2006; Baumgardt & Kroupa, 2007) and by means of N-body simulations (Tutukov, 1978; Hills, 1980; Lada et al., 1984; Goodwin, 1997). Hills (1980), using the virial theorem, argued that for an SFE > 0.5 the cluster results in completely destroyed if the gas is removed instantaneously. N-body modelling

(Lada et al. (1984); Geyer & Burkert (2001); Boily & Kroupa (2003)) confirmed the idea of Hill. Lada et al. (1984) found a bound SC with SFE = 0.4 and Geyer & Burkert (2001) indicated that the critical SFE is below 0.35, supported by Kroupa (2001) computing the evolution of Orion nebula-like clusters.

Baumgardt & Kroupa (2007) by means of several N-body simulations studied how the star formation efficiency (SFE) can affect the process. Different ways to eliminate the gas were taken into account their work, quantified by the duration of the gas removal ($\tau_{\rm ge}$). The first regimen of gas expulsion corresponds to an explosive event, where $\tau_{\rm ge} << \tau_{\rm cross}$, while the second is adiabatic where $\tau_{\rm ge} >> \tau_{\rm cross}$. To quantify the survival of a cluster the bound mass ($M_{\rm bound}$) after the expulsion of gas is compared with the initial mass with the equation:

$$\mathrm{f_b} = \frac{M_{\rm bound}}{M_{\rm stars}} \tag{6.2}$$

Baumgardt & Kroupa (2007) used spherical distributions to emulate the initial state of a star cluster and the gas. They covered values of SFE in the range of 0.05-0.80. Baumgardt & Kroupa (2007) removed the gas potential with different $\tau_{\rm ge}$. In this sense a value of $\tau_{\rm ge} = 0$ means an instantaneous gas expulsion. In this case the cluster cannot react to this change in the global state becoming super-virial ($Q >> 1$), reaching velocities higher than $v_{\rm esc}$. The cluster cannot prevent its members from spreading into the field. In an adiabatic regime, $\tau_{\rm ge} > 0$, the cluster can adapt to the change and can retain more members after the total removal of the gas. They measured the $\mathrm{f_b}$ for different values of SFE to find the dependency on $\tau_{\rm ge}$.

Fig. 6.1 shows a comparison of results from different work comparing the SFE against $\mathrm{f_b}$. The results show a general trend where for low SFE the bound fraction is also low or zero. It is possible to find surviving clusters for low SFE when the gas was expelled slowly. For instant gas expulsion (worst scenario) the low limit is around of SFE ~ 0.3.

Smith et al. (2011) added a new initial condition to the simulations to produce more realistic conditions. They changed the initial spherical distribution used by Baumgardt & Kroupa (2007) to a substructured distribution, as is commonly observed for young embedded SCs (see Sec. 1.1.2).

They used three different values for SFE. The covered the range between 0.2 and 0.3, where all previous studies did not find surviving clusters. They also use SFE = 0.4 where the previous results found survival of clusters.

Smith et al. (2011) found surviving clusters for SFE = 0.4 as the previous work and, also found surviving clusters for SFE = 0.3 and, SFE = 0.2.

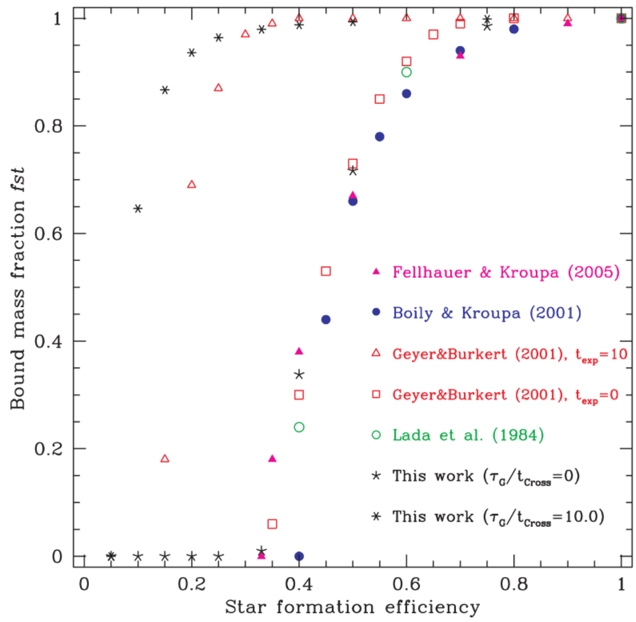

FIGURE 6.1: Comparison f_b in function of SFE from different works using instantaneously gas expulsion or an slow one. Figure taken from Baumgardt & Kroupa (2007)

Fig. 6.2 shows the results obtained by Smith et al. (2011) compared with Baumgardt & Kroupa (2007) where is possible to observe surviving cluster for the three different SFEs.

They concluded that SFE which is a global quantity is not describing very well if a cluster can survive or not after emerging from its gas.

For a better description of the final f_b, Smith et al. (2011) introduced a new parameter called Local Stellar Fraction (LSF) which compares the mass of stars and the total mass (counting gas) as the SFE but now restricted to the R_h as follow:

$$\mathrm{LSF} = \frac{M_{\mathrm{stars}}(r < R_h)}{M_{\mathrm{stars}}(r < R_h) + M_{\mathrm{gas}}(r < R_h)} \tag{6.3}$$

This parameter can describe better than the SFE the actual state of the cluster. The SFE of the simulations does not change while the stars are constantly moving and trying to re-arrange themselves into a more spherical and denser configuration. As the stars are moving, the R_h in constantly changing with time, making the LSF a time-varying quantity, which is better suited to describe these dynamically changing systems.

Fig. 6.3 shows the same simulations shown in 6.2 but now as a dependence of the LSF at the moment of the gas expulsion. A trend can be observed where for a low LSF a low f_b is obtained. For higher LSF is possible to observe also higher f_b. A significant spread anyway is observed and, more observable for low LSF (~ 0.2).

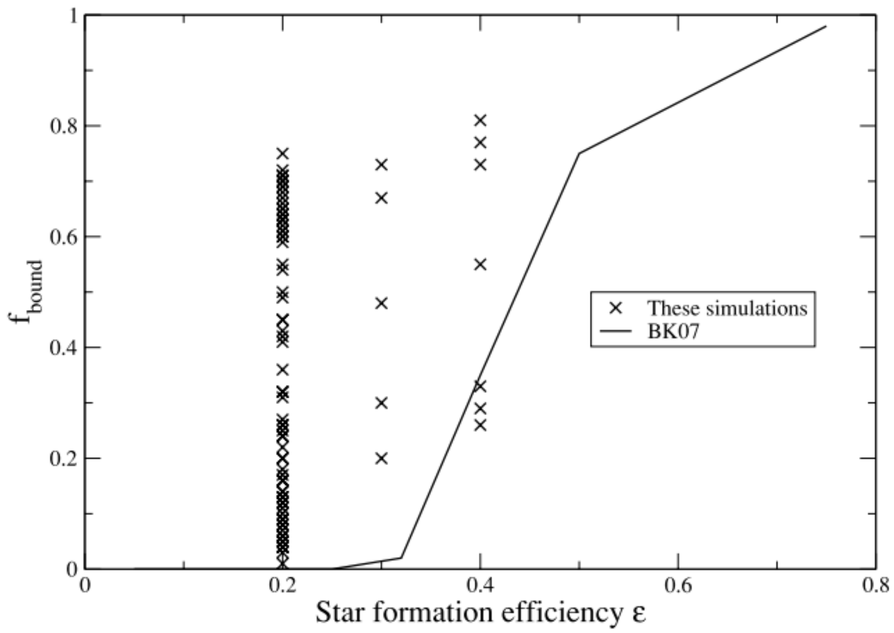

FIGURE 6.2: SFE against f_b. The solid line represents the results from Baumgardt & Kroupa (2007) and stars are the results from Smith et al. (2011). From Smith et al. (2011)

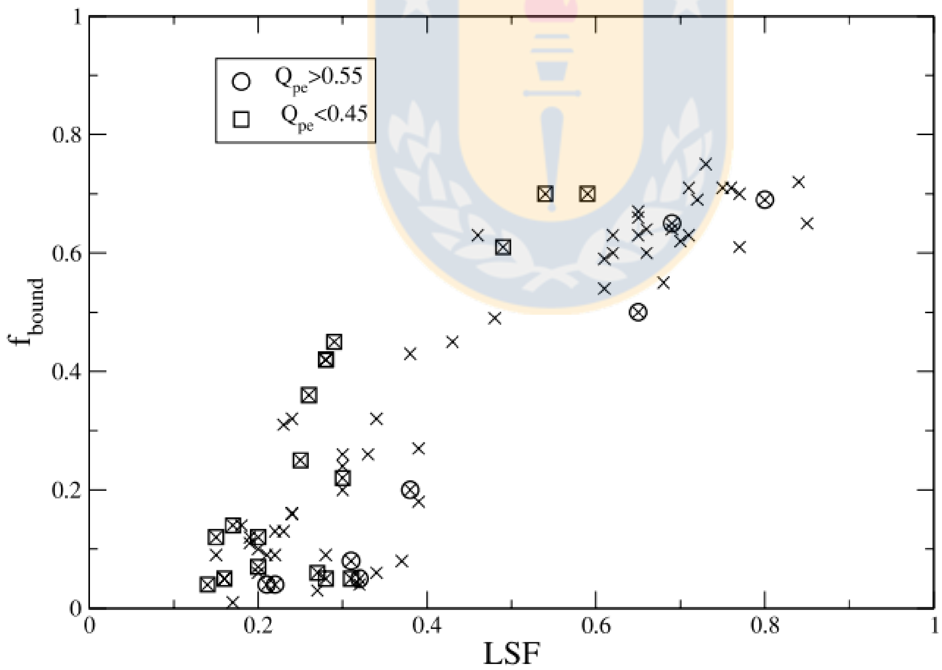

FIGURE 6.3: Results of LSF against f_b. From Smith et al. (2011)

Farias et al. (2015), continuing with the previous work and looking for a better description of f_b, focused only in a SFE = 0.2. They added Q_f, the virial ratio of the stars at the time of gas-expulsion as a secondary parameter, to better describe the bound fraction and as a explanation foe the scatter in the results of Smith et al. (2011). In Fig. 6.4 is showed the results obtained by Farias et al. (2015), where a clearer trend is observed if the results are sorted by their different Q_f. The colours represent the shape of the background gas, a Plummer sphere (blue) and a uniform sphere (red). The filled circles are simulations with $Q_{init} = 0.5$ and open circles are distributions with $Q_{init} = 0.0$. As a general trend we observe that simulations starting which $Q_{init} = 0.0$ are surviving better as they produce higher values of LSF at the time of gas-expulsion.

At the moment just before the gas expulsion in the work of Farias et al. (2015) the SCs showed Maxwellian distributions for the velocities of the stars. The solid line in Fig. 6.4 represents the cumulative distribution function as follow:

$$f_b = \mathrm{erf}\left(\sqrt{\frac{3}{2}\frac{\mathrm{LSF}}{Q_f}}\right) - \sqrt{\frac{6}{\pi}\frac{\mathrm{LSF}}{Q_f}}\exp\left(-\frac{3}{2}\frac{\mathrm{LSF}}{Q_f}\right) \tag{6.4}$$

which can predict in a good way the f_b only knowing the LSF and Q_f at the moment where the gas is expelled.

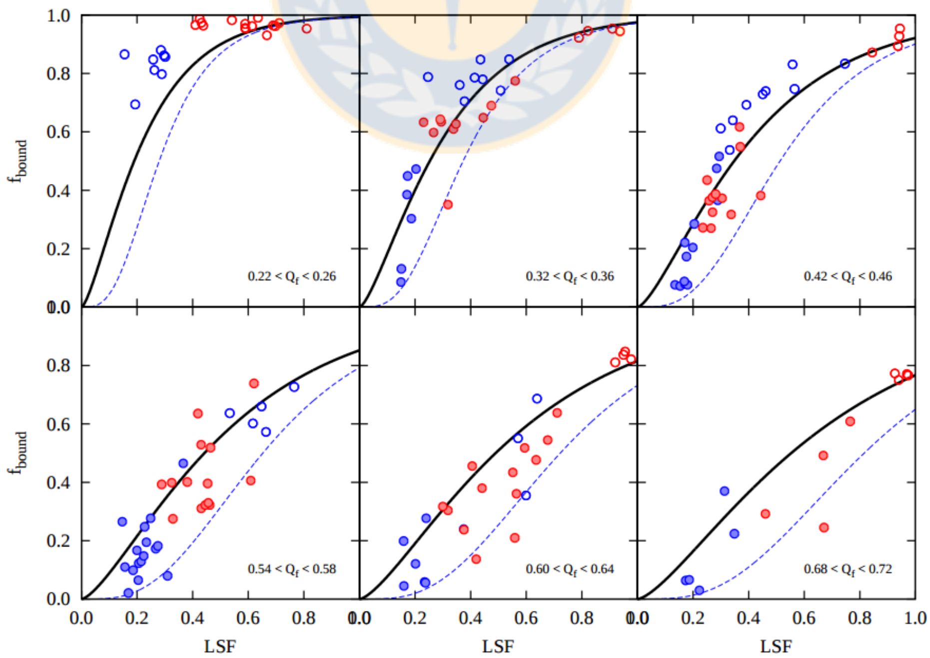

FIGURE 6.4: LSF against f_b split by different ranges of Q. From Farias et al. (2015)

6.3 Method

Continuing with the work by Farias et al. (2015) we added a new parameter, an IMF. All the studies described before have been performed using equal-mass particles to avoid the effects of MS and strong two-body interaction.

- We emulate the initial state of SCs with 10 substructured distributions. To generate these kind of distribution we used the method of Goodwin & Whitworth (2004) (see Sec. 2.2) with a value of D=1.6 and a total radius $R = 1.5$ pc.
- We assigned different masses according to a modified Kroupa IMF (2002) (see Eq. 3.1). We use 8 random IMF samples with ~ 500 $M_{\odot}$ and ~ 1000 particles. The samples that we use are shown in Fig. 6.5 and described in Tab. 6.1.
- To locate the massive stars in the distribution at positions we use the distribution NO-SEG and SEG-IN (see Sec. 3.3)
- The SCs are embedded in two different BG potential. A cored potential is emulated by a Plummer sphere and a flat potential by a uniform sphere with SFE = 0.2 (Lada, 1999; Lada & Lada, 2003; Clark & Bonnell, 2004).
- To emulate the gas expulsion we instantaneously remove the BG potential, producing the worst case scenario in terms of abrupt gas expulsion.
- The gas is removed at four different times in the evolution of the oscillation of Q defining a "virial" time-scale. One complete oscillation of Q is called one virial-time (vt). Fig. 6.6 shows an example of the evolution of Q. The gas is expelled independent of $Q_{\rm init}$ in the first crest (vt = 0.25), then at Q = 0.5 (vt = 0.50), at the first valley (vt = 0.75) and the last again at Q = 0.5 (vt = 1.0).
- At the instant of gas expulsion, we measure the value of the parameters LSF and $Q_{\rm f}$.
- After the gas expulsion, we evolve the clusters for 9 Myr without BG potential and measure the $f_{\rm b}$.
- We use the prediction of Farias et al. (2015) for equal mass-particles (see Eq. 6.2) to compare with our results.

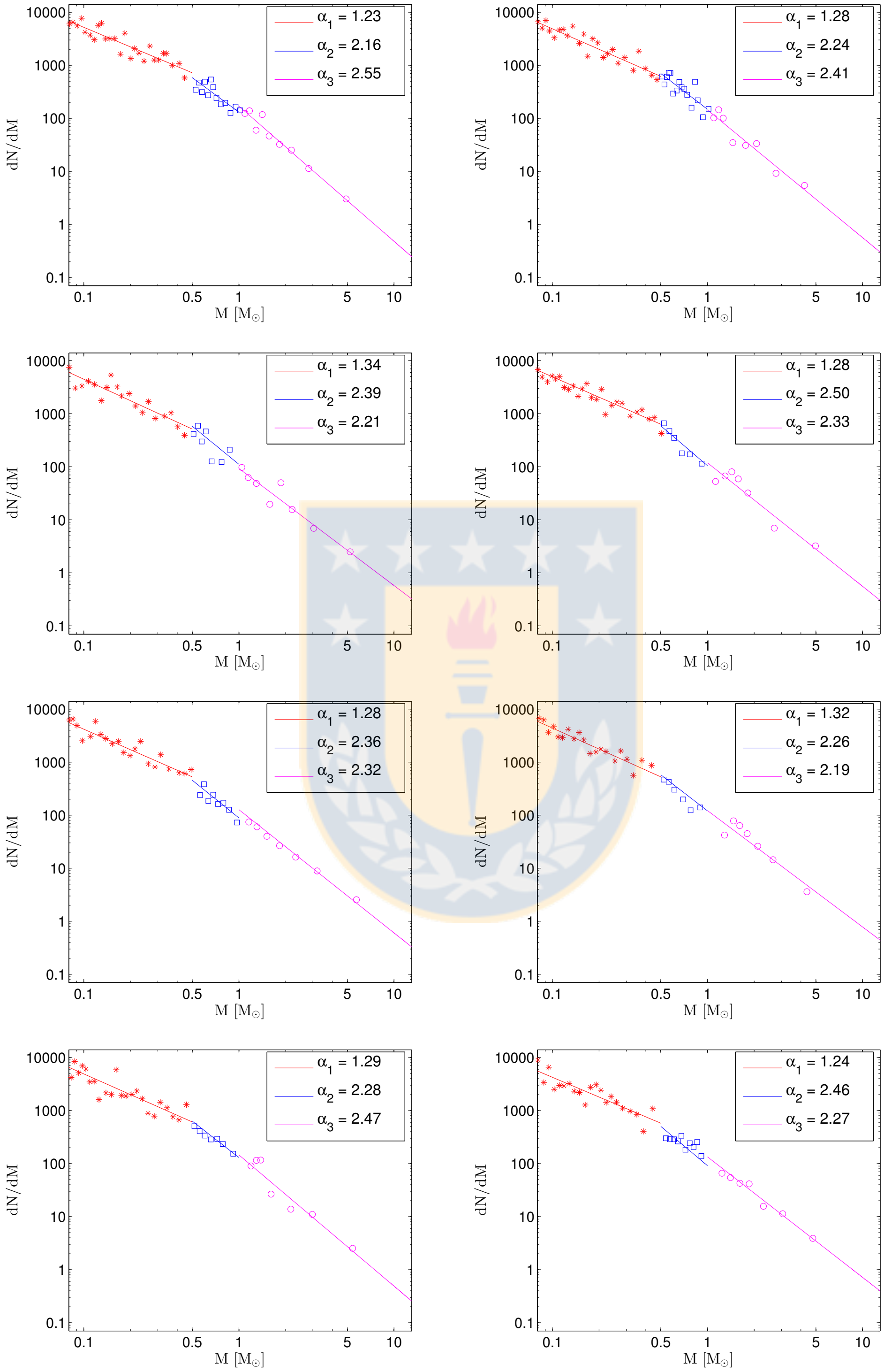

FIGURE 6.5: Samples of IMF used for the simulations in this work. The different colours are to represent the regions of the masses. From this work.

TABLE 6.1: Summary of properties of IMF samples showed in Fig. 6.5. From this work.

IMF sample row	Total Mass [$M_\odot$]	Number of particles (N_p)	N_p range 1	N_p range 2	N_p range 3	N_p $M \geq 4\ M_\odot$	N_p $M \geq 10$ [$M_\odot$]	Maximum Mass [$M_\odot$]	Average Mass [$M_\odot$]
(1)	500.23	1013	788	124	101	9	2	32.36	0.49
(2)	500.36	960	709	155	96	16	2	15.45	0.52
(3)	522.98	800	607	120	73	14	6	48.64	0.65
(4)	501.21	927	721	126	80	13	3	37.51	0.54
(5)	500.06	789	610	88	91	18	9	19.25	0.63
(6)	516.48	839	620	129	90	13	5	29.91	0.62
(7)	500.06	936	705	140	91	14	5	23.12	0.53
(8)	500.24	857	644	122	91	15	3	30.14	0.58

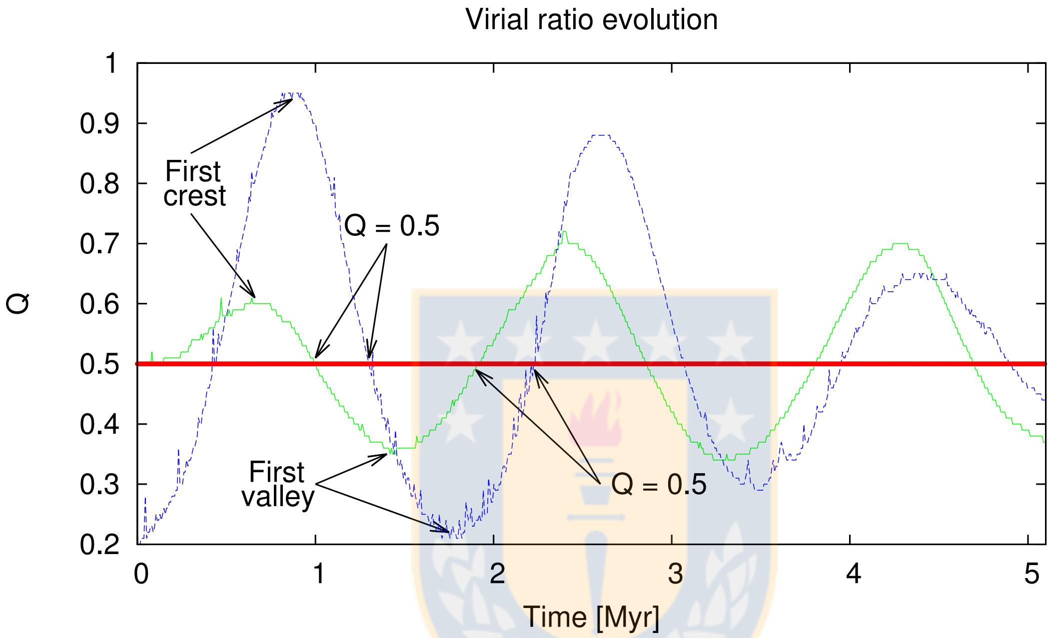

FIGURE 6.6: An example of the evolution of the virial-ratio for fractal distributions. The green solid line shows the oscillations for one fractal starting in virial equilibrium (Q = 0.5) and the blue dashed line shows the changes for the same fractal now starting in a cool state (Q = 0.2). Horizontal line denotes the virial equilibrium value of Q = 0.5. The arrows show the four points of gas expulsion. From this work.

6.4 Set of Simulations

We perform, in total, 2560 N-body simulations using the direct N-body integrator code NBODY6 with around 1000 different mass particles with sub-virial, virial and clumpy initials conditions embedded in two different BG potentials.

We use a total of 10 different fractal distributions. To these fractals we assigne 8 different IMF samples, two different $Q_{\rm init}$ (cold and pseudo-equilibrium), embedded in two BG potential and expelling the gas at the four points previously described, producing the NO-SEG sample. The same sample was re-arranged with the restriction SEG-IN.

The complete sample of simulations is shown in Tab. 6.2.

TABLE 6.2: Summary of initial conditions of simulations used in this work. From this work.

Initial Distribution	IMF sample	Q_{init}	BG Potential	Fractal row	Virial Time
NO-SEG SEG-IN	(1-2-3-4-5-6-7-8)	0.5	Plummer	(1)	0.25-0.50-0.75-1.0
NO-SEG SEG-IN	(1-2-3-4-5-6-7-8)	0.5	Uniform	(1)	0.25-0.50-0.75-1.0
NO-SEG SEG-IN	(1-2-3-4-5-6-7-8)	0.2	Plummer	(1)	0.25-0.50-0.75-1.0
NO-SEG SEG-IN	(1-2-3-4-5-6-7-8)	0.2	Uniform	(1)	0.25-0.50-0.75-1.0
NO-SEG SEG-IN	(1-2-3-4-5-6-7-8)	0.5	Plummer	(2)	0.25-0.50-0.75-1.0
NO-SEG SEG-IN	(1-2-3-4-5-6-7-8)	0.5	Uniform	(2)	0.25-0.50-0.75-1.0
NO-SEG SEG-IN	(1-2-3-4-5-6-7-8)	0.2	Plummer	(2)	0.25-0.50-0.75-1.0
NO-SEG SEG-IN	(1-2-3-4-5-6-7-8)	0.2	Uniform	(2)	0.25-0.50-0.75-1.0
NO-SEG SEG-IN	(1-2-3-4-5-6-7-8)	0.5	Plummer	(3)	0.25-0.50-0.75-1.0
NO-SEG SEG-IN	(1-2-3-4-5-6-7-8)	0.5	Uniform	(3)	0.25-0.50-0.75-1.0
NO-SEG SEG-IN	(1-2-3-4-5-6-7-8)	0.2	Plummer	(3)	0.25-0.50-0.75-1.0
NO-SEG SEG-IN	(1-2-3-4-5-6-7-8)	0.2	Uniform	(3)	0.25-0.50-0.75-1.0
NO-SEG SEG-IN	(1-2-3-4-5-6-7-8)	0.5	Plummer	(4)	0.25-0.50-0.75-1.0
NO-SEG SEG-IN	(1-2-3-4-5-6-7-8)	0.5	Uniform	(4)	0.25-0.50-0.75-1.0
NO-SEG SEG-IN	(1-2-3-4-5-6-7-8)	0.2	Plummer	(4)	0.25-0.50-0.75-1.0
NO-SEG SEG-IN	(1-2-3-4-5-6-7-8)	0.2	Uniform	(4)	0.25-0.50-0.75-1.0
NO-SEG SEG-IN	(1-2-3-4-5-6-7-8)	0.5	Plummer	(5)	0.25-0.50-0.75-1.0
NO-SEG SEG-IN	(1-2-3-4-5-6-7-8)	0.5	Uniform	(5)	0.25-0.50-0.75-1.0
NO-SEG SEG-IN	(1-2-3-4-5-6-7-8)	0.2	Plummer	(5)	0.25-0.50-0.75-1.0
NO-SEG SEG-IN	(1-2-3-4-5-6-7-8)	0.2	Uniform	(5)	0.25-0.50-0.75-1.0
NO-SEG SEG-IN	(1-2-3-4-5-6-7-8)	0.5	Plummer	(6)	0.25-0.50-0.75-1.0
NO-SEG SEG-IN	(1-2-3-4-5-6-7-8)	0.5	Uniform	(6)	0.25-0.50-0.75-1.0
NO-SEG SEG-IN	(1-2-3-4-5-6-7-8)	0.2	Plummer	(6)	0.25-0.50-0.75-1.0
NO-SEG SEG-IN	(1-2-3-4-5-6-7-8)	0.2	Uniform	(6)	0.25-0.50-0.75-1.0
NO-SEG SEG-IN	(1-2-3-4-5-6-7-8)	0.5	Plummer	(7)	0.25-0.50-0.75-1.0
NO-SEG SEG-IN	(1-2-3-4-5-6-7-8)	0.5	Uniform	(7)	0.25-0.50-0.75-1.0
NO-SEG SEG-IN	(1-2-3-4-5-6-7-8)	0.2	Plummer	(7)	0.25-0.50-0.75-1.0
NO-SEG SEG-IN	(1-2-3-4-5-6-7-8)	0.2	Uniform	(7)	0.25-0.50-0.75-1.0
NO-SEG SEG-IN	(1-2-3-4-5-6-7-8)	0.5	Plummer	(8)	0.25-0.50-0.75-1.0
NO-SEG SEG-IN	(1-2-3-4-5-6-7-8)	0.5	Uniform	(8)	0.25-0.50-0.75-1.0
NO-SEG SEG-IN	(1-2-3-4-5-6-7-8)	0.2	Plummer	(8)	0.25-0.50-0.75-1.0
NO-SEG SEG-IN	(1-2-3-4-5-6-7-8)	0.2	Uniform	(8)	0.25-0.50-0.75-1.0
NO-SEG SEG-IN	(1-2-3-4-5-6-7-8)	0.5	Plummer	(9)	0.25-0.50-0.75-1.0
NO-SEG SEG-IN	(1-2-3-4-5-6-7-8)	0.5	Uniform	(9)	0.25-0.50-0.75-1.0
NO-SEG SEG-IN	(1-2-3-4-5-6-7-8)	0.2	Plummer	(9)	0.25-0.50-0.75-1.0
NO-SEG SEG-IN	(1-2-3-4-5-6-7-8)	0.2	Uniform	(9)	0.25-0.50-0.75-1.0
NO-SEG SEG-IN	(1-2-3-4-5-6-7-8)	0.5	Plummer	(10)	0.25-0.50-0.75-1.0
NO-SEG SEG-IN	(1-2-3-4-5-6-7-8)	0.5	Uniform	(10)	0.25-0.50-0.75-1.0
NO-SEG SEG-IN	(1-2-3-4-5-6-7-8)	0.2	Plummer	(10)	0.25-0.50-0.75-1.0
NO-SEG SEG-IN	(1-2-3-4-5-6-7-8)	0.2	Uniform	(10)	0.25-0.50-0.75-1.0

Chapter 7

Results and Discussion Survival of Embedded Star Clusters

7.1 Survival Results

To compare directly with the results of Farias et al. (2015) (see 6.2), we reproduce their figures splitting the results into six interval of Q_f.

7.1.1 LSF vs f_b after 9 Myr, embedded in an uniform BG

Fig. 7.1 shows the results of the simulations with a uniform BG after evolving without gas for 9 Myr. For each panel, 160 simulations were analysed for each mass distribution. The averages of f_b and 1σ errors were calculated for different ranges of LSF and Q_f. The top panel shows the results for simulations with $Q_{init} = 0.5$ and the bottom panel for simulations with $Q_{init} = 0.2$, both under the effect of a uniform BG. Blue crosses are the results for NO-SEG cases, red filled circles are the results for SEG-IN cases, while the green dashed line is the prediction of Farias et al. (2015) (see eq 6.2).

In some boxes of our figures no results are shown, because none of our simulations showed these particular ranges of Q_f values.

In the top panel of Fig. 7.1 we see clearly that the prediction of Farias et al. (2015) (in the following called the prediction) is above the results obtained in this study.

In the bottom panel, as before, the prediction overestimates f_b in most cases. We can note better agreement for low LSFs (<0.3) and, then the discrepancy becomes larger.

The results for high LSFs do not show a strong dependency of the LSF, with practically the same f_b.

The average of f_b is practically the same, independent of the initial mass distribution or match within the error-bars.

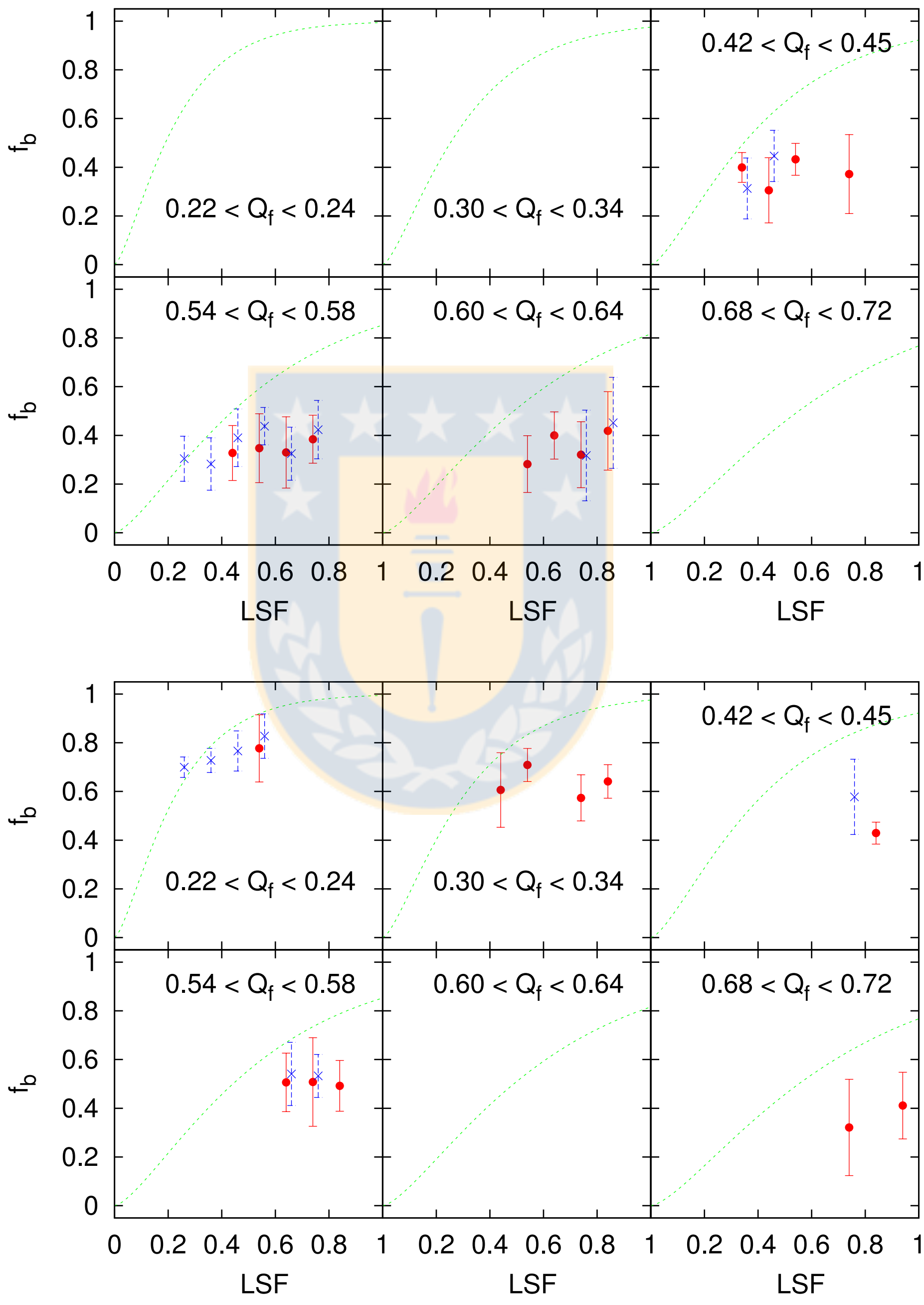

FIGURE 7.1: Both panels show results for simulations with uniform BG after 9 Myr evolving without gas. Top and bottom panels with $Q_{init} = 0.5$ and $Q_{init} = 0.2$ respectively. All the boxes show f_b as a function of LSF, divided in six intervals of Q_f as Farias et al. (2015). Our results are denoted by red circles for SEG-IN and blue crosses for NO-SEG. The green solid line is the prediction of Farias et al. (2015). From this work.

7.1.2 LSF vs f_b after 9 Myr, embedded in a Plummer BG

Fig. 7.2 shows the results of the simulations starting with a Plummer BG after evolving without gas for 9 Myr. For each panel, 160 simulations were analysed for each mass distribution. The averages of f_b and 1σ errors are calculated for different ranges of LSF and Q_f. The top panel shows the results for simulations with $Q_{init} = 0.5$ and the bottom panel for simulations with $Q_{init} = 0.2$, both under the effect of a uniform BG. Blue crosses are the results for NO-SEG cases, red filled circles are the results for SEG-IN cases, while the green dashed line is the prediction of Farias et al. (2015) (see eq. 6.2).

In the top panel of Fig. 7.2, as before, most of the results are below the curve.

The prediction also shows here a better agreement for low LSFs and, an increasing of the discrepancy as the LSF becomes larger.

The f_b is practically independent of the initial mass distribution as we observed previously.

In the bottom panel, we note in the second box that the prediction is underestimating f_b, but for the rest of results with high LSFs (>0.3), the previous trend is reproduced with all the results below the prediction.

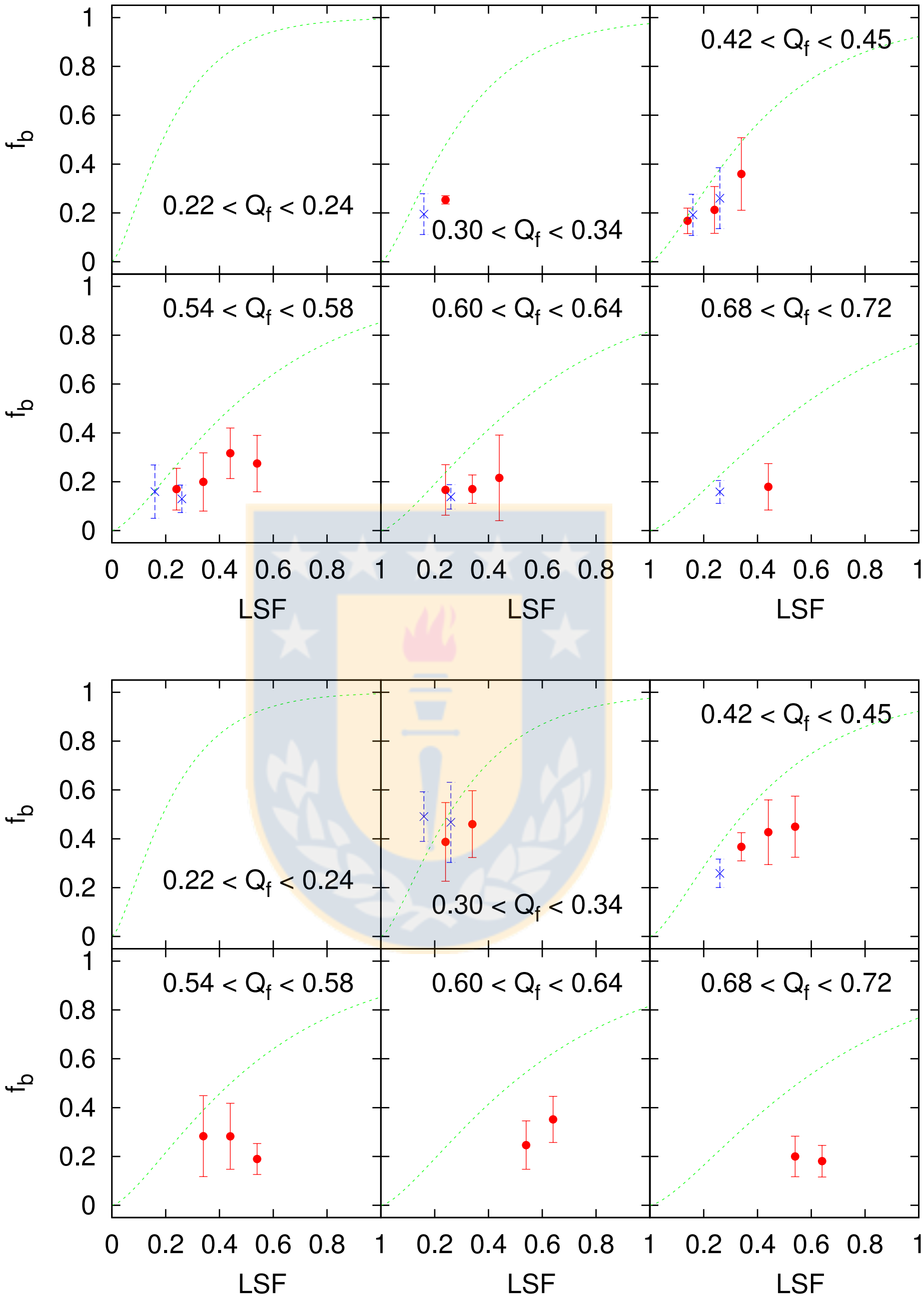

FIGURE 7.2: Both panels show results for simulations with Plummer BG after 9 Myr evolving without gas. Top and bottom panels with $Q_{init} = 0.5$ and $Q_{init} = 0.2$ respectively. All the boxes show f_b as a function of LSF, divided in six intervals of Q_f as Farias et al. (2015). Our results are denoted by red circles for SEG-IN and blue crosses for NO-SEG. The green solid line is the prediction of Farias et al. (2015). From this work.

7.1.3 LSF vs f_b after 9 Myr, with $Q_f \sim 0.5$

Half of the simulations of this work (160 for each mass distribution) have $Q_f \sim 0.5$ and are summarised in Fig. 7.3. Top panels show the results for simulations with uniform BG and bottom panels for a Plummer BG. Left panels started with $Q_{init} = 0.5$ and right panels with $Q_{init} = 0.2$. The symbols are as before.

We observe in the four panels, as before, that most of the results are below the prediction. For values of LSFs greater than 0.2 the prediction never matches with the average results. The prediction only approach to our results in the bottom panels for LSFs lower than 0.3 and SEG-IN mass distribution.

The average f_b shows small differences independent of the initial mass distribution.

It is also possible to observe that the average of f_b is very similar when the LSF increases, showing again a low dependency on this parameter.

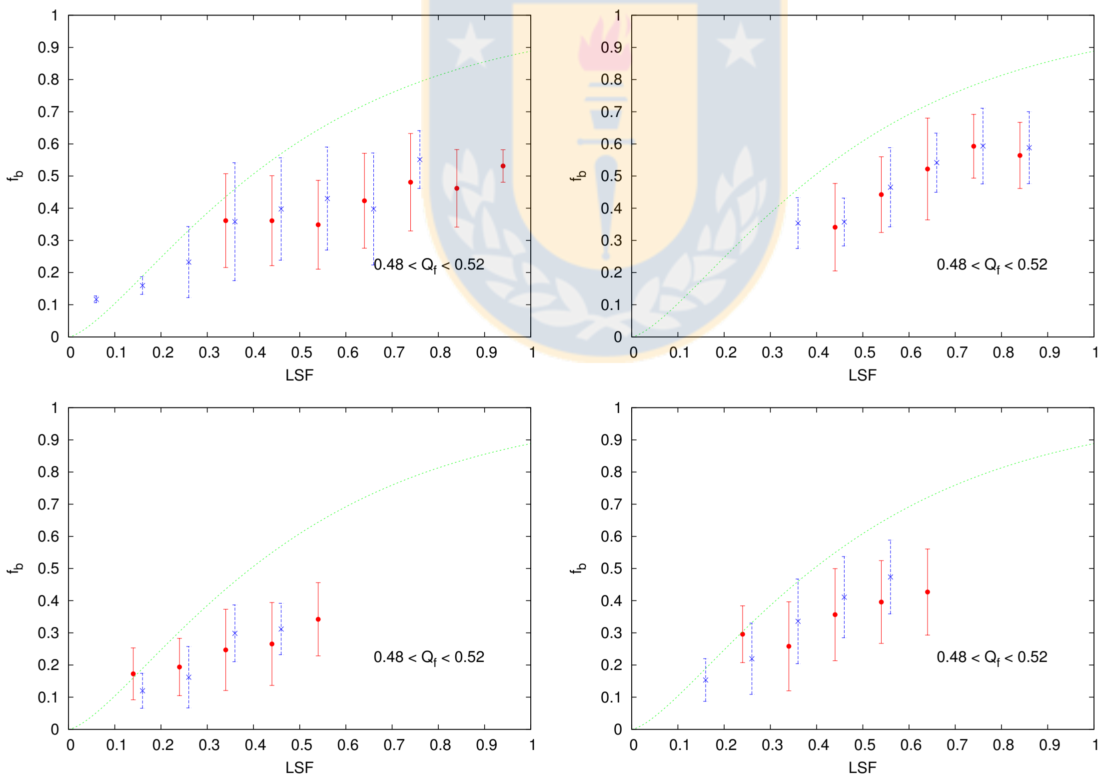

FIGURE 7.3: Panels show results for simulations after 9 Myr evolving without gas. Top and bottom panels with uniform BG and Plummer BG respectively. Left panels started with $Q_{init} = 0.5$ and right panels with $Q_{init} = 0.2$. All the panels show f_b as a function of LSF, for $Q_f \sim 0.5$. Our results are denoted by red circles for SEG-IN and blue crosses for NO-SEG. The green solid line is the prediction of Farias et al. (2015). From this work.

7.2 Dependency of f_b on the time evolution

In order to test if the evolution of the cluster is rapid because of two-body effects, we also measure f_b at 4 and 2 Myr after gas expulsion. The results are shown as we did previously (see e.g. Fig. 7.2) in the following subsections.

7.2.1 LSF vs f_b after 4 Myr, embedded in a uniform BG

Fig. 7.4 shows the results of the simulations with a uniform BG, after evolving without gas for 4 Myr. The order and symbols are as in Fig. 7.2.

The results cover the parameters ranges, as they are the same simulations than before, so Q_f and LSF are the same. The changes are only observed for f_b as we are measuring at 4 Myr after the gas expulsion.

In the top panel, we observe that the results are now closer to the prediction but still in most of the cases below to the curve.

The average of f_b is again practically independent of the initial mass distribution.

It is also possible to observe that f_b changes only by small amount, although is now more sensitive to LSF variations.

In the bottom panel, it is possible to observe in the first box, enough good agreement between the results and prediction, at least of NO-SEG cases. For SEG-IN, in this box, we only have one point, not enough to observe a trend. For the rest of the results, they are always below to the curve with small changes in f_b as LSF increases (second and third box).

7.2.2 LSF vs f_b after 4 Myr, embedded in a Plummer BG

Fig. 7.5 shows the results of the simulations with a Plummer BG, after evolving without gas for 4 Myr. The order and symbols are as in Fig. 7.2.

In the top panel, we note a better agreement with the prediction for low LSFs (<0.3) and disagree for higher LSFs values.

The average f_b in the bottom boxes is showing some differences dependent on the initial mass distribution, but still agree their error-bars.

Also here, small differences are observed on the average of f_b as the LSF increases.

In the bottom panel, we observe as before a better agreement for low LSFs (<0.3), but the results disagree with higher LSFs values.

The differences observed on the average of f_b as the LSF increases are small as in all the previous cases.

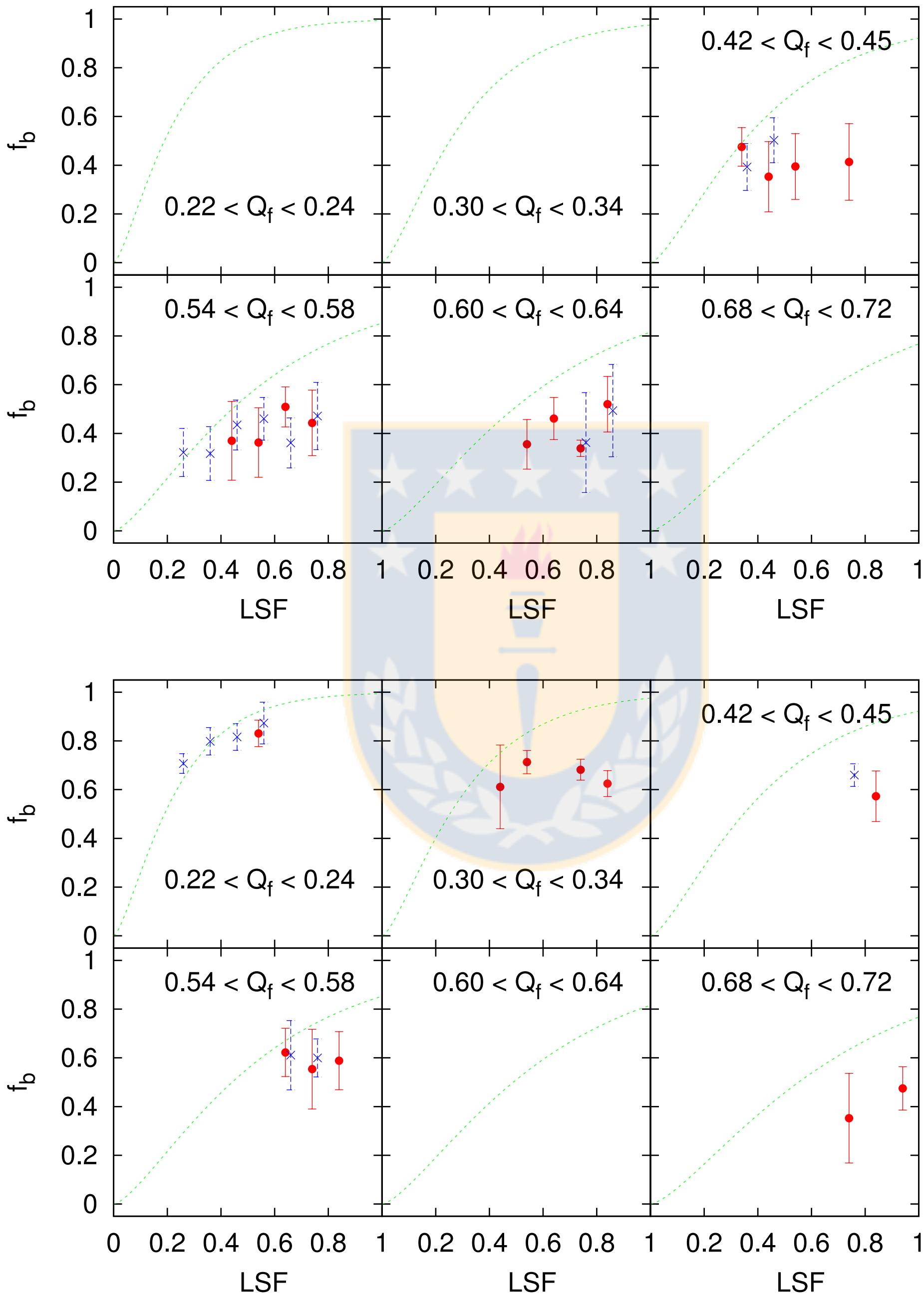

FIGURE 7.4: Both panels show results for simulations with uniform BG after 4 Myr evolving without gas. Top and bottom panels with $Q_{init} = 0.5$ and $Q_{init} = 0.2$ respectively. All the boxes show f_b as a function of LSF, divided in six intervals of Q_f as Farias et al. (2015). Our results are denoted by red circles for SEG-IN and blue crosses for NO-SEG. The green solid line is the prediction of Farias et al. (2015). From this work.

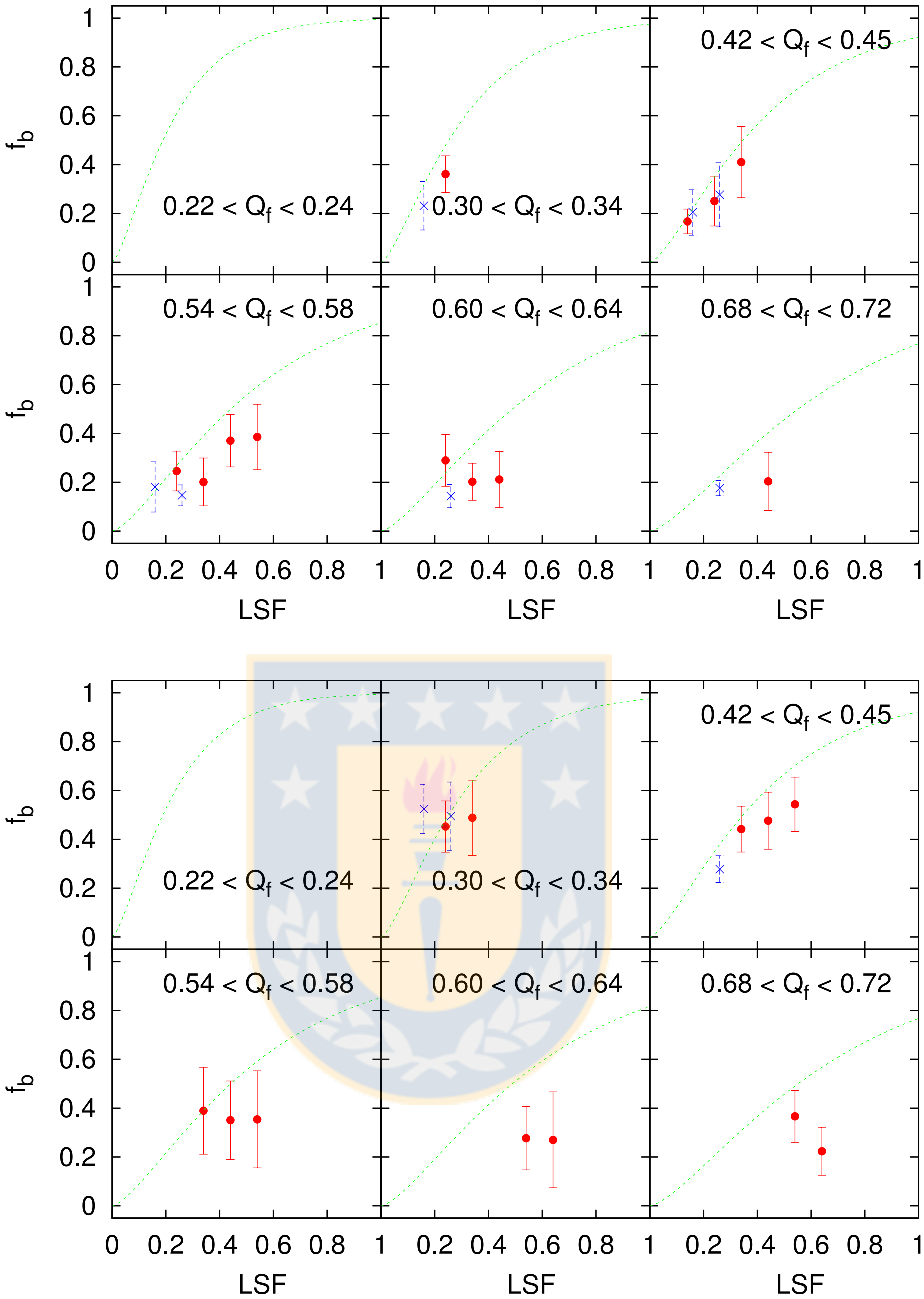

FIGURE 7.5: Both panels show results for simulations with Plummer BG after 4 Myr evolving without gas. Top and bottom with $Q_{init} = 0.5$ and $Q_{init} = 0.2$ respectively. All the boxes show f_b as a function of LSF, divided in six intervals of Q_f as Farias et al. (2015). Our results are denoted by red circles for SEG-IN and blue crosses for NO-SEG. The green solid line is the prediction of Farias et al. (2015). From this work.

7.2.3 LSF vs f_b after 4 Myr, with $Q_f \sim 0.5$

As before we measure f_b after 4 Myr of gas expulsion, for a $Q_f \sim 0.5$ where we have more statistics. The results are summarized in Fig. 7.6. Top panels are the results for simulations with uniform BG and bottom panels for Plummer BG. Left panels started with $Q_{init} = 0.5$ and right panels with $Q_{init} = 0.2$. The symbols are as before.

We observe in the four panels, that the results are closer to the prediction but still most of them are below the curve. For values of LSFs greater than 0.4 the prediction never match with the average results. Some the results are approaching if we take into account error-bars.

The average f_b is practically the same independent of the initial mass distribution.

It is also possible to observe as before that the average of f_b is very similar when the LSF increases, showing again a low dependency on this parameter.

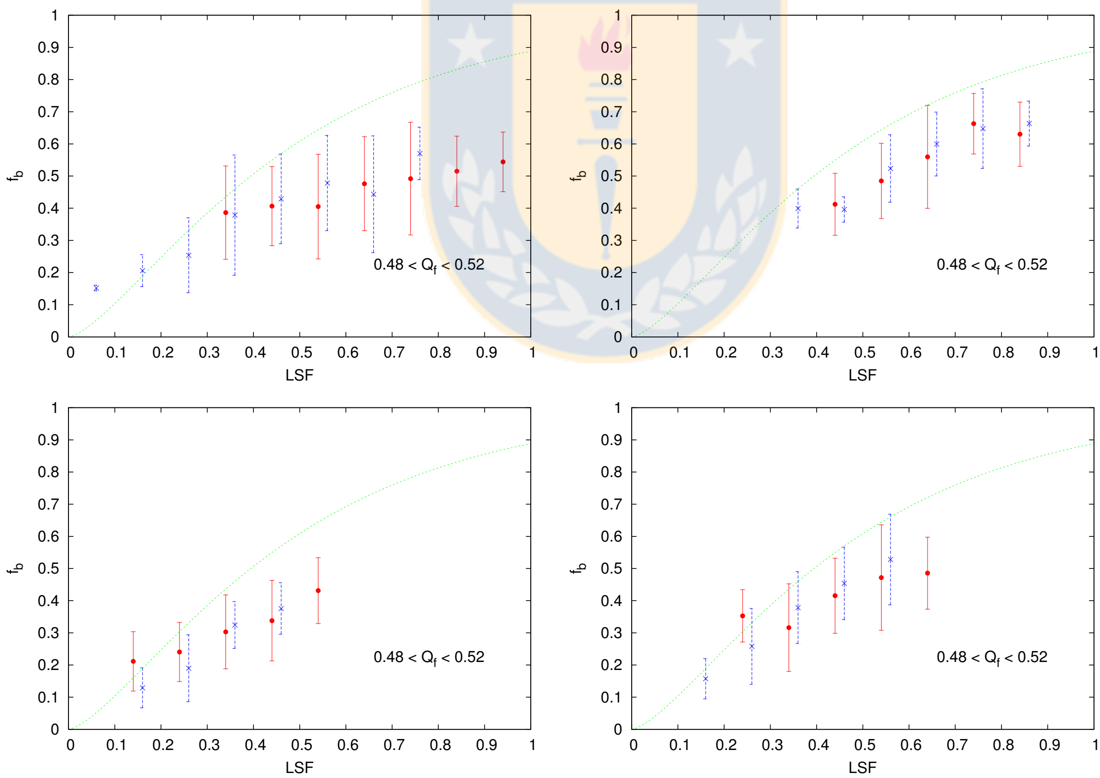

FIGURE 7.6: Panels show results for simulations after 4 Myr evolving without gas. Top and bottom panels with uniform BG and Plummer BG respectively. Left panels started with $Q_{init} = 0.5$ and right panels with $Q_{init} = 0.2$. All the panels show f_b as a function of LSF, for $Q_f \sim 0.5$. Our results are denoted by red circles for SEG-IN and blue crosses for NO-SEG. The green solid line is the prediction of Farias et al. (2015). From this work.

7.2.4 LSF vs f_b after 2 Myr, embedded in an uniform BG

Fig. 7.7 shows the results of the simulations with a uniform BG, after evolving without gas for 2 Myr. The order and symbols are as before.

In the top panel is possible to observe that the prediction is closer than before to the results even for high LSFs, but still failing more for the highest values of LSFs.

The average f_b values are as before practically the same independent of initial mass distribution.

In the bottom panel, we also observe that the prediction agrees in most of the cases even for higher LSFs as the first and sixth box show.

The largest discrepancy is observed in the sixth box, where the prediction is still close to the error-bars but the discrepancies may be driven by low number statistics.

We observe again that f_b is almost the same for different initial mass distributions.

7.2.5 LSF vs f_b after 2 Myr, embedded in a Plummer BG

Fig. 7.8 shows the results of the simulations with a Plummer BG, after evolving without gas for 2 Myr. The order and symbols are as before.

In the top panel, the prediction agrees or with few discrepancies in most of the cases. The discrepancy increases with higher LSFs.

We observe in the third and fourth boxes practically the same average of f_b independent of the initial mass distribution.

In the bottom panel, we also observe that the prediction is closer to the results.

In the bottom boxes, there is almost no dependence on the LSFs for the averages of f_b. They look approximately constant.

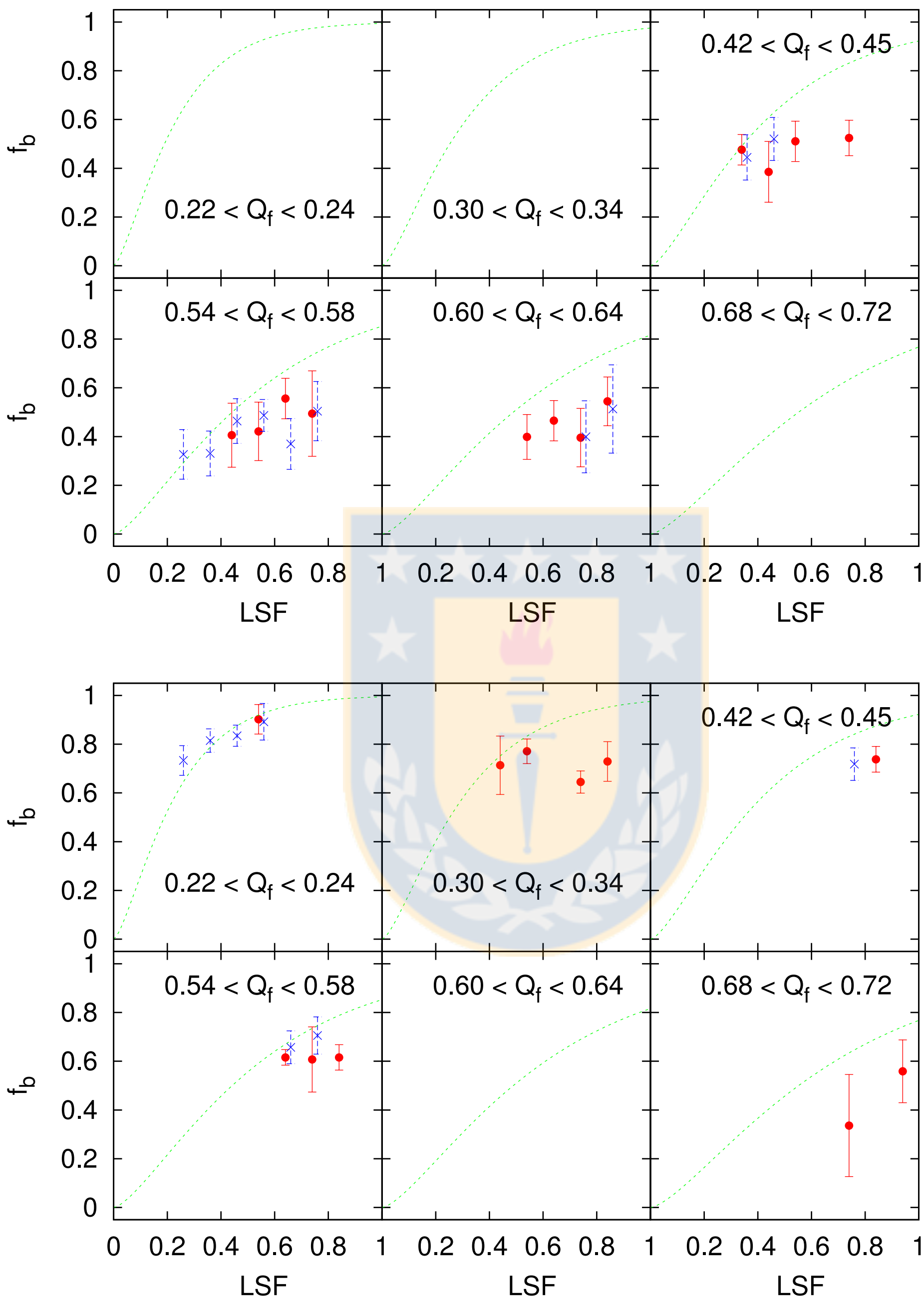

FIGURE 7.7: Both panels show results for simulations with uniform BG after 2 Myr evolving without gas. Top and bottom panels with $Q_{init} = 0.5$ and $Q_{init} = 0.2$ respectively. All the boxes show f_b as a function of LSF, divided in six intervals of Q_f as Farias et al. (2015). Our results are denoted by red circles for SEG-IN and blue crosses for NO-SEG. The green solid line is the prediction of Farias et al. (2015). From this work.

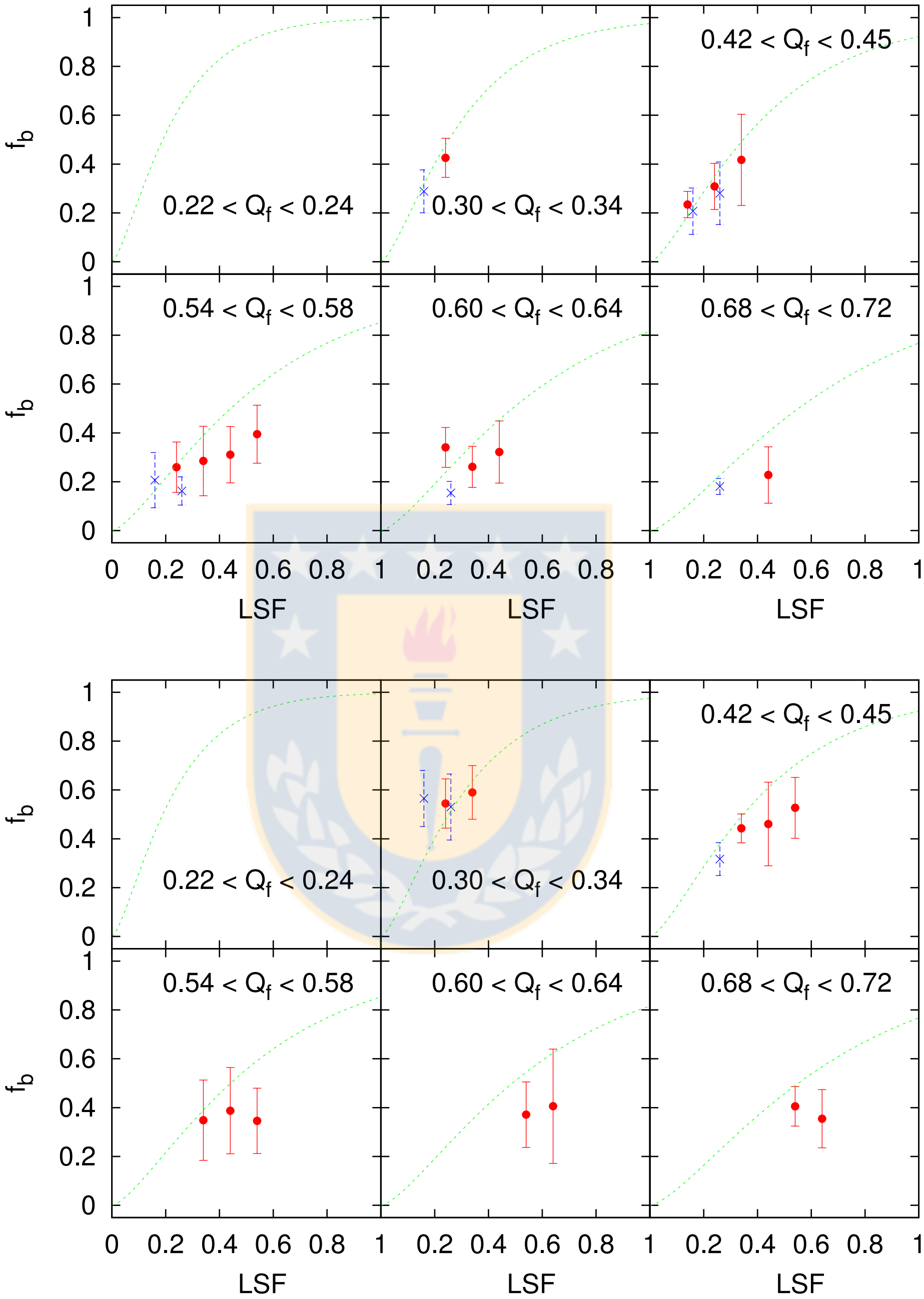

FIGURE 7.8: Both panels show results for simulations with Plummer BG after 2 Myr evolving without gas. Top and bottom panels with $Q_{init} = 0.5$ and $Q_{init} = 0.2$ respectively. All the boxes show f_b as a function of LSF, divided in six intervals of Q_f as Farias et al. (2015). Our results are denoted by red circles for SEG-IN and blue crosses for NO-SEG. The green solid line is the prediction of Farias et al. (2015). From this work.

7.2.6 LSF vs f_b after 2 Myr, with $Q_f \sim 0.5$

We also measure f_b after 2 Myr of gas expulsion, for a $Q_f \sim 0.5$ where we have more statistics. The results are summarized in Fig. 7.9. The symbols and order are as before.

The four panels show enough good agreement between the results and prediction for LSFs < 0.4. The discrepancies are become larger for higher LSFs, showing in the top-right panel.

Independent of the initial mass distribution the average of f_b is practically the same.

The average of f_b exhibits small changes at high LSFs.

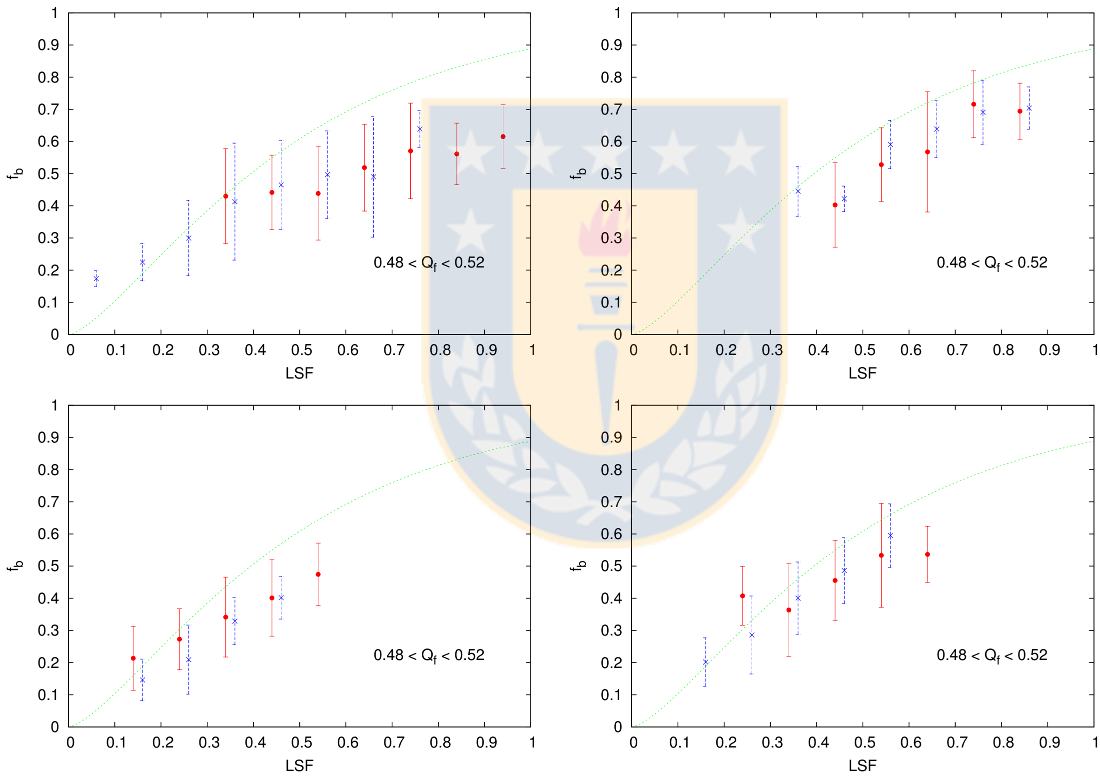

FIGURE 7.9: Panels show results for simulations after 2 Myr evolving without gas. Top and bottom panels with uniform BG and Plummer BG respectively. Left panels started with $Q_{init} = 0.5$ and right panels with $Q_{init} = 0.2$. All the panels show f_b as a function of LSF, for $Q_f \sim 0.5$. Our results are denoted by red circles for SEG-IN and blue crosses for NO-SEG. The green solid line is the prediction of Farias et al. (2015). From this work.

7.3 Dependency on Λ_{MST}

The prediction of Farias et al. (2015) was developed for simulations with equal-mass particles. In this work, we add that the stars have different masses. To address that the inclusion of an IMF will alter the results will alter the results significantly from the prediction, we show in Fig. 7.10 the simulations and their Λ_{MST} parameter. Each simulation which has a result within $|\Delta \mathrm{f_b}| < 0.1$ ($|\Delta \mathrm{f_b}|$ is the deviation from the prediction) is marked as green circle and, if $|\Delta \mathrm{f_b}| > 0.1$ then we mark the simulations as red square. The top panel shows results of the measurements for 9 Myr and the bottom panel for 2 Myr after gas expulsion.

We show the results for the complete sample of simulations (N=2560) and, we observe that the prediction works in a few cases independent of the influence of the different masses or level of MS which we quantified using Λ_{MST} parameter.

We can observe more green filed squares in the top right panel which started with NO-SEG mass distribution. On the other hand, in the top left panel green squares are practically no observable.

In the bottom panels, green squares increase their frequency, but still in minority, for both initial mass distributions.

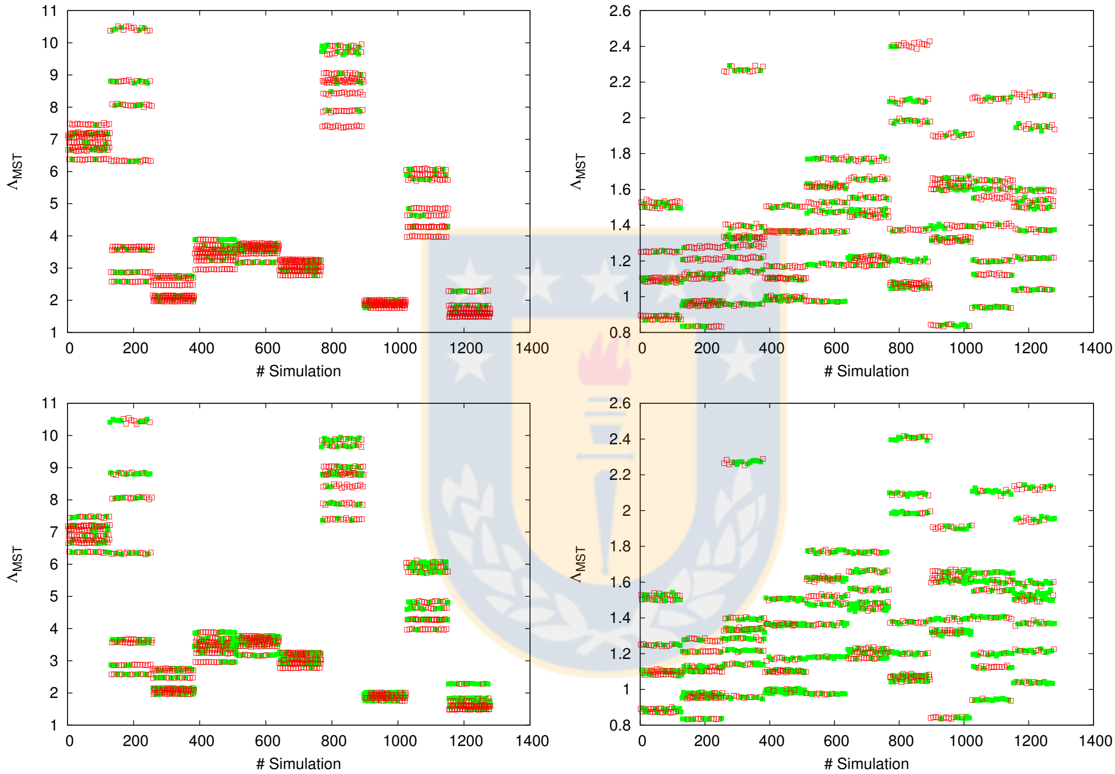

FIGURE 7.10: Influence of Λ_{MST} over prediction in top panels for 9 Myr and bottom for 2 Myr, after evolving without gas. Left panels for SEG-IN cases and right panels for NO-SEG cases. Green filled squares mean that the predictions agree and red open squares mean that the predictions disagree. From this work.

7.4 Evaporation

From the previous results, it is possible to observe that the discrepancy between the results and the prediction becomes larger as a function of time. To scrutinise this behaviour in more detail, we follow the bound fraction for the entire duration of the simulation. We compare the f_b with the bound fraction at the moment of the gas expulsion (f_{bexp}). If evaporation is producing an effect the difference will be less than 0, ($f_b - f_{bexp} < 0$). We only use the results with $Q_f \sim 0.5$, where we have more statistics. We show the average evaporation of the clusters quantified by $f_b - f_{bexp}$ along the time after gas expulsion. The different symbols are for different ranges of LSF and green solid line is denoting the zero point of f_{bexp}. As we are using negative numbers, a decreasing value of $f_b - f_{bexp}$ means that evaporation after gas-expulsion become more important. We define $f_b - f_{bexp} > -0.1$ as not significant evaporation. On the other hand, if the value is $<$ -0.1, we consider this as a significant value of evaporation. We summarise the results for the different cases in the following subsections. We call first, second and next ranges, as they are showed in the legend of each figure.

7.4.1 Time vs $f_b - f_{bexp}$, with $Q_{init} = 0.5$ and uniform BG

In Fig. 7.11 we show the results for $Q_{init} = 0.5$ and uniform BG. In the top panels, we show the results for the NO-SEG mass distribution. Top-left panel shows that, with exception of the first range, as LSF increase the evaporation is increasing. For LSF < 0.5 the maximum value of evaporation is $>$ -0.1, that is, not a significant value of evaporation. On the other hand, the top-right panel shows practically the same evaporation for the first and second range of LSF. A higher evaporation is observed for the third range. The values of evaporation are < -0.18 and we say that they show a significant evaporation.

The bottom panel shows the results for SEG-IN mass distribution. As the LSF becomes larger the evaporation also increases. The second and fourth range are two exceptions to this trend. The values of evaporation are < -0.15 and, they show significant evaporation.

7.4.2 Time vs $f_{bexp} - f_b$, with $Q_{init} = 0.2$ and uniform BG

In Fig. 7.12 we show the results for $Q_{init} = 0.2$ and uniform BG. In the left panel, we show the results for NO-SEG mass distribution. With exception of the second and third range, as LSF increases the evaporation increases. The values of evaporation are < -0.15 so, a significant evaporation.

The right panel shows the results for SEG-IN mass distribution. The first range is the only one exception to the previous trend. The values of evaporation are < -0.18 i.e. a significant evaporation as we defined before.

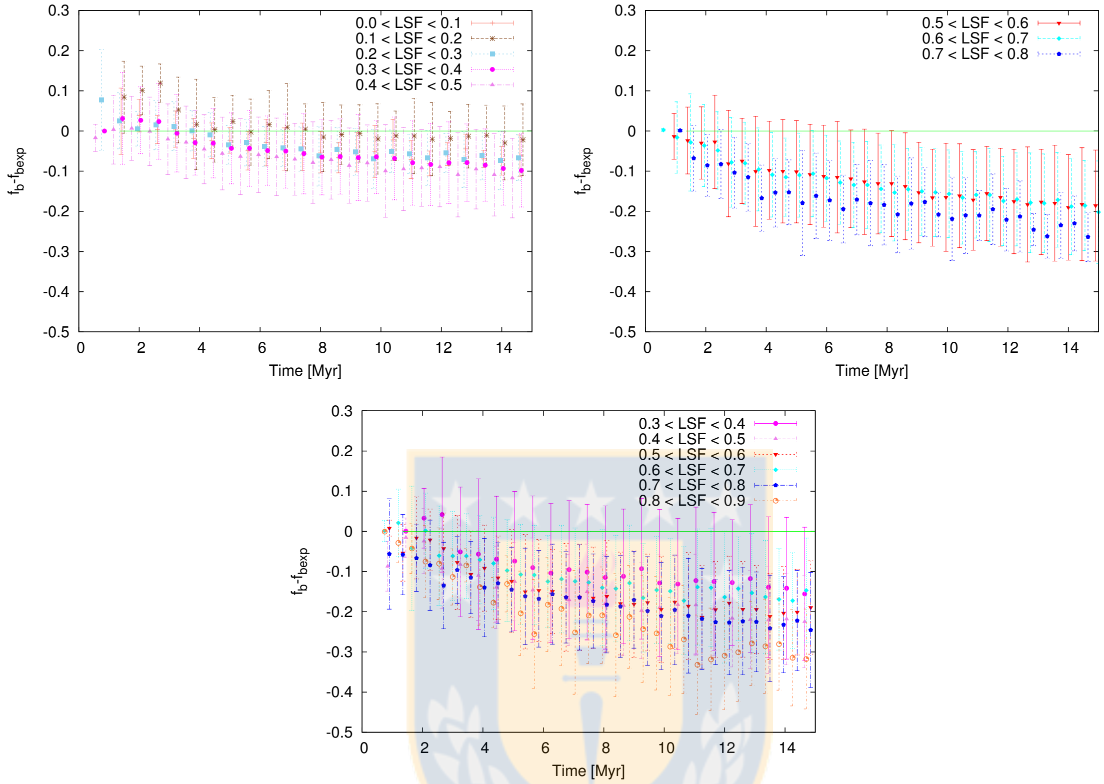

FIGURE 7.11: Time vs average $f_b - f_{bexp}$, for uniform BG, $Q_{init} = 0.5$ and $Q_f \sim 0.5$. The different symbols denote the ranges of LSF and green solid line is denoting the point zero of f_{bexp}. Top panels show the results for NO-SEG cases, with left panel showing insignificant evaporation and right panel showing significant evaporation. Bottom panel for SEG-IN case with significant evaporation. From this work.

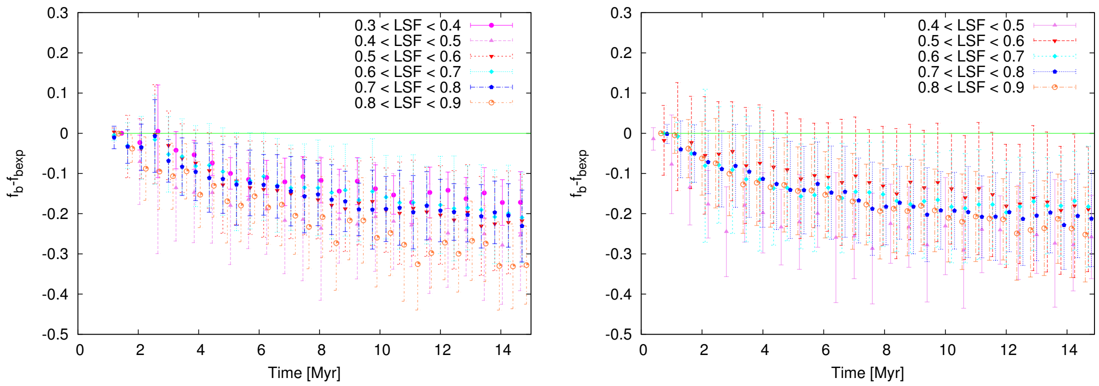

FIGURE 7.12: Time vs average $f_{bexp} - f_b$, for uniform BG, $Q_{init} = 0.2$ and $Q_f \sim 0.5$. The different symbols denote the ranges of LSF and green solid line is denoting the point zero of f_{bexp}. Left panel shows the results for NO-SEG cases and right panel for SEG-IN cases, both with significant evaporation. From this work.

7.4.3 Time vs $\mathbf{f_{bexp} - f_b}$, with $\mathbf{Q_{init}} = 0.5$ and Plummer BG

In Fig. 7.13 we show the results for $Q_{init} = 0.5$ and Plummer BG. In the top panels, we show the results for NO-SEG mass distribution. Top-left panel shows again the previous trend, as LSF increases the evaporation increases. The maximum value of evaporation is $>$ -0.1 with an insignificant value of evaporation. On the other hand, the top-right panel shows practically the same evaporation for the first and second range of LSF, reaching values $<$ -0.15, i.e. significant evaporation.

The bottom-left panel shows the results for SEG-IN mass distribution. As the LSF becomes larger the evaporation also increases with many results showing insignificant evaporation. The bottom-right panel shows values $<$ -0.18 i.e. significant evaporation.

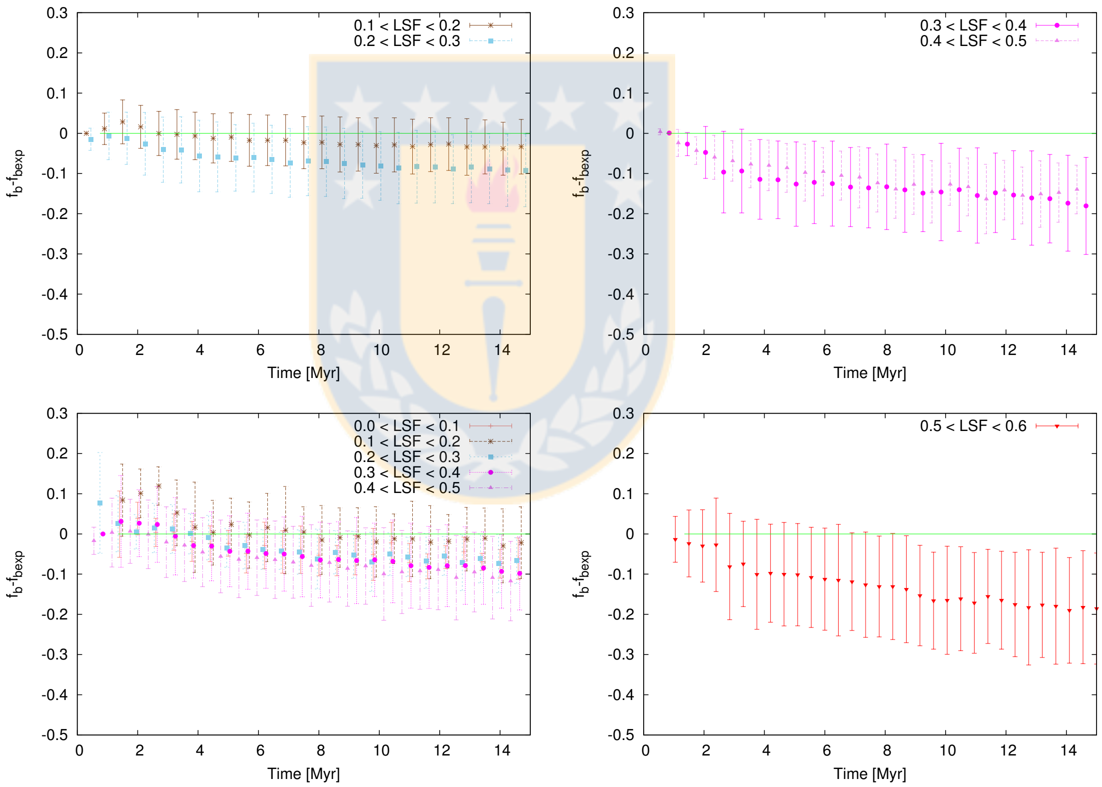

FIGURE 7.13: Time vs average $f_b - f_{bexp}$, for Plummer BG, $Q_{init} = 0.5$ and $Q_f \sim 0.5$. The different symbols denote the ranges of LSF and green solid line is denoting the point zero of f_{bexp}. Top panels show the results for NO-SEG cases and bottom panels for SEG-IN cases. Left panels are showing insignificant evaporation and right panel are showing significant evaporation. From this work.

7.4.4 Time vs $\mathbf{f_{bexp} - f_b}$, with $\mathbf{Q_{init}} = 0.2$ and Plummer BG

In Fig. 7.14 we show the results for $Q_{init} = 0.2$ and Plummer BG. In the top panels, we show the results for NO-SEG mass distribution. Top-left panel shows a maximum value of evaporation is $>$ -0.1. On the other hand, the top-right panel shows the same trend observed before, reaching values $<$ -0.12, which means a significant evaporation.

The bottom panel shows the results for SEG-IN mass distribution. We again observe as the LSF becomes larger the evaporation also increases. The maximum evaporation value is < -0.18, producing a significant evaporation.

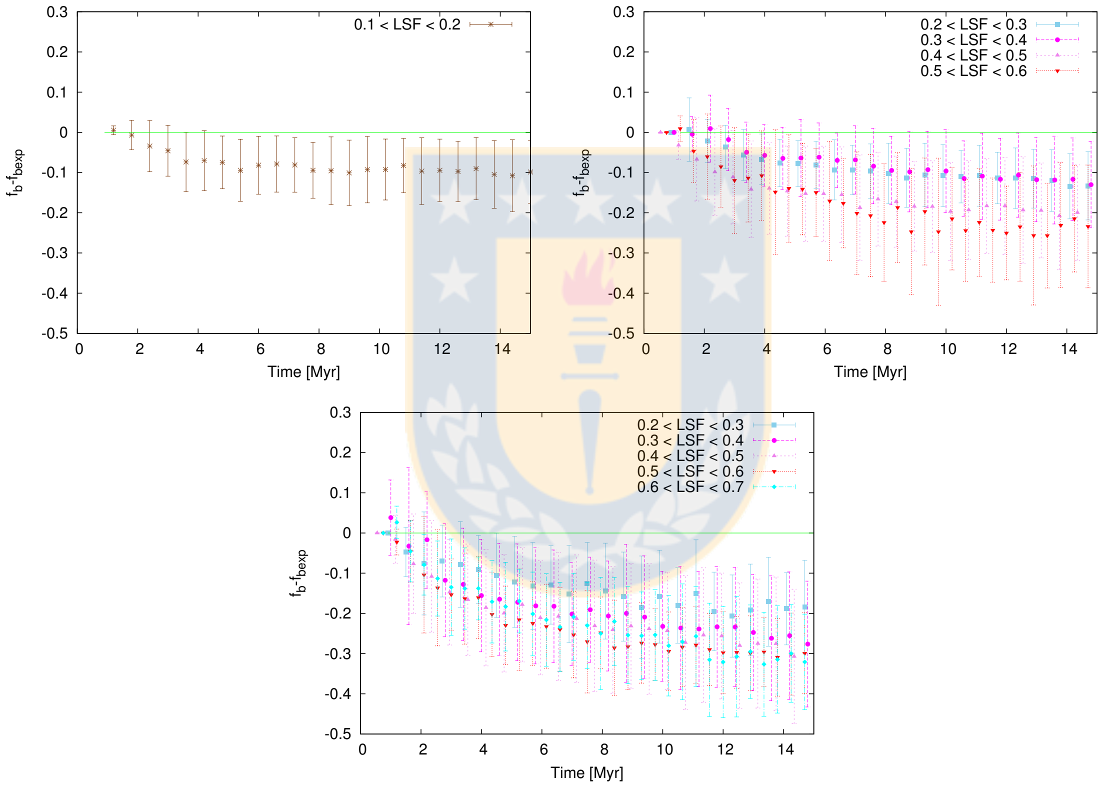

FIGURE 7.14: Time vs average $f_b - f_{bexp}$, for Plummer BG, $Q_{init} = 0.2$ and $Q_f \sim 0.5$. The different symbols denote the ranges of LSF and green solid line is denoting the point zero of f_{bexp}. Top panels show the results for NO-SEG cases, with left panel showing insignificant evaporation while right panel showing significant evaporation. Bottom panel for SEG-IN case with significant evaporation. From this work.

7.4.5 Time vs $f_{bexp} - f_b$, for Equal-mass simulations

In order to justify if the evaporation of the clusters is producing the discrepancy between the prediction and the results of this work, we measure the values of evaporation for equal-mass simulations.

The top panels show the results for simulations with uniform BG with $Q_{init} = 0.5$ (left panel) and $Q_{init} = 0.2$ (right panel). The middle panels show the results for simulations with Plummer BG with $Q_{init} = 0.5$ (left panel) and $Q_{init} = 0.2$ (right panel). The four panels show $f_{bexp} - f_b > -0.1$, i.e. no significant evaporation values even for high values of LSF. In the top panels the final values of evaporation are very similar. The last behavior is not observable in the middle left panel.

On the other hand, the simulations which started with $Q_{init} = 0.2$, have a counterpart with $f_{bexp} - f_b < -0.12$. In the bottom-left panel for an uniform BG is possible to observe one exception with LSF $>$ 0.5. In the bottom-left panel the average of the evaporation values are practically the same finishing with values $\sim$ -0.12, for LSF $>$ 0.3. Both panel have significant values of evaporation according to our definition.

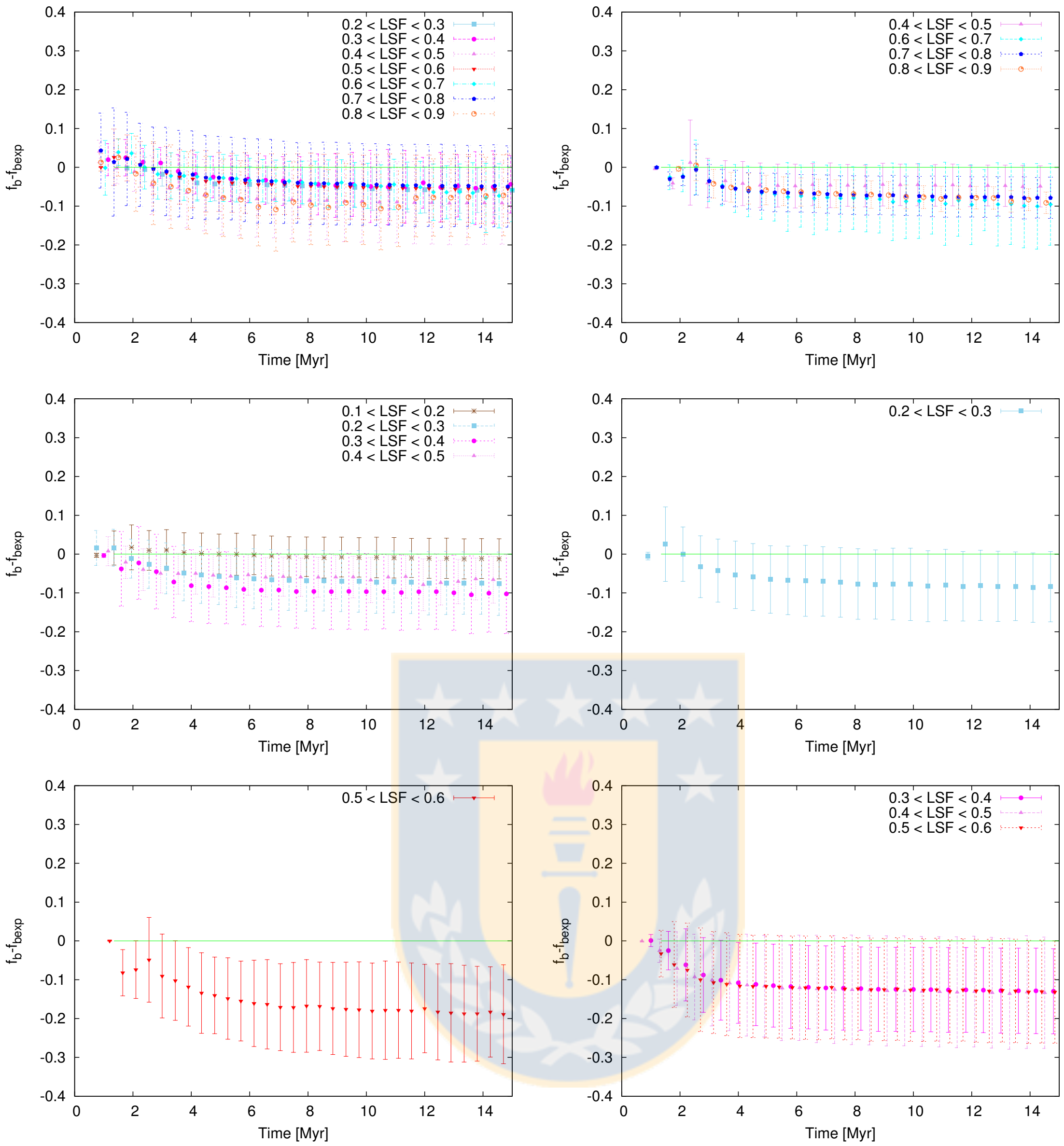

FIGURE 7.15: Time vs average $f_{bexp} - f_b$, with $Q_f \sim 0.5$ for equal-mass simulations. The different symbols denote the ranges of LSF and green solid line is denoting the point zero of f_{bexp}. Top panels have a uniform BG, left panel with $Q_{init} = 0.5$ and right panel with $Q_{init} = 0.2$. Middle panels have a Plummer BG, left panel with $Q_{init} = 0.5$ and right panel with $Q_{init} = 0.2$. The last four panels show the results with no significant evaporation values. Bottom panels show the results with significant evaporation values with $Q_{init} = 0.2$, left panel with uniform BG while right panel with Plummer BG. From this work.

7.5 New approaches

The objective of this section is to identify a better prediction when other parameters are analysed and combined.

7.5.1 Global Q_f as a predictor of f_b after 9 Myr

Fig. 7.16 shows the f_b as a function of Q_f. The order of the panel and the meaning of the symbols are as in Fig. 7.3.

It is possible to observe a decreasing trend in the right panels, but not in the bottom-left panel where f_b is practically constant independent Q_f.

The average f_b in most of the cases, is very similar, independent of initial mass distribution.

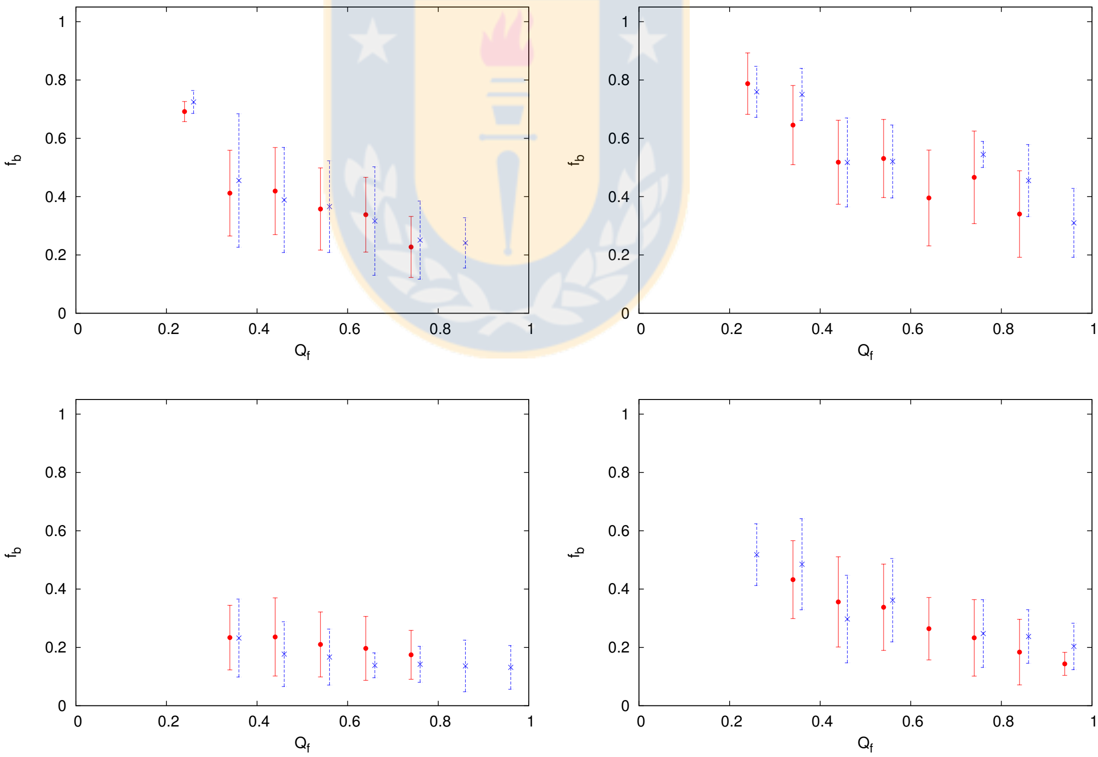

FIGURE 7.16: Comparison between f_b as a function of Q_f (Q using gas and stars). Top panels show results for simulations with uniform BG. Bottom panels show results for simulations with Plummer BG. Left panels started with $Q_{init} = 0.5$ and right panels with $Q_{init} = 0.2$. Red circles for SEG-IN and blue crosses for NO-SEG. From this work.

7.5.2 Bound stars Q_{fb} as a predictor of f_b, after 9 Myr

In the previous results Q_f was measured taking into account the gas where the clusters were embedded. As the gas is instantaneously expelled in this work, stars have not moved yet and we can measure the Q_f of the stars alone now. We furthermore restrict ourselves on only the bound stars.

Fig. 7.17 shows the f_b as a function of Q measured only with stars which were bound at the moment of the gas expulsion (Q_{fb}). The order of the panels and the meaning of the symbols are as in Fig. 7.3.

No clear trend is observable for the four panels. It is important to mention that as we are not taking into account the gas, we measured values of Q_{fb} larger than one i.e. super-virial.

As before the average f_b, in most of the cases, is very similar independent of initial mass distribution.

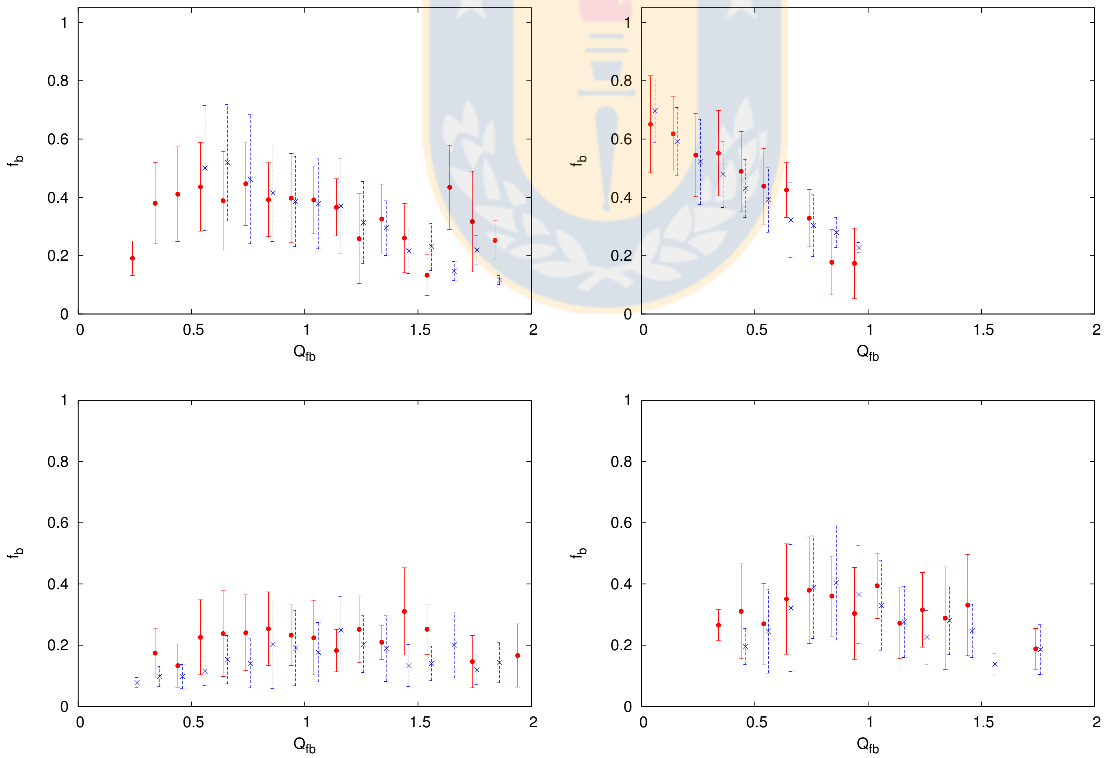

FIGURE 7.17: Comparison between f_b as a function of Q_{fb} (Q only using bound stars). Top panels show results for simulations with uniform BG. Bottom panels show results for simulations with Plummer BG. Left panels started with $Q_{\rm init} = 0.5$ and right panels with $Q_{\rm init} = 0.2$. Red circles for SEG-IN and blue crosses for NO-SEG. From this work.

7.5.3 All stars Q_{fg} as a predictor of f_b after 9 Myr

Excluding stars around the principal clump can be a source of error. For this reason, we also compare the global Q of the all the stars of the cluster (Q_{fg}), again ignoring the gas.

Fig. 7.18 shows the results of f_b as a function of Q_{fg}. The order of the panels and the meaning of the symbols are as in Fig. 7.3.

It is possible to observe a decreasing trend in the four cases. This is less appreciable in the third panel but still present. Even when it is possible to observe a trend, the results are occupying different locations in the plot, indicating a possible dependence on extra parameters.

Again the average f_b, in most of the cases, is very similar independent of initial mass distribution.

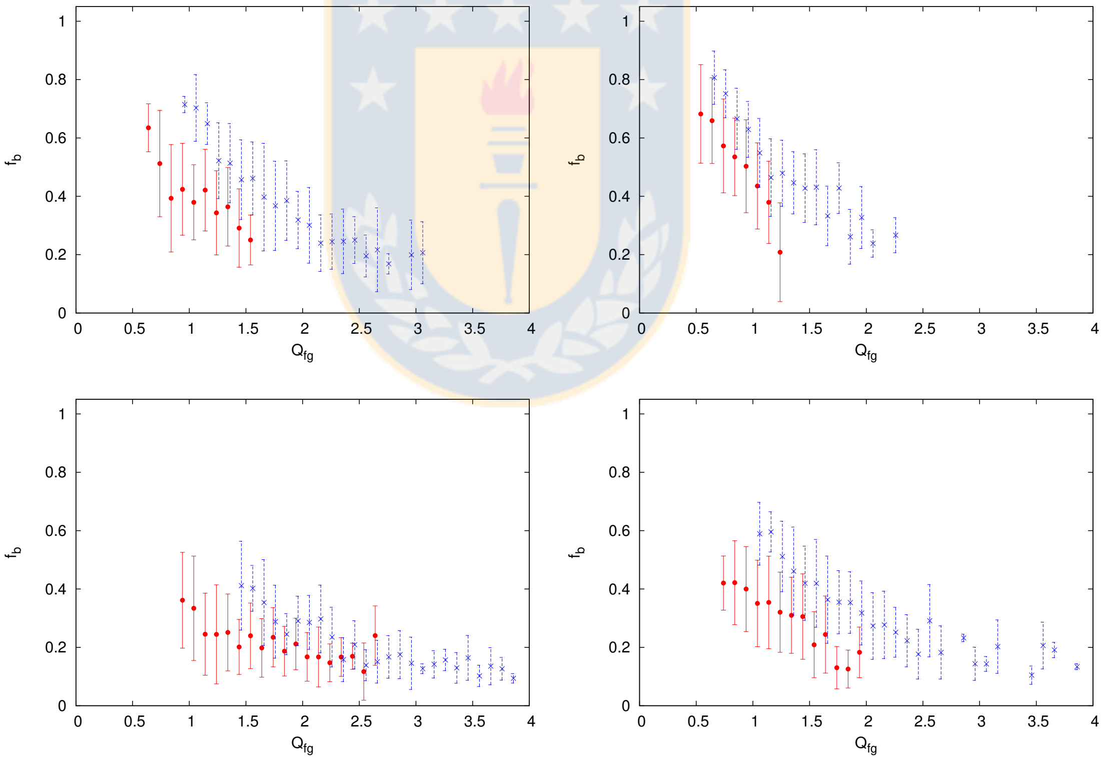

FIGURE 7.18: Comparison between f_b as a function of Q_{fg} (Q only using stars). Top panels show results for simulations with uniform BG. Bottom panels show results for simulations with Plummer BG. Left panels started with $Q_{init} = 0.5$ and right panels with $Q_{init} = 0.2$. Red circles for SEG-IN and blue crosses for NO-SEG. From this work.

7.5.4 Joining Λ_{MST} and $\mathrm{Q_{fg}}$ as a predictor of $\mathrm{f_b}$ after 9 Myr

Until now we have not been considering the effects of MS, as an important parameter in the future evolution of the clusters. It is also important to take into account the $\mathrm{f_b}$ at the moment of the gas expulsion ($\mathrm{f_{bexp}}$), which is an upper limit for the final surviving cluster. In Fig. 7.18 we observe a decreasing trend in the four panels, but as they are occupying different locations in the plot, it is possible that the results have some dependence on other parameters. We test as extra parameters Λ_{MST} and $\mathrm{f_{bexp}}$. We find a trend using the following conjugation of parameters:

$$X = \log\left(\frac{\mathrm{Q_{fg}} * (\Lambda_{\mathrm{MST}})^{0.5}}{\mathrm{f_{bexp}}}\right) \tag{7.1}$$

Fig. 7.19 shows the results using the last transformation. The symbols are as the Fig. Fig. 7.3 and the green dashed line is the fit which is described by the equation:

$$\mathrm{f_{bexp}} = -0.0505X^3 + 0.3473X^2 - 0.8214X + 0.7461 \tag{7.2}$$

It is possible to observe that most of the averages of $\mathrm{f_b}$ are very close to the curve for every value of X.

In the four panels the average $\mathrm{f_b}$, in most of the cases, is very similar independent of initial mass distribution.

Fig. 7.20 shows the same fit (green dashed line), but now compared with the equal-mass results. Red empty circles symbols are for results with uniform BG and $\mathrm{Q_{init}} = 0.5$. Blue filled circles symbols denote results with uniform BG and $\mathrm{Q_{init}} = 0.2$. Plummer results with $\mathrm{Q_{init}} = 0.5$ and $\mathrm{Q_{init}} = 0.2$ are showed with cyan empty and magenta filled squares respectively. The fit agrees with small differences. It is possible to note only five exceptions.

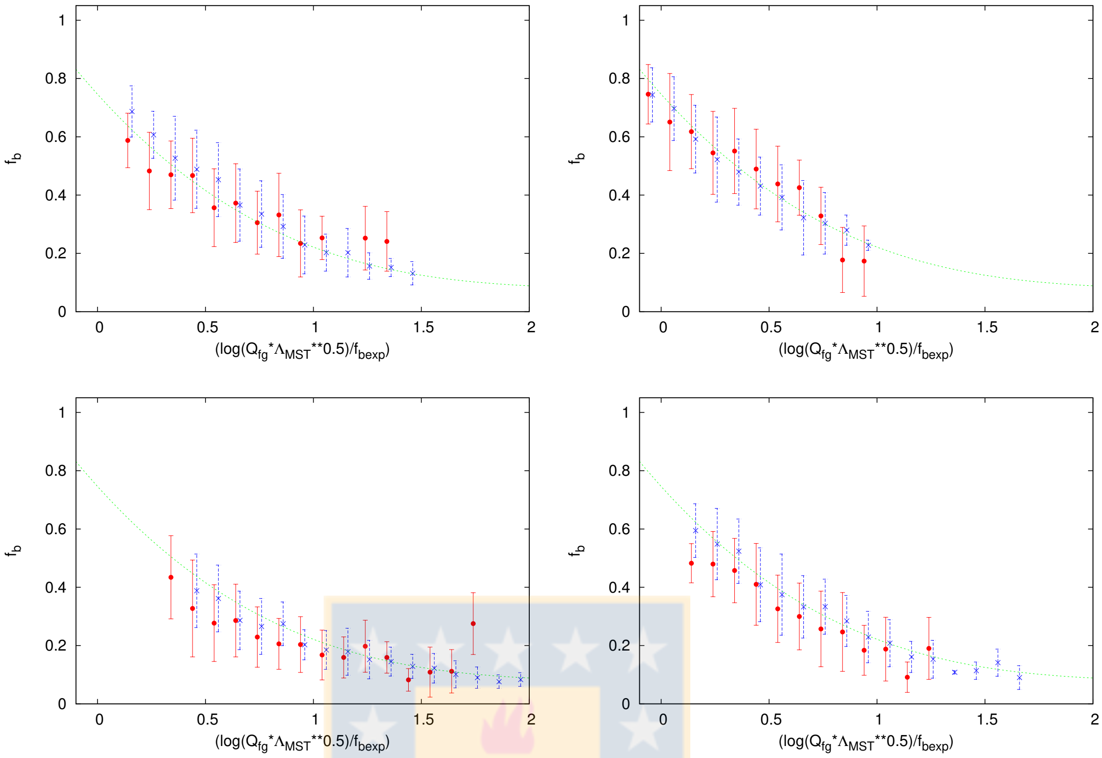

FIGURE 7.19: Comparison between f_b as a function of X. Top panels show results for simulations with uniform BG. Bottom panels show results for simulations with Plummer BG. Left panels started with $Q_{init} = 0.5$ and right panels with $Q_{init} = 0.2$. Red circles for SEG-IN, blue crosses for NO-SEG and green solid line for the fit. From this work.

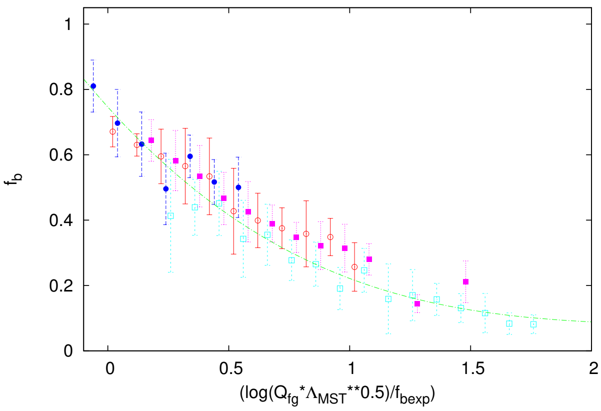

FIGURE 7.20: Comparison between f_b as a function of X, for equal-mass simulations. Red empty circles symbols: uniform BG and $Q_{init} = 0.5$. Blue filled circles: uniform BG and $Q_{init} = 0.2$. Cyan empty squares: Plummer and $Q_{init} = 0.5$. Magenta filled squares: Plummer and $Q_{init} = 0.2$ Green solid line for the fit. From this work.

7.5.5 Joining $\Lambda_{\mathbf{MST}}$ and $\mathbf{Q_{fg}}$ as a predictor of $\mathbf{f_b}$ after 4 Myr

In order to test if the new fit approximation is sensitive to time evolution, we compare it with the results measured at 4 Myr after gas expulsion.

Fig. 7.21 shows the average values of X. The symbols are as in Fig. 7.3 and the green dashed line is the fit. The fit is still working but now in many cases underestimating the f_b with differences less than 0.1. The larger differences are observed for the simulations with a uniform BG.

Again in the four panels the average f_b is very similar independent of initial mass distribution.

Fig. 7.22 shows the results for equal-mass simulations. The symbols are as Fig. 7.20. The fit also agree as we previously observed, even with less time of evolution.

They show a small shift-up compared with the results of 7.20 which has 9 Myr of evolution.

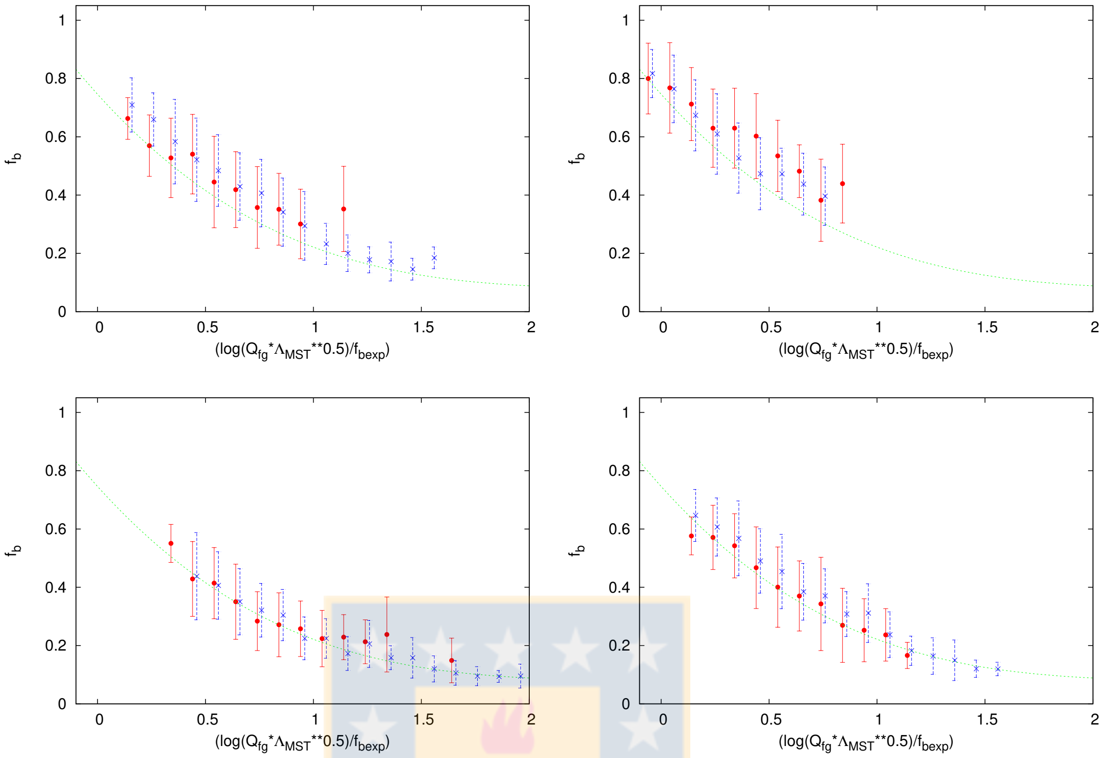

FIGURE 7.21: Comparison between f_b (after 4 Myr) as a function of X. Top panels show results for simulations with uniform BG. Bottom panels show results for simulations with Plummer BG. Left panels started with $Q_{init} = 0.5$ and right panels with $Q_{init} = 0.2$. Red circles for SEG-IN, blue crosses for NO-SEG and green solid line for the fit. From this work.

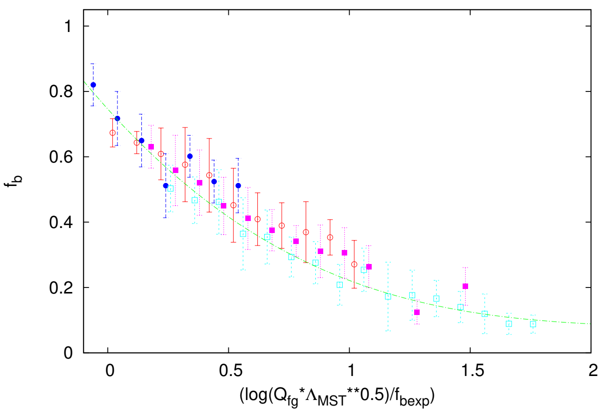

FIGURE 7.22: Comparison between f_b (after 4 Myr) as a function of X, for equal-mass simulations. Red empty circles symbols: uniform BG and $Q_{init} = 0.5$. Blue filled circles: uniform BG and $Q_{init} = 0.2$. Cyan empty squares: Plummer and $Q_{init} = 0.5$. Magenta filled squares: Plummer and $Q_{init} = 0.2$ Green solid line for the fit. From this work.

7.6 Discussion

In Sec. 7.1 it is clear that the prediction of Farias et al. (2015) in most of the cases is over predicting the f_b compared with the results obtained in this work, which are measured after 9 Myr of evolution. This becomes even clearer with higher LSF where the biggest discrepancies are observed.

Focusing now on Sec. 7.1.3, where we have more statistics, it is possible to observe that the averages of f_b are showing a small dependence of the values of LSF. For high LSF they almost follow a constant trend.

It is also possible to note on Sec. 7.1.3, that the results of f_b for SEG-IN and NO-SEG are very similar. This behaviour is in agreement with the results observed in Sec. 4.1, where simulations which start with NO-SEG mass distributions segregate very fast (< 1 Myr). In our simulations the gas expulsion happens in ranges 0.8 Myr $< t_{exp} <$ 2.2 Myr, as Fig. 6.6 shows, so the SCs have enough time to segregate and keep evolving as a segregated SC. The small differences shown in the results are because even when they are segregated, SCs do not have the exact same level of MS.

In Sec. 7.2 we reproduce the same study but measuring the f_b after 4 and 2 Myr of evolution. The results show a small shift up compared with the results for 9 Myr, logical due that they have less time to exchange energy and expel stars. In some cases, the results can reach the prediction but it continues failing for higher values of LSF.

Again focusing in results with $Q_f \sim 0.5$ at Sec. 7.2.3 and 7.2.6, the average of f_b even with the shift up, remains almost constant for high LSFs values and very similar for different initial mass-distribution.

The strict dependence on LSF observed by Farias et al. (2015) and Smith et al. (2011) for simulations with equal-mass particles, is not clearly observed. For LSFs > 0.4 in most of the cases, the average f_b is very similar, which indicates that the LSF is not describing the final f_b of the SCs anymore.

MS is affecting the further evolution and agreement of the prediction and results as the Sec. 7.3 shows. The results have more chances to approach the prediction if the SCs start not segregated i.e. NO-SEG. This is because as the clusters which are showing significant MS have more massive stars in the centre which are able to eject low-mass stars effectively. The results approach the prediction line if the time evolution is shorter, but still a minority of them. This indicates a fast evolution in the early time of evolution.

The prediction of Farias et al. (2015) was developed for equal-mass simulations. Adding an IMF, the evolution becomess faster as Sec 7.4 shows. Most of the averages finalise with evaporation values < -0.1 with a decreasing trend and, also can reach values < -0.2 for most of SEG-IN cases and/or initially cold. On the other hand, for equal-mass only dense configurations ($Q_{\rm init}$ = 0.2 and high LSF values) are able to show low but significant evaporations.. The evaporation trend is maintained practically constant, which produces higher f_b almost independent of the evolution time. Strong two-body encounters and MS which are not present in equal-mass simulations are producing the decreasing of the f_b in our study. The SCs with different masses do not stabilise as the the equal-mass SCs. They are continuously exchanging energy and expelling stars. This is the reason why we observe that the decreasing trend of evaporation is maintained along the entire simulation. The effect is stronger in simulations where we usually find a denser proto-cluster.

As the prediction of Farias et al. (2015) is not working to describe all our results we find a fit which can match better the results. In this fit we take into account the effect of the MS and $Q_{\rm fg}$, limited by $f_{\rm bexp}$ as a maximum where starts to decrease. The fit is independent of the initial conditions, but it is necessary to measure three parameters at the moment of gas expulsion. Sec 7.5.4 shows the agreement with the results and also works for equal-mass particles. Sec 7.5.5 shows that the fit also agrees, with a small shift for lower time evolution. This shift is almost no observable for equal-mass simulations due to low evaporation values.

Chapter 8

Conclusion: Survival of Embedded Star Clusters

We have presented simulations of fractal embedded star clusters with an initially cool or pseudo-virial state. The clusters start with two different initial levels of MS, namely NO-SEG and SEG-IN. We expel the gas at different times and measure the f_b after 9 Myr of the gas expulsion. We also measure f_b at different intermediate times to quantify the effects of evaporation. The results are then compared with the prediction of Farias et al. (2015) for simulations with equal-mass particles.

We conclude that the prediction of Farias et al. (2015) is not working for simulations with different masses. The prediction after 9 Myr fails for all cases with LSF > 0.4. For lower values of LSF, the prediction can match in some cases but still fail for many of the results. The prediction of Farias et al. (2015) shows an increasing trend of f_b as the LSF becomes higher, but we do not observe this behaviour in our results. A high value of LSF implies a small R_h, i.e. highly concentrated SCs, which when the support of the BG potential is removed, initially expel stars rapidly before reaching a phase when the expulsion declines at a constant rate as is consistent within the error-bars. Using the parameters spaces of Farias et al. (2015), it is possible to say that a value of LSF ~ 0.4 is describing the f_b for higher LSF values, as we observe very small changes as LSF becomes greater (almost constant trend). We observe that the prediction approach to the results if we compare with the f_b of earlier times, which is logical since we are measuring in points where the evaporation is less. Even if we measure f_b for early times, the global trend it is that the prediction fails in most of the cases.

The prediction of Farias et al. (2015) describes well the f_b for equal-mass particles simulations, where the two-body encounters and MS are avoided. These two issues lead to the process of evaporation to be quick and decreasing on time. On the other hand, equal-mass simulations show small values of evaporation and constant independent of the evolution time.

We conclude that for a better description of f_b, it is necessary to take into account at the moment of the gas expulsion the level of MS quantified by Λ_{MST}, Q_{fg} and f_{bexp}. Joining these parameters, we find a fit which can describe very well f_b after 9 Myr of evolution, independent of the initial conditions. The fit also works for equal-mass particles, supporting the importance of these parameters over Q_f and LSF, on which the prediction of Farias et al. (2015) are based. It is important to mention that even when the fit has a good agreement with results, it lacks a physical explanation, making necessary a deep study into the physics implications of MS and strong two-body encounters.

Bibliography

Aarseth, S. J. 2003, Gravitational N-Body Simulations, by Sverre J. Aarseth, pp. 430. ISBN 0521432723. Cambridge, UK: Cambridge University Press, November 2003., 430

Adams, F. C. 2000, ApJ, 542, 964

Adams, F. C., & Myers, P. C. 2001, ApJ, 553, 744

Ahmad, A., & Cohen, L. 1973, Journal of Computational Physics, 12, 389

Allison, R. J., Goodwin, S. P., Parker, R. J., et al. 2009, ApJL, 700, L99

Allison, R. J., Goodwin, S. P., Parker, R. J., Portegies Zwart, S. F., & de Grijs, R. 2010, MNRAS, 407, 1098

Antonov, V. A. 1962, Vestnik Leningradskogo Universiteta, Leningrad: University, 1962,

Auluck, F. C., & Kothari, D. S. 1965, ZAP, 63, 9

Bastian, N., & Goodwin, S. P. 2006, MNRAS, 369, L9

Bastian, N., Covey, K. R., & Meyer, M. R. 2010, ARA&A, 48, 339

Bate, M. R., Bonnell, I. A., & Bromm, V. 2003, MNRAS, 339, 577

Bate, M. R. 2009, MNRAS, 397, 232

Baumgardt, H., & Kroupa, P. 2007, MNRAS, 380, 1589

Bencivenni, D., Brocato, E., Buonanno, R., & Castellani, V. 1991, AJ, 102, 137

Benz, W., & Hills, J. G. 1987, ApJ, 323, 614

Binney, J., & Tremaine, S. 1987, Princeton, NJ, Princeton University Press, 1987, 747 p.,

Boily, C., & Kroupa, P. 2002, Modes of Star Formation and the Origin of Field Populations, 285, 141

Boily, C. M., & Kroupa, P. 2003, MNRAS, 338, 673

Bok, B. J. 1934, Harvard College Observatory Circular, 384, 1

Bonatto, C., & Bica, E. 2006, A&A, 455, 931

Bonnell, I. A., Bate, M. R., Clarke, C. J., & Pringle, J. E. 1997, MNRAS, 285, 201

Bonnell, I. A., & Davies, M. B. 1998, MNRAS, 295, 691

Bonnell, I. A., Bate, M. R., Clarke, C. J., & Pringle, J. E. 2001, MNRAS, 323, 785

Bonnell, I. A., Clarke, C. J., Bate, M. R., & Pringle, J. E. 2001, MNRAS, 324, 573

Bonnell, I. A., & Bate, M. R. 2006, MNRAS, 370, 488

Bonnell, I. A., Bate, M. R., & Vine, S. G. 2003, MNRAS, 343, 413

Carpenter, J. M., & Hodapp, K. W. 2008, Handbook of Star Forming Regions, Volume I, 4, 899

Cartwright, A., & Whitworth, A. P. 2004, MNRAS, 348, 589

Cayrel, R., Tarrab, I., & Richtler, T. 1988, The Messenger, 54, 29

Chavarría, L., Mardones, D., Garay, G., et al. 2010, ApJ, 710, 583

Chen, L., de Grijs, R., & Zhao, J. L. 2007, AJ, 134, 1368

Clark, P. C., & Bonnell, I. A. 2004, MNRAS, 347, L36

Cohn, H. 1980, ApJ, 242, 765

Eggleton, P. 2006, Evolutionary Processes in Binary and Multiple Stars, by Peter Eggleton, pp. . ISBN 0521855578. Cambridge, UK: Cambridge University Press, 2006.,

Elmegreen, B. 2000, Star Formation from the Small to the Large Scale, 445, 265

Elmegreen, B. G., & Krakowski, A. 2001, ApJ, 562, 433

Elmegreen, B. G. 2007, ApJ, 668, 1064

Er, X.-Y., Jiang, Z.-B., & Fu, Y.-N. 2013, Research in Astronomy and Astrophysics, 13, 277

Farias, J. P., Smith, R., Fellhauer, M., et al. 2015, MNRAS, 450, 2451

Fellhauer, M., & Kroupa, P. 2005, ApJ, 630, 879

Fischer, P., Welch, D. L., Coté, P., Mateo, M., & Madore, B. F. 1991, The Magellanic Clouds, 148, 200

Fregeau, J. M., Gürkan, M. A., Joshi, K. J., & Rasio, F. A. 2003, ApJ, 593, 772

Freitag, M., & Benz, W. 2001, A&A, 375, 711

Gao, B., Goodman, J., Cohn, H., & Murphy, B. 1991, ApJ, 370, 567

Geyer, M. P., & Burkert, A. 2001, MNRAS, 323, 988

Geyer, M. P., & Burkert, A. 2001, Galaxy Disks and Disk Galaxies, 230, 311

Gieles, M., & Baumgardt, H. 2008, MNRAS, 389, L28

Gieles, M., & Portegies Zwart, S. F. 2011, MNRAS, 410, L6

Goodman, J., & Hut, P. 1989, Nature, 339, 40

Goodwin, S. P. 1997, MNRAS, 284, 785

Goodwin, S. P., & Whitworth, A. P. 2004, A&A, 413, 929

Gouliermis, D., Keller, S. C., Kontizas, M., Kontizas, E., & Bellas-Velidis, I. 2004, A&A, 416, 137

Grondin, L., Demers, S., & Kunkel, W. E. 1992, AJ, 103, 1234

Gürkan, M. A., Freitag, M., & Rasio, F. A. 2004, ApJ, 604, 632

Gutermuth, R. A., Megeath, S. T., Pipher, J. L., et al. 2005, ApJ, 632, 397

Hambly, N. C., & Jameson, R. F. 1991, MNRAS, 249, 137

Hénon, M. 1965, Annales d'Astrophysique, 28, 62

Hillenbrand, L. A. 1997, AJ, 113, 1733

Hillenbrand, L. A., & Hartmann, L. W. 1998, ApJ, 492, 540

Hills, J. G. 1980, ApJ, 235, 986

Heggie, D. C., & Aarseth, S. J. 1992, MNRAS, 257, 513

Hurley, J. R., Pols, O. R., & Tout, C. A. 2000, MNRAS, 315, 543

Inagaki, S., & Saslaw, W. C. 1985, ApJ, 292, 339

Jeans, J. H. 1902, Philosophical Transactions of the Royal Society of London Series A, 199, 1

Kalirai, J. S., Fahlman, G. G., Richer, H. B., & Ventura, P. 2003, AJ, 126, 1402

Kharchenko, N. V., Piskunov, A. E., Röser, S., Schilbach, E., & Scholz, R.-D. 2005, A&A, 438, 1163

Kharchenko, N. V., Piskunov, A. E., Röser, S., Schilbach, E., & Scholz, R.-D. 2005, A&A, 440, 403

King, I. 1962, AJ, 67, 471

Kirk, H., & Myers, P. C. 2011, ApJ, 727, 64

Kirk, H., Offner, S. S. R., & Redmond, K. J. 2014, MNRAS, 439, 1765

Klessen, R. S., & Burkert, A. 2000, ApJS, 128, 287

Klessen, R. 2001, From Darkness to Light: Origin and Evolution of Young Stellar Clusters, 243, 139

Klessen, R. S., & Burkert, A. 2001, ApJ, 549, 386

Kroupa, P., Petr, M. G., & McCaughrean, M. J. 1999, Nature, 4, 495

Kroupa, P. 2001, Dynamics of Star Clusters and the Milky Way, 228, 187

Kroupa, P. 2002, Science, 295, 82

Lada, C. J., Margulis, M., & Dearborn, D. 1984, ApJ, 285, 141

Lada, C. J., Alves, J., & Lada, E. A. 1996, AJ, 111, 1964

Lada, E. A. 1999, NATO Advanced Science Institutes (ASI) Series C, 540, 441

Lada, C. J., & Lada, E. A. 2003, ARA&A, 41, 57

Larson, R. B. 1982, MNRAS, 200, 159

Larson, R. B. 1995, MNRAS, 272, 213

Leisawitz, D., Bash, F. N., & Thaddeus, P. 1989, ApJS, 70, 731

Lynden-Bell, D., & Wood, R. 1968, MNRAS, 138, 495

Lynden-Bell, D., & Eggleton, P. P. 1980, MNRAS, 191, 483

Lynga, G. 1987, Publications of the Astronomical Institute of the Czechoslovak Academy of Sciences, 69, 121

Makino, J. 1991, ApJ, 369, 200

Makino, J. 1996, ApJ, 471, 796

Mardling, R., & Aarseth, S. 1999, NATO Advanced Science Institutes (ASI) Series C, 522, 385

Maschberger, T., Clarke, C. J., Bonnell, I. A., & Kroupa, P. 2010, MNRAS, 404, 1061

Maschberger, T., & Clarke, C. J. 2011, MNRAS, 416, 541

McMillan, S., Hut, P., & Makino, J. 1990, ApJ, 362, 522

McMillan, S., Hut, P., & Makino, J. 1991, ApJ, 372, 111

McMillan, S. L. W., Vesperini, E., & Portegies Zwart, S. F. 2007, ApJL, 655, L45

Messier, C., & Niles, P. H. 1981, Clifton Park, N.Y. : Auriga, 1981.,

Mikkola, S., & Aarseth, S. J. 1993, Celestial Mechanics and Dynamical Astronomy, 57, 439

Mikkola, S., & Aarseth, S. J. 1998, Nature, 3, 309

Miller, G. E., & Scalo, J. M. 1979, ApJS, 41, 513

Moeckel, N., & Bonnell, I. A. 2009, MNRAS, 400, 657

Moraux, E., Bouvier, J., Stauffer, J. R., & Cuillandre, J.-C. 2003, A&A, 400, 891

Murray, S. D., & Lin, D. N. C. 1996, ApJ, 467, 728

Offner, S. S. R., Hansen, C. E., & Krumholz, M. R. 2009, ApJL, 704, L124

Padmanabhan, T. 2001, Theoretical Astrophysics - Volume 2, Stars and Stellar Systems, by T. Padmanabhan, pp. 594. Cambridge University Press, July 2001. ISBN-10: 0521562414. ISBN-13: 9780521562416. LCCN: QB801 .P23 2001, 594

Pandey, A. K., Upadhyay, K., Ogura, K., et al. 2005, MNRAS, 358, 1290

Parker, R. J. 2014, The Labyrinth of Star Formation, 36, 431

Parker, R. J., & Goodwin, S. P. 2015, MNRAS, 449, 3381

Parker, R. J., Goodwin, S. P., Wright, N. J., Meyer, M. R., & Quanz, S. P. 2016, MNRAS, 459, L119

Peretto, N., André, P., & Belloche, A. 2006, A&A, 445, 979

Peretto, N., Hennebelle, P., & André, P. 2007, A&A, 464, 983

Peterson, C. J., & King, I. R. 1975, AJ, 80, 427

Phelps, R. L., & Janes, K. A. 1993, AJ, 106, 1870

Piskunov, A. E., Schilbach, E., Kharchenko, N. V., Röser, S., & Scholz, R.-D. 2008, A&A, 477, 165

Plummer, H. C. 1911, MNRAS, 71, 460

Portegies Zwart, S. F., & McMillan, S. L. W. 2002, ApJ, 576, 899

Portegies Zwart, S. F., Baumgardt, H., Hut, P., Makino, J., & McMillan, S. L. W. 2004, Nature, 428, 724

Portegies Zwart, S. F., McMillan, S. L. W., & Gieles, M. 2010, ARA&A, 48, 431

Prialnik, D. 2000, ”An Introduction to the Theory of Stellar Structure and Evolution, by D. Prialnik. ISBN 052165937X. <A href=”http://www.cambridge.org/us/catalogue/catalogue.asp?isbn=052165937X. Cambridge”>http://www.cambridge.org/us/catalogue/catalogue.asp?isbn=052165937X. Cambridge</A>, UK: Cambridge University Press, 2000.”,

Price, D. J., & Bate, M. R. 2009, MNRAS, 398, 33

Prisinzano, L., Micela, G., Sciortino, S., & Favata, F. 2003, A&A, 404, 927

Proszkow, E.-M., & Adams, F. C. 2009, ApJS, 185, 486

Quinlan, G. D. 1996, ApJS, 1, 255

Raboud, D., & Mermilliod, J.-C. 1998, A&A, 333, 897

Rana, N. C., & Basu, S. 1992, A&A, 265, 499

Richtler, T. 1994, A&A, 287, 517

Sabbi, E., Sirianni, M., Nota, A., et al. 2008, AJ, 135, 173

Sagar, R., Miakutin, V. I., Piskunov, A. E., & Dluzhnevskaia, O. B. 1988, MNRAS, 234, 831

Sagar, R., & Richtler, T. 1991, A&A, 250, 324

Sagar, R. 2002, Extragalactic Star Clusters, 207, 515

Salpeter, E. E. 1955, ApJ, 121, 161

Sanner, J., Geffert, M., Brunzendorf, J., & Schmoll, J. 1999, VizieR Online Data Catalog, 334,

Sanner, J., & Geffert, M. 2001, A&A, 370, 87

Schmeja, S., & Klessen, R. S. 2006, A&A, 449, 151

Schmeja, S., Kumar, M. S. N., & Ferreira, B. 2008, MNRAS, 389, 1209

Smith, R., Fellhauer, M., Goodwin, S., & Assmann, P. 2011, MNRAS, 414, 3036

Spitzer, L., Jr. 1958, ApJ, 127, 17

Spitzer, L., Jr. 1969, ApJL, 158, L139

Spitzer, L. 1987, Princeton, NJ, Princeton University Press, 1987, 191 p.,

Smith, L. J., & Gallagher, J. S. 2001, MNRAS, 326, 1027

Stolte, A., Brandner, W., Brandl, B., & Zinnecker, H. 2006, AJ, 132, 253

Testi, L., Sargent, A. I., Olmi, L., & Onello, J. S. 2000, ApJL, 540, L53

Tutukov, A. V. 1978, A&A, 70, 57

Vanbeveren, D. 1982, A&A, 113, 205

Weidner, C., & Kroupa, P. 2004, MNRAS, 348, 187

Will, J.-M., Bomans, D. J., & de Boer, K. S. 1995, A&A, 295, 54

Williams, J. 2000, IAU Joint Discussion, 3,

Yu, J., de Grijs, R., & Chen, L. 2011, ApJ, 732, 16

Zinnecker, H. 1982, Annals of the New York Academy of Sciences, 395, 226